POLITECNICO DI MILANO

SCUOLA DI INGEGNERIA INDUSTRIALE E DELL'INFORMAZIONE

CORSO DI LAUREA MAGISTRALE IN INGEGNERIA BIOMEDICA

CORRELATION OF FUNCTIONAL AND STRUCTURAL BRAIN CONNECTIVITY WITHIN RESTING STATE NETWORKS COMBINING MEASURES FROM INDEPENDENT COMPONENT ANALYSIS AND PROBABILISTIC TRACTOGRAPHY

Relatori: Tesi di Laurea di:

Prof. Giuseppe Baselli   **Laura Pelizzari**

Dott.ssa Francesca Baglio   **Matr.: 799528**

Correlatore:

Ing. Elisa Scaccianoce

Anno Accademico 2013/2014

A mio nonno Angelo

Ringraziamenti

Contents

List of Abbreviations

ACR	Anterior Corona Radiata
AD	Alzheimer Disease
ADC	Apparent Diffusion Coefficient
ASL	Amyotrophic Lateral Sclerosis
ATR	Anterior Thalamic Radiation
bedpostX	Bayesian Estimation of Diffusion Parameters Obtained using Sampling Techniques
BOLD	Blood Oxygenation Level Dependent
BSS	Blind Source Separation
CC	Corpus Callosum
CF	Connettività Funzionale
CS	Connettività Strutturale
DMN	Default Mode Network
DTI	Diffusion Tensor Imaging
DWI	Diffusion Weighted Imaging
EEG	Electroencepalography
EPI	Echo Planar Imaging
FA	Fractional Anisotropy
FC	Functional Connectivity
FIX	FMRIB's ICA-based Xnoiseifier
FLIRT	FMRIB's Linear Image Registration Tool
fMRI	functional Magnetic Resonance Imaging
FNIRT	FMRIB's non-Linear Image Registration Tool
FSL	FMRIB Software Library
FWHM	full width at half maximum
GLM	General Linear Model
GM	Gray Matter
HARDI	High Angular Resolution Diffusion Imaging
HBP	Human Brain Project

HCP	Human Connectome Project
HRF	Hemodynamic Response Function
IC	Independent Component
ICA	Independent Component Analysis
IFOF	Inferior Frontal-Occipital Fasciculus
ILF	Inferior Longitudinal Fasciculus
IQR	Inter-Quartile Range
LLN	Left Later Network
MCI	Mild Cognitive Impairment
MCMC	Markov Chain Montecarlo
MD	Mean Diffusivity
MEG	Magnetoencephalography
MELODIC	Multivariate Exploratory Linear Optimized Decomposition into Independent Component
MNI	Montreal Neurological Institute
MPRAGE	Magnetization Prepared Rapid Acquisition Gradient Echo
MR	Magnetic Resonance
MRI	Magnetic Resonance Imaging
MS	Multiple Sclerosis
PCA	Principal Component Analysis
PD	Parkinson Disease
pdf	probability density function
pICA	probabilistic Independent Component Analysis
PPCA	Probabilistic Principal Component Analysis
RF	Radiofrequency
RLN	Right Lateral Network
RM	Risonanza Magnetica
ROI	Region Of Interest
rsfMRI	resting state functional Magnetic Resonance Imaging
RSN	Resting State Network
SC	Structural Connectivity
SLF	Superior Longitudinal Fasciculus

SMN   Sensory-Motor Network

TE   Echo Time

TI   Inversion Time

WM   White Matter

List of Figures

List of Tables

Sommario

Contesto e obiettivi dello studio: la risonanza magnetica funzionale a riposo (in condizione di "resting state") e la trattografia, che si basa su neuroimmagini pesate in diffusione, sono tecniche consolidate di risonanza magnetica (RM) per indagare rispettivamente la connettività funzionale (CF) e la connettività strutturale (CS) del cervello (van de Heuvel et al,. 2009). Lo studio combinato di CF e CS sta acquisendo crescente interesse all'interno della comunità scientifica, sia nel campo della ricerca di base sia nella pratica clinica, in quanto consente di integrare le informazioni relative alla materia grigia e alla materia bianca. Infatti, è stato dimostrato che il cervello si organizza in reti, il cui corretto funzionamento dipende da una perfetta sinergia tra le aree corticali e i fasci di materia bianca (Cabral et al., 2014). Di conseguenza, lo studio combinato di queste strutture può consentire di capire meglio il funzionamento del cervello, non solo in condizioni normali ma anche in presenza di patologie neurologiche o psichiatriche. Lo scopo di questo lavoro era studiare, in un gruppo di soggetti sani, la correlazione tra CF e CS all'interno della Default Mode Network (DMN), della Left Lateral Network (LLN) e della Right Lateral Network (RLN).

Panoramica sul metodo: questo studio si basa su due consolidati approcci relativi all'analisi separata di CF e CS, che, per nostra conoscenza, non sono stati integrati in questo modo in precedenza. Le *resting state networks* (RSNs) sono state estratte a livello di gruppo mediante l'analisi delle componenti indipendenti, metodo comunemente usato per effettuare tale procedura. Utilizzando un approccio innovativo, alcune di esse sono state divise in *cluster*, i quali costituiscono i nodi delle reti considerate. L'entità della correlazione tra CF e CS per le diverse coppie di nodi, è stata valutata sia a livello del singolo soggetto che a livello di gruppo.

In merito alla CF, i segnali di ciascun soggetto sono stati estratti dai dati di RM funzionale a riposo con il metodo della *dual regression*, sulla base dei cluster ottenuti a livello di gruppo. L'entità del legame di CF è stata quindi calcolata mediante il coefficiente di correlazione di Pearson.

I dati di CS sono stati ricavati dalle immagini pesate in diffusione che forniscono informazioni sulla/e direzione/i locale/i delle fibre di sostanza bianca. Le connessioni strutturali sono state ottenute utilizzando i cluster come regioni di interesse per la trattografia probabilistica. In generale, la trattografia guidata da risonanza magnetica funzionale ricostruisce fibre virtuali che collegano aree di materia grigia, le quali in molti casi sono definite a partire dall'attivazione a seguito dell'esecuzione di un compito o di un evento, mentre nel nostro caso sono state individuate a partire dalle RSNs. L'approccio probabilistico permette di superare i limiti dell'approccio deterministico, che si ferma in corrispondenza di regioni che presentano una struttura delle fibre più complessa rispetto al tradizionale modello unidirezionale.

Metodo: Questo studio è stato condotto presso il laboratorio di risonanza magnetica della Fondazione Don Carlo Gnocchi Onlus, IRCCS Santa Maria Nascente di Milano, utilizzando uno scanner da 1.5 Tesla (Siemens Magnetom Avanto, Erlangen, Germania). Le immagini di risonanza magnetica funzionale in *resting state* e le immagini pesate in diffusione sono state acquisite su venti soggetti sani e destrimani (età media = 45,70 ± 11,53 anni, 9 maschi). Un soggetto è stato tuttavia escluso dalle successive analisi a causa della scarsa qualità delle rispettive immagini pesate in diffusione. Dopo avere effettuato una prima elaborazione dei dati grezzi, sono state estratte le mappe spaziali delle RSN. Esse sono state ottenute mediante un'analisi delle componenti indipendenti effettuata sui dati del gruppo, secondo il metodo proposto da Dipasquale et al. (2015) e impostando a 30 l'ordine del modello. La DMN, la RLN e la LLN sono state individuate e, successivamente, divise in sotto-reti, le quali sono state definite sulla base della loro separazione anatomica. All'interno di ogni RSN considerata, la CF è stata valutata per ciascun soggetto, calcolando tra tutte le possibili coppie di sotto-reti il coefficiente di correlazione di Pearson, trasformato poi in un indice di intensità z. I valori ottenuti sono stati organizzati in matrici di CF. Mediando i valori dei singoli soggetti, è stata costruita una matrice di CF di gruppo. Le coppie di sotto-reti utilizzate nelle analisi di CF sono state successivamente considerate anche come regioni *seed* e *target* per effettuare le analisi di trattografia probabilistica su ciascun soggetto. In particolare, per ogni coppia di sotto-reti, sono stati ottenuti due tratti diversi, a seconda di quale delle due regioni corticali fosse definita come seed o come target. In seguito, questi due tratti sono stati normalizzati e moltiplicati al fine di ottenere

un unico tratto "simmetrico" che connettesse strutturalmente le due regioni di interesse. Per ogni tratto "simmetrico" ricostruito è stato adottato come indice di CS il numero di voxel sopra soglia (0.02) (Khalsa et al., 2014). I valori ottenuti sono stati quindi schematizzati in matrici di CS. Una media dei valori relativi ai singoli soggetti ha consentito di costruire una matrice di CS di gruppo per ogni RSN considerata. Al fine di valutare la consistenza statistica dei tratti individuati, sono state create delle mappe probabilistiche di gruppo per ciascun fascio. Esse sono state ottenute mediando le immagini binarizzate dei tratti relativi ai singoli soggetti e sogliando quindi, con tre diversi valori (20%, 40%, 60%). Per ogni coppia di sotto-reti, è stata calcolata l'intensità media sul tratto appartenente alle mappe probabilistiche. Tale intensità è stata adottata come indice di robustezza statistica e i valori ottenuti sono stati raccolti in matrici. Infine, per valutare il rapporto esistente tra reti strutturali e reti funzionali, gli indici di CF e di CS sono stati correlati tra di loro, sia a livello del singolo soggetto che a livello del gruppo, mediante il coefficiente di correlazione di Pearson.
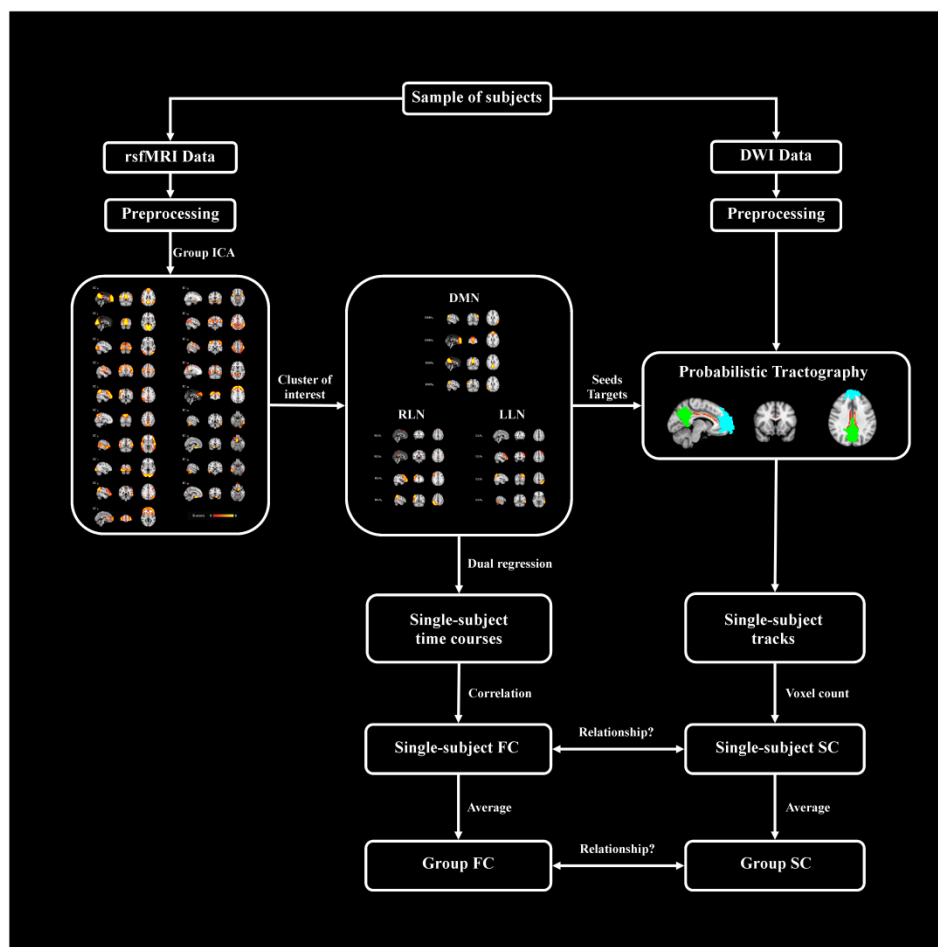
Figura 1 Schema riassuntivo del metodo

Risultati: All'interno di ciascuna RSN considerata, sono stati osservati elevati valori di CF e tutte le coppie di sotto-reti sono risultate essere strutturalmente collegate da un tratto o un insieme di tratti. Inoltre, la maggior parte dei fasci individuati (4 su 18) si sono rivelati statisticamente robusti. Combinando i valori di CF e CS ottenuti, a livello del singolo soggetto, abbiamo osservato che 11 soggetti presentavano una correlazione statisticamente significativa tra CF e CS, soprattutto all'interno della LLN e della RLN. Questo risultato è stato confermato dall'analisi a livello di gruppo, la quale ha evidenziato una forte correlazione tra CF e CS, soprattutto nella LLN e nella RLN (Fig. 2, pannello b e c). All'interno della DMN, invece, sono stati ottenuti alti valori di CF e di CS separatamente ma non è stata osservata alcuna correlazione tra di esse (Fig. 2, pannello a).
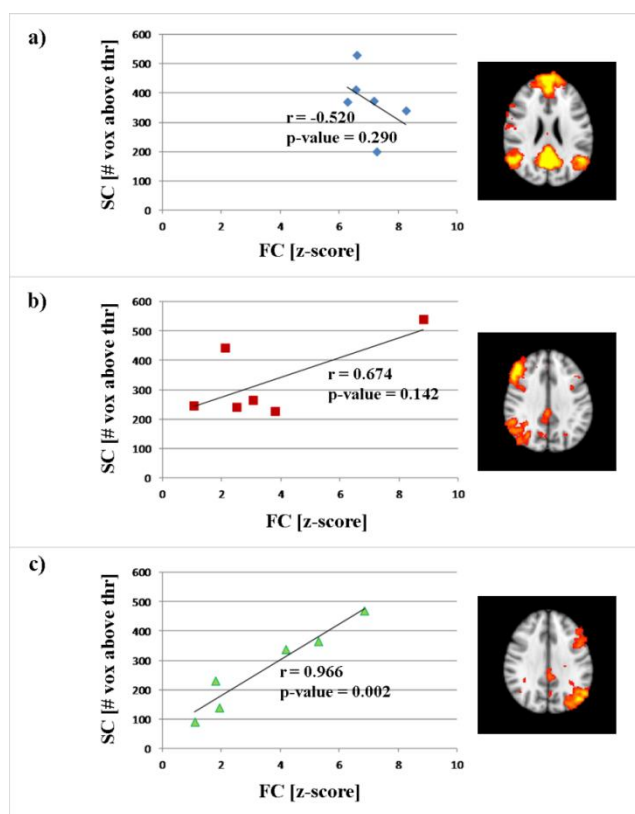
Figura 2 Relazione tra connettività funzionale e strutturale di gruppo all'interno della DMN (pannello a, in blu), della RLN (pannello b, in rosso) e della LLN (pannello c, in verde).

Discussione e Conclusione:

Questi risultati suggeriscono che la LLN e la RLN sono reti altamente funzione-specifiche e, dunque, i collegamenti strutturali diretti tra le loro sotto-reti riflettono pienamente la comunicazione funzionale esistente tra di esse. All'interno della DMN, invece, l'assenza di

correlazione tra CF e CS può essere giustificata dalla presenza di percorsi aggiuntivi e fibre collaterali che collegano le sue sotto-reti. Questo risultato è coerente con la natura associativa e integrativa di questa rete. In conclusione, in questo studio abbiamo proposto un approccio per correlare CF e CS, utile per indagare il problema della connettività cerebrale nel suo complesso. I nostri risultati suggeriscono che un'alta CS riflette un forte livello di comunicazione all'interno della rete ma che un'alta CF tra diverse regioni corticali non implica necessariamente un legame strutturale diretto tra di esse.

Summary

Background and purpose: resting state functional MRI (rsfMRI) and tractography, derived from diffusion weighted imaging (DWI), are well-established modalities to investigate respectively functional connectivity (FC) and structural connectivity (SC) (van de Heuvel et al., 2009). The combined study of brain FC and SC is gaining increasing interest both in neuroscience and clinical practice since it discloses integrated information about gray matter (GM) and white matter (WM). Indeed, the existence of brain networks, whose correct activity depends on a perfect synergy between cortical areas and WM bundles, was proved (Cabral et al., 2014). Hence studying these networks as a whole may lead to better understand brain functionality not only in normal condition but also in pathological ones. The aim of this work was exploring the correlation between FC and SC in the default mode network (DMN), left lateral network (LLN) and right lateral network (RLN) within a healthy subject sample.

Method overview: this study is based on two well-established approaches to FC and SC separated analysis, which are integrated in this way for the first time to our knowledge. Resting state networks (RSNs) were extracted at group level trough the classic blind-source separation method of spatial independent component analysis (ICA). By a novel approach, some of them were split into localized clusters, which represent the nodes of the addressed network. The strength of FC and SC correlation for the pairs of nodes was analyzed both, at single and group level.

As to FC, single-subject rsfMRI signals were extracted through the dual regression method, based on the group clusters. FC link strength was hence individually derived by Pearson's correlation coefficient.

SC data were extracted from diffusion weighted imaging (DWI) which provides information about the local direction (or directions) of white matter (WM) fibers. Structural links were obtained using the clusters as seed/target ROIs for rsfMRI-guided probabilistic tractography. fMRI-guided tractography, in general, reconstructs virtual connections between gray matter (GM) ROIs, which in many cases are defined by the fMRI activation while in our case were set as the resting state network clusters. The probabilistic approach permits to overcome the limitations of the deterministic one, which

is stopped by regions that present a more complex fiber structure than a unidirectional mainstream.

Methods: the study was conducted in the MR Lab, IRCCS S. M. Nascente, Fondazione Don Carlo Gnocchi Onlus, Milano, using a 1.5 Tesla Siemens Magnetom Avanto (Erlangen,Germany) MRI scanner. Resting state fMRI and DWI data were acquired from twenty healthy right-handed voluntary subjects (mean age = 45.70 ± 11.53 years, 9 males) but one subject was excluded due to its DWI data low quality. After data processing performed according to Dipasquale et al. (2015), the RSN extraction was performed with group-ICA (model order = 30). DMN, RLN and LLN were selected and then divided into sub-networks defined as anatomically separated clusters. Within each RSN, single subject FC values were calculated with Pearson correlation coefficient (transformed in z-value) between all possible cluster pairs and stored in FC matrices. By averaging these values across subjects, a group FC matrix was obtained for each RSN. The pairs of clusters selected for the FC analysis were also used as seed and target regions in single subject probabilistic tractography. In details, for each pair of sub-networks two tracts were obtained by setting one cluster as seed and the other as target region and *viceversa.* Afterwards, these two tracts were normalized and then multiplied in order to obtain a "symmetric" single tract connecting the two regions of interest (ROIs). For each reconstructed "symmetric" tract the number of voxels above-threshold (0.02) was adopted as SC index (Khalsa et al., 2014) and stored in SC matrices. Averaging these values across subjects, a group SC matrix was obtained for each RSN. In order to evaluate tract consistency, group probabilistic maps were created for each bundle by averaging binarized tract images across subjects and thresholding them at three different values: 20%, 40%, 60%. For each pairs of ROIs, the mean intensity calculated on tract probabilistic maps was adopted as robustness index and stored in SC consistency matrices. Finally, in order to probe functional and structural networks relationship, FC and SC indexes were correlated by Pearson coefficient both at single and group level.
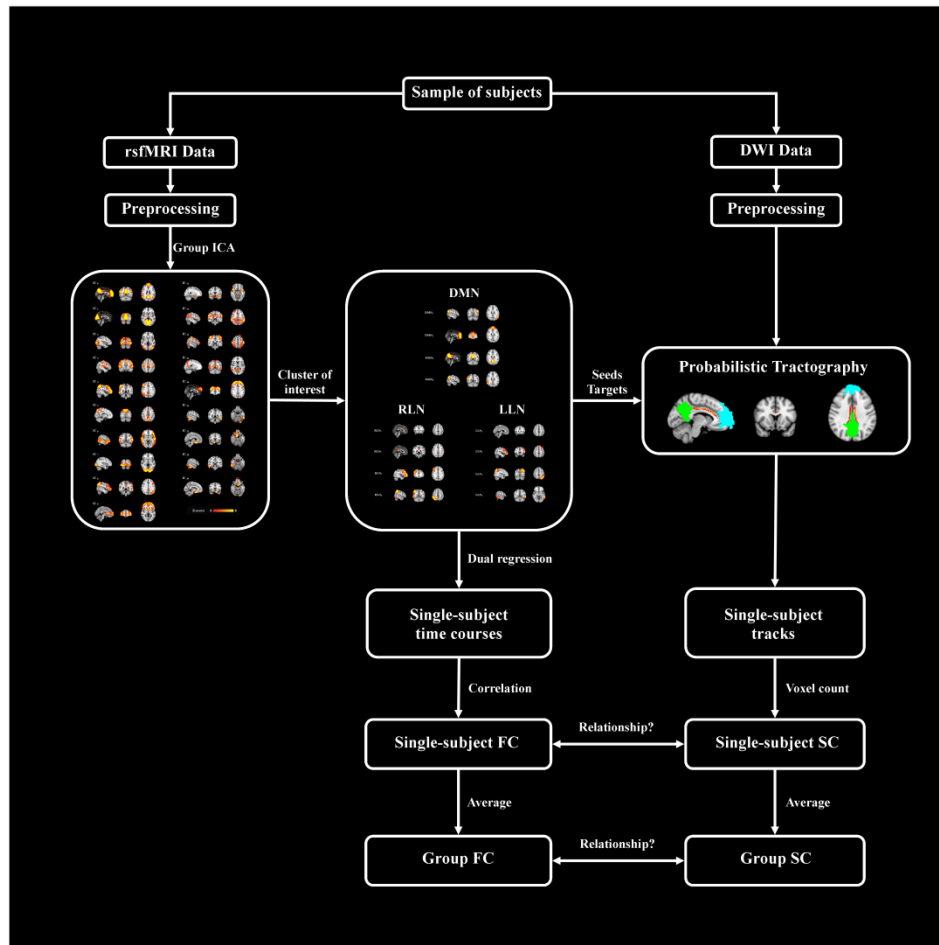
Figure 3 Method pipeline.

Results: within each considered RSN, high values of FC were observed and all the pairs of sub-networks were found to be structurally connected by a tract or an ensemble of tracts. The majority of the identified bundles (4 of 18) were statistically robust across subjects. Combining FC and SC results, at single level we observed that 11 subjects presented a statistically significant FC-SC correlation especially in LLN and in RLN. This was corroborate by the group level analysis that showed a high FC-SC correlation mainly in the LLN and RLN (Fig 4, panel b and c). The DMN, instead, revealed high values of FC and SC separately but no correlation was found between them (Fig 4, panel a).
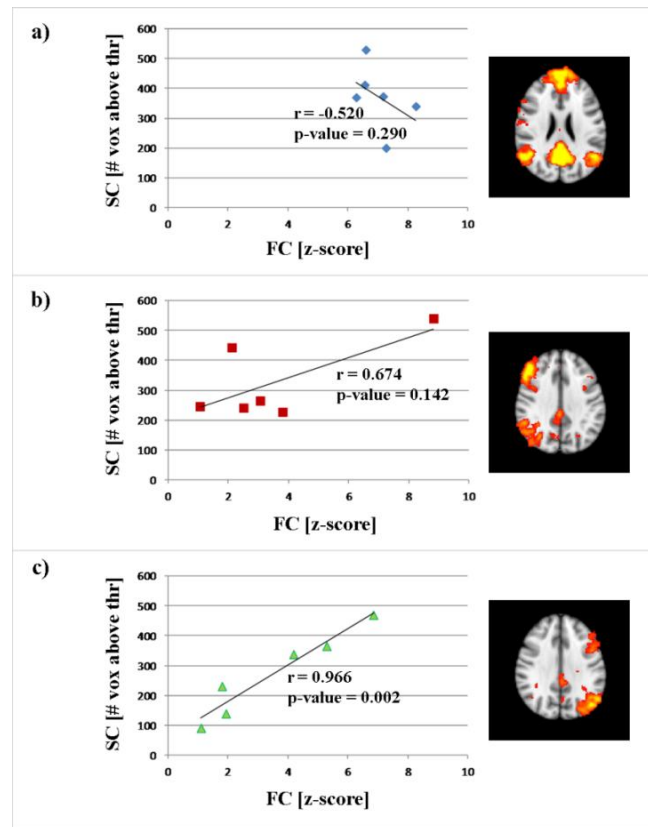
Figure 4 Relationship between structural and functional group connectivity within DMN (panel a, in blue), RLN (panel b, in red) and LLN (panel c, in green).

Discussion and Conclusion: our results suggest that LLN and RLN are highly function-specific networks since direct structural links between their clusters reflect the functional communication existing between them. Within DMN, instead, the absence of correlation between FC and SC can be explained by additional and collateral fiber pathways which link DMN sub-networks. This result is consistent with the associative and integrative nature of DMN.

In conclusion, in this study we proposed a useful approach to correlate FC and SC to deeply investigate the brain connectivity issue in its entirety. Our results suggest that a high SC reflects a strong communication level within RSNs but a high FC between different cortical regions does not imply a direct structural link.

Chapter 1

Introduction

The brain is the most complex human organ and probably one of the most complicated systems in nature. It is a highly efficient integrative system, as it combines multiple information from different body districts and external environment. This information is very rapidly carried through the white matter (WM) from one region of gray matter (GM) to another. In the last decades, the evidences of the existence of neuronal networks and the increase of knowledge about brain area specialization, have led the scientific community to consider the issue of brain connectivity as a topic of great relevance. In 1993 Zeki had already highlighted the striking capability of the visual system to integrate features processed in particular brain areas, referring to it as 'the binding problem'. The integrative nature he observed in this particular system has now become a paradigm for the whole brain.

In this fashion, the brain connectivity studies aim at deeply exploring the intricate communication among regions which are strongly interconnected (Sporns et al., 2004; van den Heuvel et al., 2010). According to the kind of connection, the brain connectivity may be anatomical/structural (i.e., anatomical links, such as synapses or fibre pathways) or

functional (i.e., the functional dependencies between cortical regions) (Cabral et al., 2014). Furthermore, we can refer to brain connectivity at different levels: between single neurons (Hellwig et al., 2000; Thomas et al., 1984; Dickson et al.; 1974; Michalski et al., 1983), between neuronal population (K Sameshima et al., 1999; Boahen et al., 2000; Hofer et al., 2011) or between anatomically segregated regions (Rubinov et al., 2010; Sporns et al., 2002; Van Den Heuvel et al., 2009; Van Den Heuvel et al., 2010; Deco et al., 2013; Greicius et al., 2009; Greicius et al., 2013).

In this framework, methods for studying both functional connectivity (FC) and structural connectivity (SC) have experienced huge, almost parallel, developments in the last few years. Nevertheless, in order to address the connectivity issue comprehensively, the fusion of these two approaches in a multimodal methodology appears necessary by now. Several technical limitations are stumbling blocks to these combined approach, such as the limited knowledge of WM to GM interface. The empirical investigation of the correlation between FC and SC, indeed, implies the *a priori* assumption of GM and WM contiguity. Therefore, although progresses have been made in the evaluation of FC and SC separately (Dipasquale et al., 2015; Laganà et al., 2012; Caffini et al., 2014), the relationship between functional and structural physiological synergies is not well understood yet. In this context, magnetic resonance imaging (MRI) studies are particularly prone to the *in-vivo* investigation of both the functional and structural aspects of brain connectivity. In particular, this work took advantage of different MRI techniques in order to address both FC and SC problem by means of inherently statistical methods (i.e., resting state functional MRI and probabilistic tractography respectively), which will be touched on hereunder and discussed at length in the following chapters.

Regarding FC, there are two different brain MRI techniques which highlight the activations of cortical regions. The first one, the functional MRI (fMRI), yields to the identification of cortical region elicited by a specific task (e.g., verbal fluency, attention, hand motion, finger tapping, *etc.*) (Phelps et al., 1997; Bush et al.,1999; Tanaka et al., 2002; Desmond et al., 1997). The second one, the resting state fMRI (rsfMRI), allows, instead, to explore the correlation between spatially distant cortical regions in rest conditions. Such technique revealed functional networks that slowly activate and deactivate spontaneously, pointing out the existence of underlying network dynamics defined by specific spatial, temporal and spectral characteristics (Cabral et al., 2014).

These networks are defined as resting-state networks (RSNs) and consist of anatomically separated, but functionally linked brain regions that show a high level of ongoing functional connectivity during rest (van den Heuvel et al., 2010).

RSNs were observed for the first time by Biswal and colleagues (1995) while they were performing fMRI studies with a finger tapping task. They discovered that sensory-motor area exhibited correlated activations during the motor task, but also during the rest phase. Hence, as Seneca said in 65 BC., "the fact that the body is lying down is no reason for supposing that the mind is at peace. Rest is far from restful". Indeed, at rest, brain shows slow spatio-temporally organized fluctuations of neuronal activity. Probably these fluctuations play an important role in keeping the system active, improving its performances and increasing the reaction time if an unexpected stimulus is provided (Xiong et al, 2008). Biswal's surprising results were re-examined and, interestingly, it was discovered that the majority of the RSNs actually represent known functional networks (Biswal et al., 1995; Cordes et al., 2000; De Luca et al., 2006, Damoiseaux et al., 2006; Fox et al., 2005). Furthermore it was found that the RSNs overlap those regions that are known to share a common function (e.g., primary motor regions, primary visual regions, parietal and frontal lobes involved in attention processing) (van den Heuvel et al., 2010). For this reason they were appointed as 'task positive RSNs'. Examples of task positive RSNs are the sensory-motor network (SMN) , the primary visual network (PVN), the two lateralized networks consisting of superior parietal and superior frontal regions (LLN and RLN) (van den Heuvel et al., 2010) and the salience network (Di et al., 2014). Among the identified RSNs, the default mode network (DMN), consisting of posterior cingulated cortex, medial frontal and inferior parietal regions, is considered of particular interest. In fact, differently from the others, DMN clusters are more functionally connected at rest than while performing a task (Greicius et al. 2003), leading to define it as 'task-negative RSN'.

Once established that fMRI and rsfMRI truly reflect the ongoing communication between cortical regions, we need to consider also the structural connections which support the functional activity. This role is played by WM fibers which are commonly studied by means of tractography, derived from diffusion weighted imaging (DWI). Specifically, it allows to virtually reconstruct WM fiber bundles, making feasible *in-vivo* and *non-invasive* structural connectivity study (Basser et al, 2000; Melhem et al., 2002; Catani et al., 2008). First tractographic investigations were conducted in the late '90s (Makris et al., 1997),

taking advantage of the water diffusion laws (i.e., Brownian motion) applied to brain micro-structures. The water diffusion, indeed, is hindered by anisotropic structures such as WM bundles which constrain the water molecules to move along them. In this fashion, following the water molecules represents an indirect way to follow the fibers and then to virtually reconstruct the WM bundles. This technique stood for a real revolution in brain studies since WM had never been identified by any direct *in-vivo* inspection but exclusively by post-mortem brain dissections. In the last years, different fiber tracking algorithms were developed. According to the way they connect the voxel-to-voxel information, we can refer to deterministic or probabilistic approaches (Jones, 2008). Specifically, deterministic approach is more intuitive than the probabilistic one. Indeed, given a seed point, deterministic algorithms reconstruct the fibers that pass through it, following the principal direction/s defined in each voxel. On the other hand, probabilistic tractography generates a large number of pathways defining a probability map in a confidence range in which the fibers can run starting from the chosen seed (Behrens et al., 2003). However, independently from the algorithm, tractography allows nowadays a worthwhile estimation of the brain structural connectivity pattern.

Back to the issue of brain connectivity, it appears evident, now, the strong correlation between functional and structural data and the reason for the numerous attempts to integrate them. Combined FC and SC studies, indeed, have revealed that functional RSN structure often reflects underlying structural linked networks (Honey et al., 2007; Hagmann et al., 2008; Damoiseaux et al., 2009; Greicius et al., 2009; Honey et al., 2009; van den Heuvel et al., 2009; van den Heuvel et al., 2010). However, beware the straightforwardness of this relationship!!! SC is considered a good predictor of FC (Honey et al., 2009), but a higher FC does not necessarily imply a higher SC, as shown by studies that reported the absence of direct anatomical connection between areas that reveal high functional correlation (Koch et al., 2002). Furthermore, recent studies (Krienen and Buckner, 2009; O'Reilly et al., 2010; Buckner et al., 2011; Lu et al., 2011) suggest that the connectivity within or between RSNs may also be addressed by polysynaptic anatomical cerebro-cerebellar circuits pathways, namely there would be more than one pathway to link two distant region of the cortex.

All the considerations above have been the premises of innovative and ambitious projects such as the Human Connectome Project (HCP) (Elam et al., 2014; Van Essen et al., 2012;

Smith et al., 2013; Setsompop et al, 2013) and Human Brain Project (HBP) (Huerta et al., 1993; Koslow et al., 1997; Shepherd et al., 1998), whose challenging aim consists in the mapping of the whole brain functionality within the next ten years. In particular, the HCP appears extremely interesting and revolutionary since it has made high quality data available for the entire scientific community in order to promote brain connectivity studies with a multimodal approach (i.e., with images acquired with different techniques, such as rsfMRI, fMRI, DWI, *etc*.). The integration of complementary information, indeed, would allow to fill gaps that each modality alone leaves due to its intrinsic technical limitations. For this reason, the multimodal approach has been extended also to *non-MRI* techniques such as the EEG and MEG , whose data were combined with rsfMRI data (Brookes et al., 2011; de Munck et al., 2007; de Pasquale et al., 2010; Difrancesco et al., 2008; Feige et al., 2005; Goncalves et al., 2006; Hipp et al., 2012; Laufs et al., 2003; Liu et al., 2010; Moosmann et al., 2003; Nikouline et al.,2001) in order to investigate the brain from different points of view and at different organization levels.

Finally, the relevance of combined functional and structural connectivity studies is underlined by clinical investigation. Particularly in neurological disorders and psychiatric diseases, such as Alzheimer Disease (AD), Amyotrophic Lateral Sclerosis (ASL), Parkinson Disease (PD), Mild Cognitive Impairment (MCI), multiple sclerosis (MS), depression, schizophrenia, autism, it has been proved that the alteration of human functions (i.e., memory, language, attention, *etc*.) may be revealed both by functional and structural methodologies, since often there is the simultaneous involvement of WM structures and GM regions (Binnewijzend et al., 2012; Damoiseaux et al., 2012; Greicius et al., 2004; Zhou et al., 2010; Mohammadi, B. et al, 2009, Tedeschi,et al, 2012; Luo et al, 2014; Kwak et al, 2010; Rombouts et al., 2005; Bonavita et al., 2011; Faivre et al., 2012; Schoonheim et al., 2013; Greicius et al.,2007; Liu et al., 2008; Whitfield-Gabrieli et al., 2009; Bluhm etal., 2007; Garrity et al., 2007; Cornew et al., 2012; Cherkassky et al., 2006; Kennedy et al., 2006; Lai et al., 2010; Weng et al., 2010). Therefore, understanding the intrinsic and complex mechanisms leading to these alterations might yield to the definition of potential clinical biomarkers and innovative pharmacologic or rehabilitative treatments.

This work was developed considering the wide background illustrated above. The aim of our study was to analyze FC and SC within three resting state network of interest: DMN, LLN and RLN. We focused on these three networks due to their particular neurological

interest. As previously mentioned, DMN is highly involved in brain activity at rest. Moreover, it is the most consistently observable network, in any age and also during the sleep. On the other hand, LLN and RLN, overlap to brain areas that underlie multiple cognitive paradigms, including memory, language and perception (Pievani et al., 2014). On a group of healthy subjects we acquired rsfMRI and DWI data in order to establish if there was correlation between FC and SC within the above-mentioned RSNs. Specifically, FC was probed by assessing the correlation between rsfMRI time series associated to their respective clusters while SC was evaluated by means of probabilistic tractography. The pipeline of the performed analysis is reported in figure 1.1. A detailed explanation of each step will be provided in the chapter 3.

In conclusion, our multimodal approach tries to answer some basic questions: is there a correspondence between functional and structural connectivity within the examined resting state networks? may this correspondence (or absence of correspondence) give information about the link of different brain structures in normality? if no correspondence is found, are we dealing with pathologies?

Answering these questions is just a little tile in brain nature deep understanding. However, as Sir James Jeans said, "sciences usually advances by a succession of small steps". The entire scientific community hopes that our brain, this wonderful Goldberg machine, will be able to understand how it is organized and how it works itself, just doing what it does best: being activated and, through a complex reaction chain, thinking.
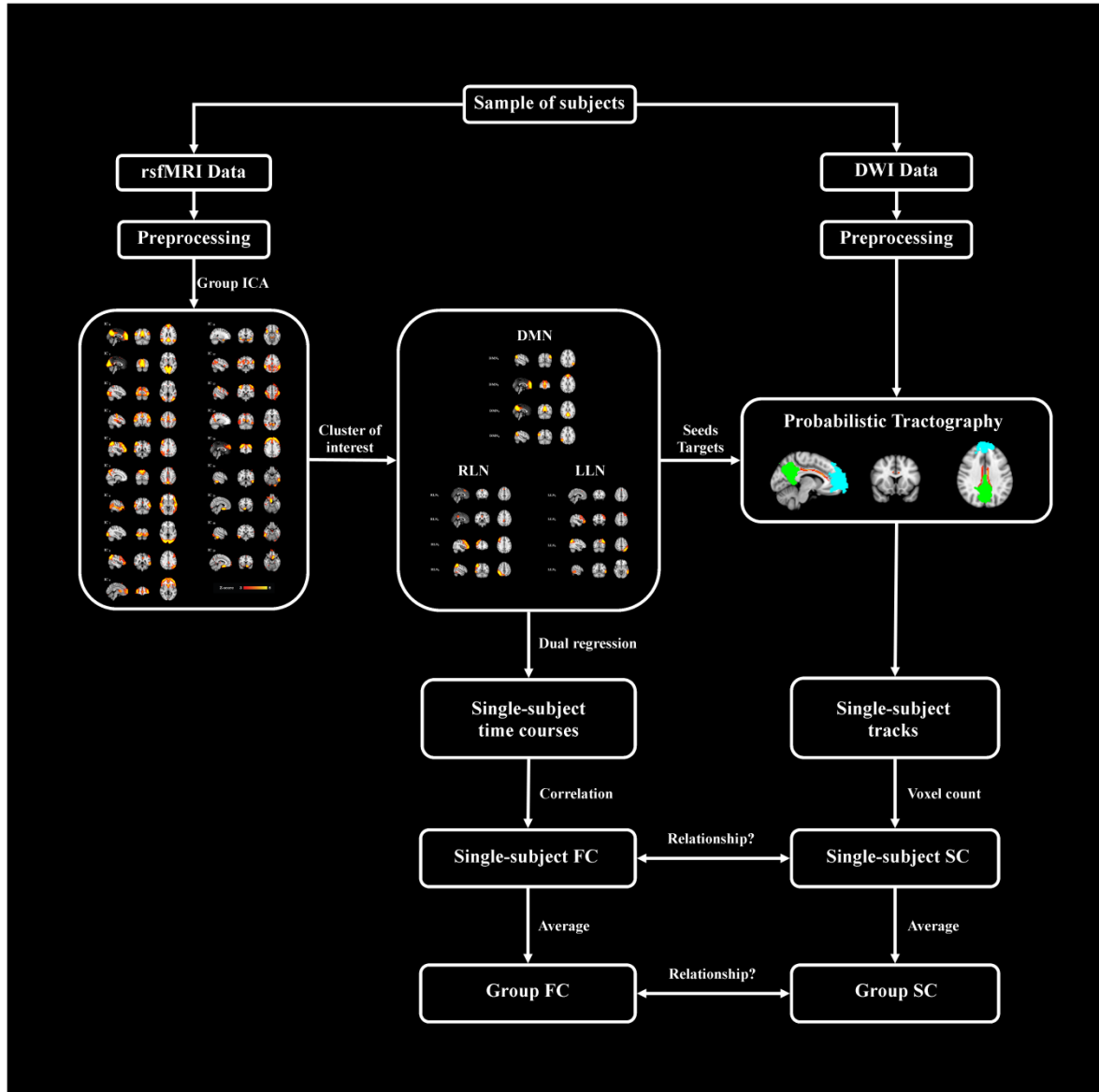
Figure 1.1 Pipeline of the performed study. Healthy subjects' rsfMRI and DWI data were preprocessed. Functional and structural connectivity analysis were performed both at a single-subject level and at group level. A comparison between functional connectivity and structural connectivity results was carried out. rsfMRI = resting state functional magnetic resonance imaging; DWI = diffusion weighted imaging; ICA = Independent Component Analysis; DMN = Default Mode Network; RLN = Right Lateral Network; LLN = Left Lateral Network; FC = Functional Connectivity; SC = Structural Connectivity.

Chapter 2

Theoretical Aspects

In this chapter we illustrate the theoretical aspects of the magnetic resonance imaging (MRI) techniques used for this study.

First of all, theoretical details about the MRI acquisition sequences used for both, functional and structural images, are provided (par. 2.1).

Then, the basic principles and processing of functional magnetic resonance imaging (fMRI) and diffusion weighted imaging (DWI) are described (pars. 2.2 and 2.3). Finally, the combination of functional information provided by fMRI and structural information supplied by DWI is discussed in 'fMRI-guided tractography' section (par. 2.4).

2.1. Image acquisition: Echo Planar Imaging (EPI)

The most common MRI sequence used for both, functional magnetic resonance imaging (fMRI) and diffusion weighted imaging (DWI) acquisitions is the echo planar imaging (EPI). It is based on a gradient echo sequence and it allows to explore the k-space, slice per slice, within a single shot (figure 2.1).
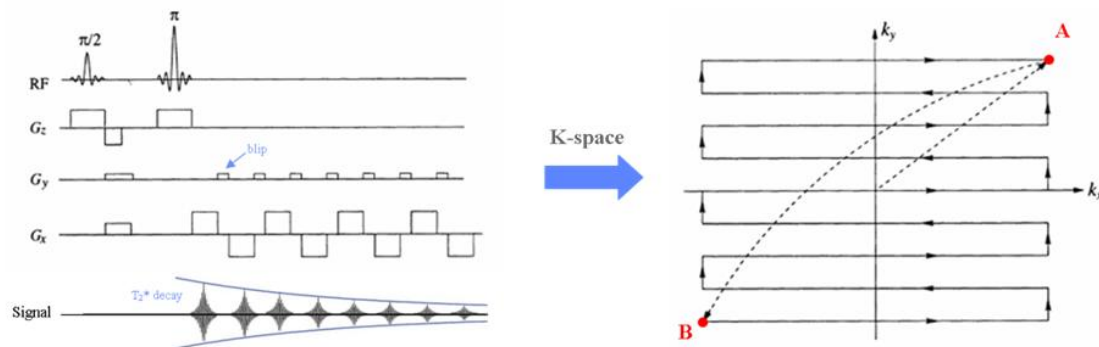
Figure 2.1 EPI sequence on the left and its trajectory drawn in the k-space on the right.
RF=radiofrequency pulse; G_x, G_y, G_z = gradient pulses respectively in x, y, z directions.

After slice selection, performed by Gz gradient, Gx and Gy gradients set the start position in k-space to point in A. Then, the radio frequency (RF) inversion pulse (angle equal to 180°) flips the starting sampling point A into B (Fig 2.1). Afterwards, by means of Gx, frequency encoding is performed and an entire k-space line is sampled during the echo phase. Finally, a phase encoding gradient pulse called blip is applied for moving to the following line.

If compared to other MRI sequences, EPI sequence is characterized by high temporal resolution, since a slice is acquired in just 100 ms. As a counterpart it has low spatial resolution (with respect to anatomical MRI images). Despite of this, the EPI sequence provides T2*-weighted contrast and its high temporal resolution allows to reduce movement artifacts. For these reasons, it is the most used sequence for fMRI and DWI.

2.2. rsfMRI: Basic Principles

In an fMRI study subjects are maintained in controlled mental states which are defined by a precise experimental design. For example, in the common block design fMRI, a baseline control state is alternated with an active state which is called 'task' (Petersen et al.,2000).

During a rsfMRI exam, instead, the subject is required to relax and lay down with closed eyes (Fig 2.2).
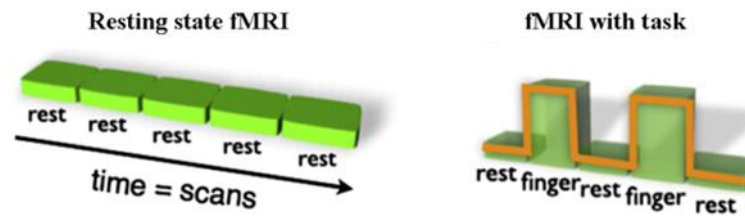
Figure 2.2 Comparison between resting state fMRI and block design fMRI experimental design (Van den Heuvel et al., 2010)

rsfMRI is particularly interesting since structured neurophysiological network are revealed even if the person lying in the scanner has not been asked to do anything more cognitively demanding than simply to rest (Salvador et al., 2005). This observation suggests that some anatomically separated brain regions work together during rest and form functional networks, characterized by a high level of ongoing strongly correlated spontaneous neuronal activity.

2.2.1. BOLD contrast imaging

Magnetic resonance image contrast depends on the acquisition sequence of the image, since with a careful choice of radio frequencies and gradient pulse timing, it is possible to distinguish different tissue characteristics (Matthews et al., 2004).

Blood Oxygenation Level Dependent (BOLD) contrast is the basic principle on which rsfMRI is based. It allows the metabolic modifications of brain activity to be highlighted. Oxygenated (oxy) hemoglobin is a diamagnetic molecule, while deoxygenated (deoxy) hemoglobin is paramagnetic. Therefore, the presence of deoxyhemoglobin, which is prevalent in venous capillaries and venules, alters the local susceptibility to the MR magnetic field, introducing field inhomogeneities within and around blood vessels (Logothetis et al., 2004). An increase in neural brain activity causes an increase in cerebral blood flow. The higher metabolic consumption results in an incremented oxygen consumption rate. However, differently from what could be expected, oxyhemoglobin increased rate, due to augmented brain blood flow, is higher than the oxygen consumption.

Hence the local deoxyhemoglobin concentration decreases. An higher neural brain activity reduces magnetic field local distortions and local MR signal increases slightly, modulated through changes in T2*-weighted images, since the T2* time constant of signal decay is shortened by magnetic field inhomogeneity at microscopic scale. The consequent small signal increase due to activation is the BOLD signal (Buxton et al., 2004) and a schematic representation of the mechanism on which is based is shown in figure 2.3.
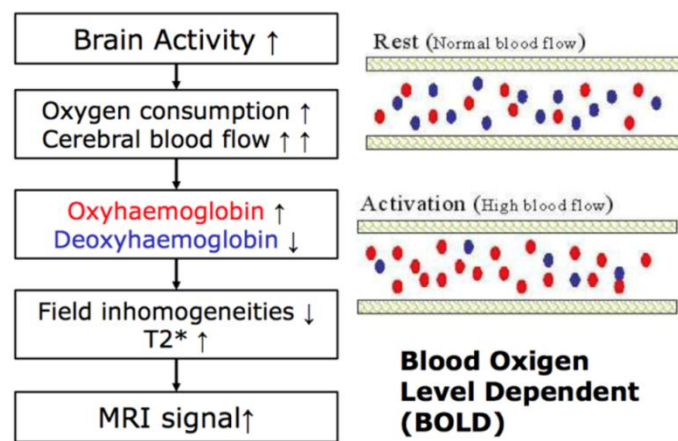
Figure 2.3 BOLD signal mechanism.

Temporal evolution of BOLD signal is delayed in respect with the neuronal activity due to the hemodynamic time lag in responding to the need of oxygen increase (Glover, 1999). BOLD signal time course is known as hemodynamic response function (HRF) (Fig 2.4).
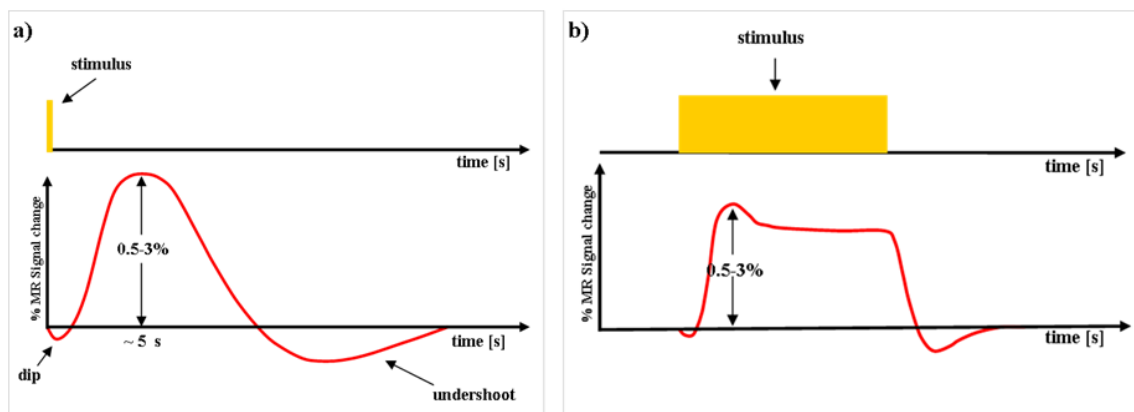
Figure 2.4 Hemodynamic response function to an impulsive stimulus (a) and to a step stimulus (b).

As it can be seen in figure 2.4, changes in BOLD signal with respect to its baseline are quite small (0.5%-3%). Moreover, this signal typically exhibits a temporal dynamics. The initial dip, lasting 1-2 seconds before the standard BOLD increase, is due to a transient augmentation of deoxyhemoglobin. After the plateau phase, a post-stimulus undershoot of the BOLD signal is observable for 30 seconds or more (Buxton, 2004).

BOLD signal is characterized by a poor signal-to-noise ratio, therefore employing statistical data analysis is necessary in order to extract the signals of interest (Beckmann, 2012). Moreover, in rsfMRI no external temporal reference is given, so the standard signal enhancement through linear regression of the stimulus or similar approaches is not feasible. Therefore, a blind source analysis of the data-set statistical structure, both spatial and temporal is needed. To achieve this goal, in this work we adopted the independent component analysis (ICA) approach, which will be described in details in the next paragraph.

2.2.2. RSNs Identification by ICA approach

Group rsfMRI studies have reported the existence of functionally linked sub-networks during rest, the resting state networks (RSNs), which consist of anatomically separated but functionally linked brain regions that show a high level of ongoing functional connectivity during rest (van den Heuvel et al., 2010). RSNs, though, are not directly identifiable from acquired rsfMRI data. Image preprocessing is necessary in order to highlight functional information of interest. Several methods to process rsfMRI have been proposed but they all can be roughly divided in 'seed methods' and 'data-driven methods'. The former examine the correlation between resting state time courses of a particular brain region (seed) and time series of all the other regions. The latter, such as PCA or ICA, enable to examine the whole brain connectivity without the need of *a priori* information (van den Heuvel et al., 2010). Specifically, ICA is a data-driven method that allows studying the intrinsic structure of the data. It is a particular implementation of the blind source separation (BSS) problem, namely the recovering of the signal components without using information about the source signals and their mixing process. The goal of ICA is expressing a set of uncorrelated variables as linear combinations of statistically independent components (Beckmann, 2012). ICA approach attempts to discover hidden underlying signals and statistically independent sources only from the measured observation that are unknown

linear mixtures of unobserved sources. ICA has been successfully applied for separating statistically independent BOLD components, associated with both, task-related and spontaneous resting state activity within neuronal networks (Abou-Elseoud et al., 2010) but it is particularly suitable for rsfMRI data (Beckmann, 2012). First of all, while principal component analysis (PCA) can identify activation patterns that are uncorrelated in both space and time, ICA can identify events that are independent in either time or space (Petersen et al., 2000). Moreover, ICA has an essential advantage over hypothesis-driven techniques (e.g., GLM) since it allows to differentiate functional brain signals from various sources of noise without any *a priori* knowledge about the signal origin (Abou-Elseoud et al., 2010).

ICA decomposes a two dimensional matrix (time × voxels) into a set of time courses and associated spatial maps, which jointly describe the temporal and spatial characteristics of underlying signals (Beckmann et al., 2005).

Formally, the problem set by ICA can be expressed as follows:

$$\bar{y} = \mathbf{F}\,\bar{z} \qquad\qquad\qquad \text{(Eq. 2.1)}$$

where $\bar{y}$ is the vector of observed random variables, $\bar{z}$ is the vector of the independent latent variables (the "independent components"), and $\mathbf{F}$ is an unknown constant matrix, called mixing matrix (Comon, 1994). Hence, the problem is to estimate both the mixing matrix $\mathbf{F}$ and the realizations of the latent variables z_i using observations of $\bar{y}$ alone. This problem is solved by iteratively optimizing $\mathbf{F}$ matrix, minimizing the mutual information of z_i (Correa et al., 2007). Two different ICA approaches can be performed to solve component and mixing matrix estimation: spatial ICA and temporal ICA. The former attempts to find spatially independent components with associated time course. The latter, aims at finding temporally independent time courses with associated spatial maps (Fig 2.5).
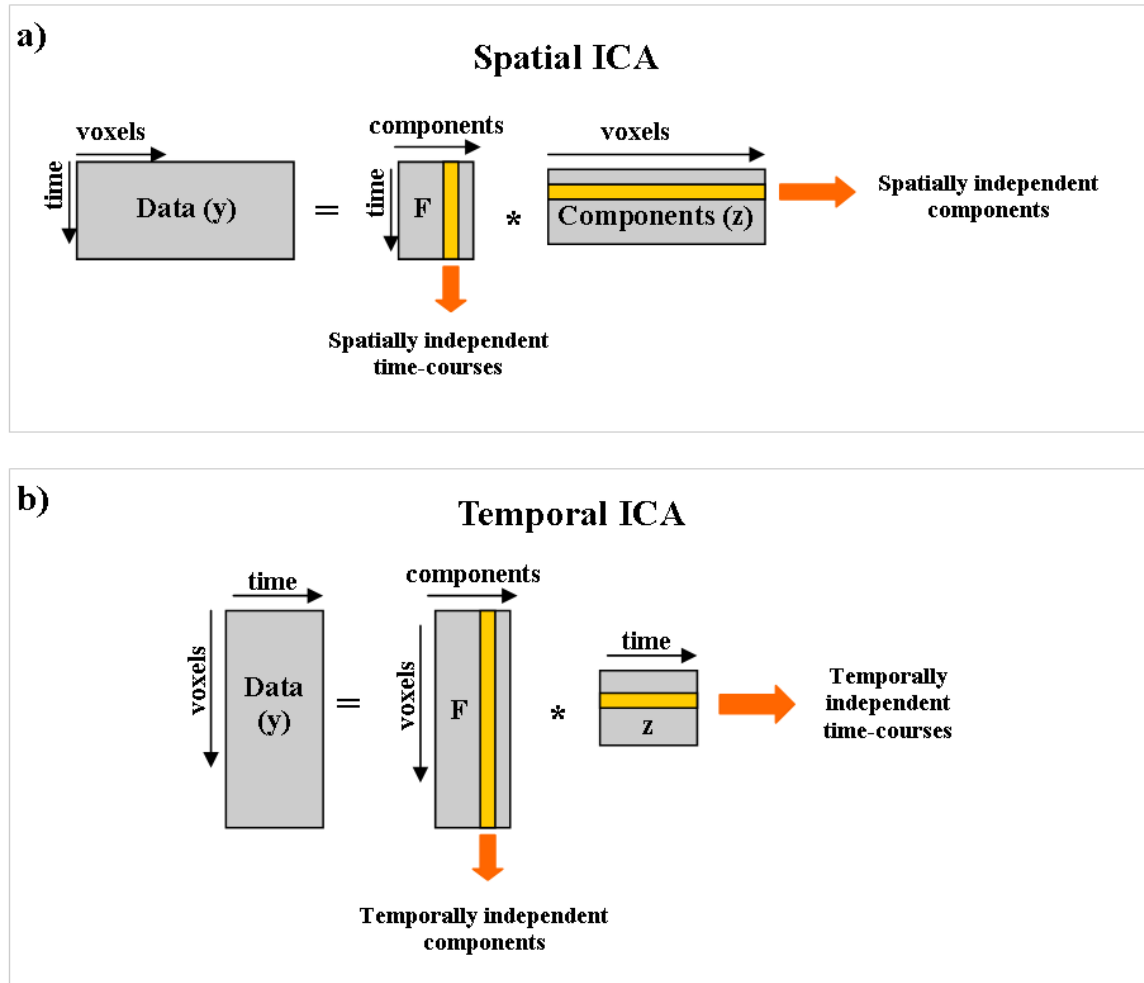
Figure 2.5 Matrix representation of the spatial ICA (a) and temporal ICA (b) approaches.

Spatial ICA, which has become the standard approach in neuroimaging (Dipasquale et al., 2015) and thus adopted in this work, can be extended to a probabilistic ICA model (pICA), which is implemented in many software packages (e.g., MELODIC, FSL toolbox used in this study) (Beckmann, 2012). This extension is performed by assuming that the p-dimensional vectors of observations (time series in the case of rsfMRI data) are generated form a set of q ($<$ p) statistically independent non-Gaussian sources (spatial maps) via a linear and instantaneous mixing process corrupted by additive Gaussian noise $\eta(t)$:

$$\bar{y}_i = \mathbf{F}\,\bar{z}_i + \bar{\eta}_i \qquad\qquad \text{(Eq. 2.2)}$$

where $\bar{z}_i$ denotes the non-Gaussian source signals contained in the data and $\bar{\eta}_i$ denoted Gaussian noise $\bar{\eta}_i \sim G(0,\ \sigma^2 \Sigma_i)$. Solving the BSS problem requires to find a linear transformation matrix $\mathbf{W}$ such that

$$\hat{z} = \mathbf{W}\,\bar{y} \qquad\qquad \text{(Eq. 2.3)}$$

35

is a good approximation to the actual source signals z (Beckmann et al., 2005).

pICA estimates independent components from the data as shown in figure 2.6 and as explained hereunder.
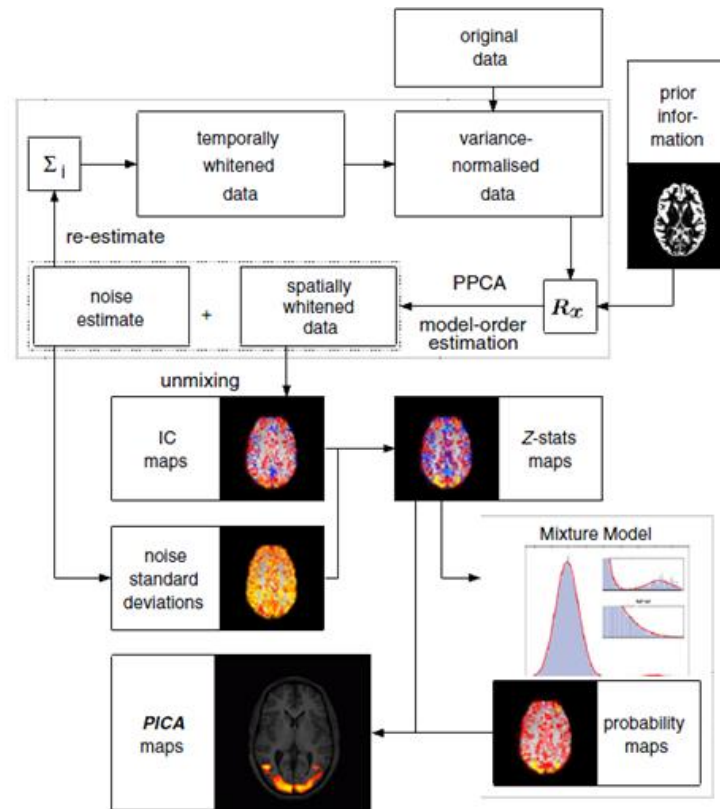
Figure 2.6 Schematic of the probabilistic ICA model (Beckmann et al., 2004).

First of all, original data are demeaned and normalized in order to have the same noise variance across space. Since variance normalization requires the knowledge of the signal but we don't have any *a priori* information about it, normalization and probabilistic PCA (PPCA) are iteratively performed to split the total data space into initial noise and signal sub-spaces. In this case, PPCA is implemented for the model order estimation, the noise is used to reiterate and refine the normalization steps and the independent component maps are estimated from the preprocessed data. Then, the estimated component maps are transformed to voxel-wise Z-statistics maps by dividing raw component maps with the standard deviation of the residuals obtained from the probabilistic PCA. Finally, these maps are thresholded in order to identify voxels that are significantly modulated by the component time courses. The threshold choice is based on the histogram of the components (Beckmann, 2012).

2.3. DWI: basic principles

The diffusion is a physical process that involves fluid molecules, which follow Brownian motion. Specifically for the water molecules, if they move in a solution without constraints, they diffuse isotropically and their random motion is influenced only by diffusion coefficient, namely by their molecular weight, intermolecular interaction (i.e., viscosity) and temperature (Beaulieu, 2002).

Diffusion weighted magnetic resonance imaging (DWI) takes advantage of this physical process in order to study tissue microstructure (Jones, 2008). The underlying cellular structure, indeed, affects the overall mobility of diffusing molecules by providing numerous barriers and by creating various compartments (e.g., intracellular and extracellular space, neurons, glial cells, axons, *etc*), which hinder diffusion and define preferential directions for the motion (Beaulieu, 2002). In particular, since neuron axons are highly straight structures, DWI is suitable for white matter (WM) studies, especially when any change in cellular structures alters the water molecules displacement per unit time (Jones, 2008). Hence, DWI allows an indirect observation of the water molecule diffusion by encoding this information in signal changes (Stejskal and Tanner, 1995). The diffusion weighting is obtained by means of an additional bipolar gradient pulse. If spins phases, which are voxel dependent, are set, and then diffusion occurs, protons shuffling among neighboring voxels causes a loss of signal coherence and thus a reduction in signal amplitude (Fig. 2.7). Echo time (TE) must be long enough to let the diffusion occur.
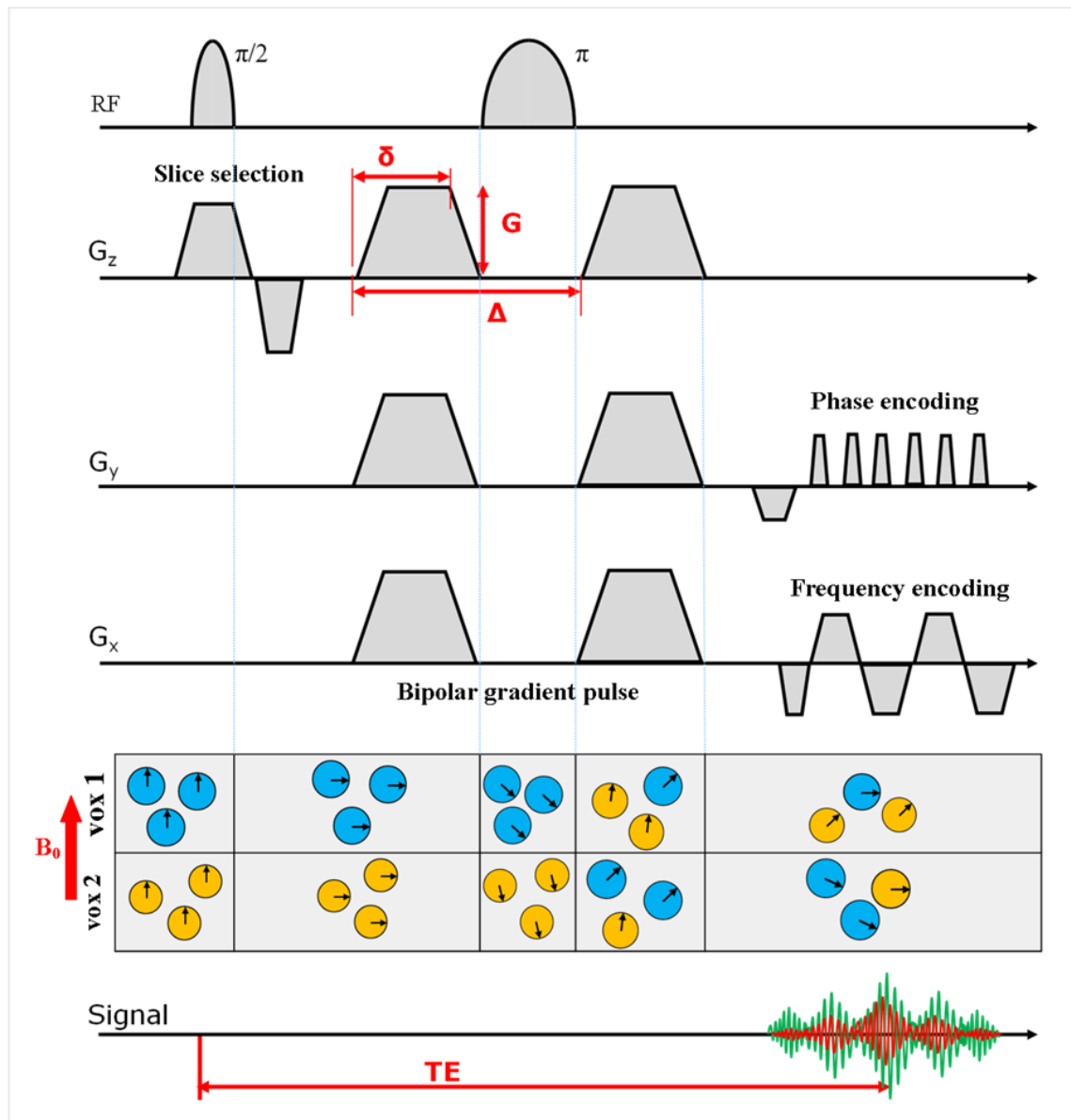
Figure 2.7 Diffusion weighted sequence by bipolar gradient pulse and EPI. If diffusion occurs, water molecules move to neighboring voxels and signal coherence is lost. In this case, recorded signal amplitude (in red) is lower than signal recorded when diffusion doesn't occur (superimposed in green).

Signal amplitude reduction is described by the following equation:

$$\frac{S}{S_0} = e^{-\gamma^2 G^2 \delta^2 \left(\Delta - \frac{\delta}{3}\right) ADC} = e^{-b\,ADC} \qquad \text{(Eq. 2.4)}$$

where S is the diffusion weighted signal, S_0 is signal obtained when diffusion doesn't occur (T2-weighted image), γ is gradient echo duration, G is gradient pulse amplitude, Δ is

diffusion time, *δ* is gyromagnetic ratio, *b* represents the diffusion sensibility level and *ADC* is the apparent diffusion coefficient. ADC is a coefficient that replaces the diffusivity coefficient in biological tissues diffusion phenomenon description, since it considers also the effect of water molecules interactions with cellular structures. ADC is directionally dependent (Jones, 2008). In isotropic tissues, the water molecules move equally in all directions and ADC is a single constant. In non-isotropic tissues, instead, ADC reflects tissue microstructure due to the diffusion directions. Therefore, in the voxels containing non-homogeneous biological microstructures, different signals are recorded for different gradient directions. Hence, it is important to acquire brain volumes using various gradient directions (six, at least) in order to obtain many ADC maps and to avoid information loss.

2.3.1.DTI-based tractography

It should be clear now that, when dealing with biological tissues with oriented structures like WM, we cannot describe water molecular behavior with a single ADC coefficient per voxel. Therefore, diffusion characterization requires a tensor in every voxel which fully describes the molecular mobility along each direction and correlation between these directions (Fig 2.8) (Le Bihan et al, 2001). Diffusion imaging is then replaced with diffusion tensor imaging (DTI).
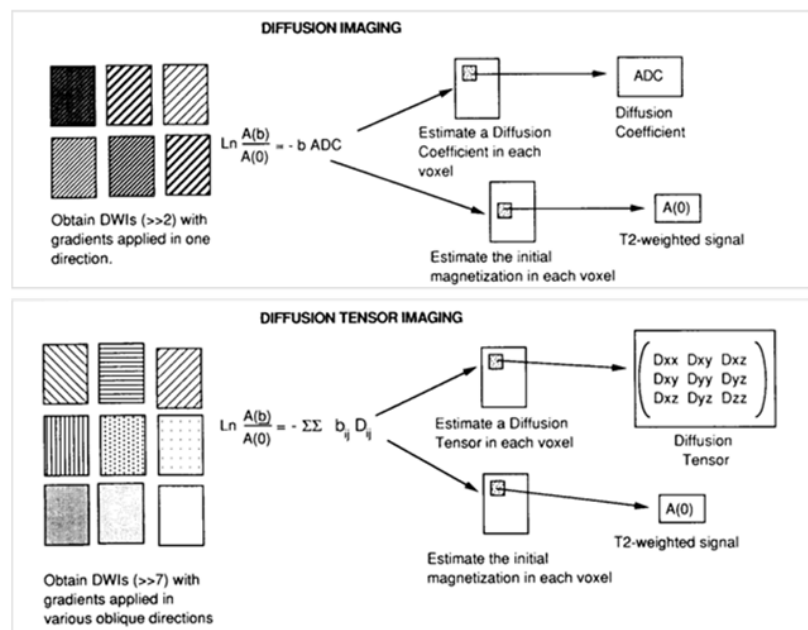
Figure 2.8 Diffusion imaging (upper panel) and diffusion tensor imaging (lower panel). (Basser, 1995)

Diffusion tensor is a 3×3 symmetric matrix which models the local diffusion as a 3D Gaussian distribution (Behrens et al, 2003). Displacement profile is thus represented by an ellipsoidal envelope (Fig 2.9), whose principal axes are given by the tensor eigenvectors (Jones, 2008).
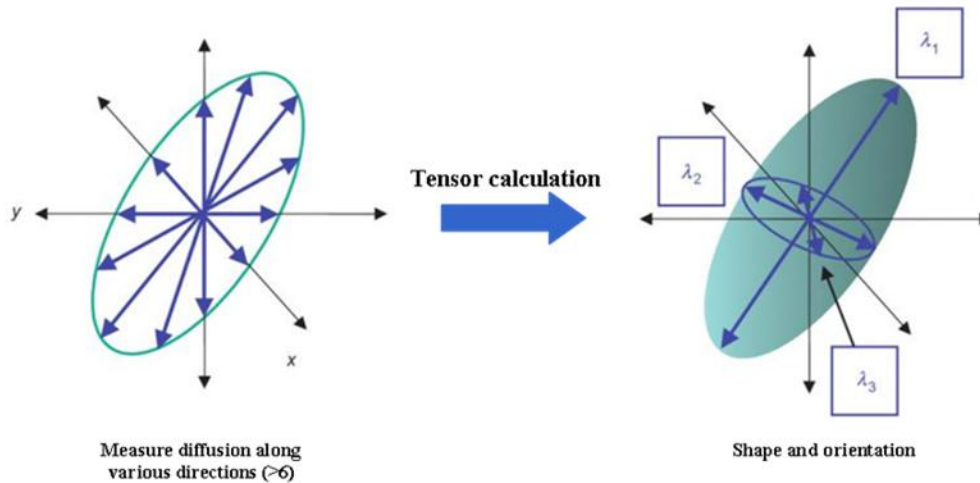
Figure 2.9 Diffusion ellipsoid. Principal axes are given by eigenvectors and their respective eigenvalues λ_1, λ_2, λ_3 (Mori et Tournier, 2014).

The three eigenvalues and the associated eigenvectors define tensor shape and orientation (Behrens et al, 2003), hence two invariant diffusion indices are derived from these parameters: mean diffusivity (MD) and fractional anisotropy (FA).

$$\text{MD} = \frac{\lambda_1 + \lambda_2 + \lambda_3}{3} \qquad \text{(Eq. 2.5)}$$

$$\text{FA} = \sqrt{\frac{3}{2} \frac{(\lambda_1 - \text{MD})^2 + (\lambda_2 - \text{MD})^2 + (\lambda_3 - \text{MD})^2}{\lambda_1^2 + \lambda_2^2 + \lambda_3^2}} \qquad \text{(Eq. 2.6)}$$

where λ_1, λ_2 and λ_3 are tensor eigenvalues.

The most useful application of DTI acquisition is tractography, which allows to reconstruct the trajectories of WM bundles by piecing together discrete estimates (i.e., voxel-based) of the underlying continuous fiber orientation field (Jones, 2008). According to the method used for fiber reconstruction, tracking algorithms are defined as deterministic or probabilistic approaches. DTI-based tractography uses deterministic tracking algorithms,

since streamlines generation is sharply based on the local maximum eigenvector direction. The main assumption underlying the single-tensor deterministic tractography, is that in each voxel the principal eigenvector is parallel to the dominant fiber orientation (Jones, 2008). Therefore, virtual fibers are reconstructed starting from a seed-point and moving forward following the principal direction defined by the eigenvector associated to the higher eigenvalue. Stopping criteria are needed to reduce sensitivity to noise and partial volume effects: for DTI data, FA threshold (usually 0.2-0.5) and local curvature threshold (commonly 45°) are introduced (Behrens et al., 2003). An example of DTI-based tracking and associated stopping criteria is shown in figure 2.10.
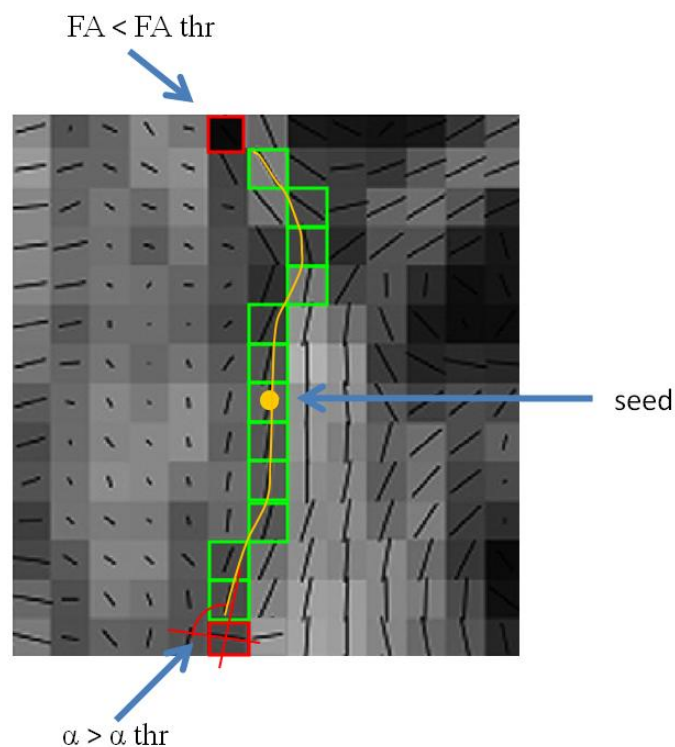
Figure 2.10 Stopping criteria in deterministic single tensor DTI-based tractography. The image represents a FA map in gray scale from white (i.e., FA=1) to black (i.e., FA=0). In each voxel the principal direction is represented by black lines. The yellow spot represents the seed point and the yellow line is the streamline tracked starting from the seed point. Green boxes highlight the path followed while red boxes show the points where stopping criteria occur.

The main limitation of DTI is the impossibility to recognize bending, branching, crossing and kissing fibers (Fig 2.11). Tensor model is unsuitable to describe fiber orientation when there is more than one fiber population within a voxel because each voxel is described by a

single tensor (Jones,2008). In these cases, since the tensor represents the average voxel structure, FA values decrease, leading to an incomplete fiber characteristic delineation.
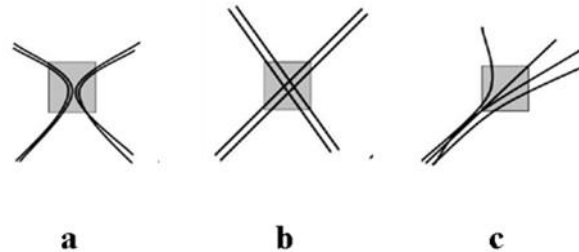
Figure 2.11 a) Kissing fibers. b) Crossing fibers. c) Branching fibers.

In the context of the deterministic algorithms, more complex models than the single tensor one, allow to detect multiple principal fiber direction in each voxel, basing on the exploration of an increased number of directions. Multi-tensor model, spherical deconvolution, q-ball analysis, HARDI, *etc* are examples of the techniques which adopt this approach. Another way to address the problem is adopting a completely different methodology, namely defining a multi-compartmental model and using probabilistic algorithms. In the next paragraph, the latter approach will be described.

2.3.2. Probabilistic tractography

Several techniques (Lazar and Alexander, 2005; Tournier et al, 2004; Tuch et al, 2004) have been proposed to describe local diffusion within an image voxel without imposing the Gaussian constraint, commonly used in tensor model approaches (Beherens et al, 2007). Indeed, there is an uncertainty in diffusion parameters estimation which is caused not only by noise and artifacts but also by the incomplete modeling of diffusion signal (Beherens et al, 2003). This uncertainty is not uniform throughout the brain (Jones, 2003). Dense WM areas, characterized by a single principal fiber direction, present low uncertainty and the diffusion single tensor model is complex enough to estimate diffusion parameters. On the other hand, low anisotropy areas, or rather, voxels in which fibers cross, kiss or branch into gray matter, are characterized by high uncertainty in fiber detection.

This problem can be addressed by increasing the model complexity. A possible solution is defining a partial volume model which fits in each voxel a distribution of fiber orientations

$H(\theta,\varphi)$, where θ, φ represents fiber direction in spherical polar coordinates (Behrens et al., 2003). This model assumes that each voxel may be divided in sub-voxels and that each sub-voxel can be described by a simple two-compartment partial volume model. The first compartment models diffusion phenomenon in the fiber directions (anisotropic compartment) while the second one models the isotropic diffusion of free water (Behrens et al., 2003). Therefore, signal related to each sub-voxel can be described as follows:

$$\mu_i = S_0 ((1-f) \exp(-b_i d) + f \exp(-b_i d r_i^T R A R^T r_i)) \qquad \text{(Eq. 2.7)}$$

where d is diffusivity, b_i and r_i are the b-value and gradient direction associated with the ith acquisition, f and RAR^T are the fraction of signal contributed by the fiber direction (θ, φ), A is defined as:

$$\begin{bmatrix} 1 & 0 & 0 \\ 0 & 0 & 0 \\ 0 & 0 & 0 \end{bmatrix} \qquad \text{(Eq. 2.8)}$$

and R rotates A to (θ, φ) (Behrens et al., 2003). The first part of Eq. 2.7 represents the signal due to the isotropic compartment while the second one refers to the anisotropic compartment.

Thus, the MR signal from each voxel at each gradient direction may be express as the sum of its sub-voxels signals:

$$\mu_{tot} = \Sigma_{j \in subvoxels} \; \mu_j \qquad \text{(Eq. 2.9)}$$

If we consider the set of principal directions (θ, φ) instead of the single sub-voxels, previous equation is equivalent to:

$$\frac{\mu_i}{S_0} = (1 - f)\exp(-b_i d) + f \int_0^{2\pi} \int_0^{\pi} H(\theta, \varphi)\exp(-b_i d r_i^T R_{\Theta\Phi} A R_{\Theta\Phi}^T r_i \sin(\theta)d\theta d\varphi)$$

$$\text{(Eq. 2.10)}$$

where μ_i is the signal associated to the ith acquisition and $H(\theta,\varphi)$ is the distribution of fibers within the voxel (Behrens et al., 2003).

Probabilistic diffusion tractography is a tractographic reconstruction technique, which is based on this partial volume model. In fact, local probability density functions (pdfs), obtained from the simple partial volume model, are used to infer on a model of global connectivity with the aim of maximizing the chances of complex fiber structure to be represented by principal direction uncertainty (Behrens et al., 2003).

The main difference between various probabilistic algorithms is the mechanism by which samples are drawn from the inherent distribution of fibers orientations (Jones, 2008), such as Bayesian methods (Behrens et al., 2003) and bootstrapping methodologies (Jones and Pierpaoli, 2005; Lazar and Alexander, 2005). Specifically, in Bayesian approaches the pdf is appointed as "posterior distribution on the parameters given the data" and expresses as:

$$P(\omega|Y, M) = \frac{P(\omega|Y,M)P(\omega|M)}{P(Y|M)} \qquad \text{(Eq. 2.11)}$$

where ω is the set of parameters, Y is the data and M is the model. The computation of P(ω|Y,M) is often analytically impossible. A numerical solution to this problem consists in drawing samples from P(ω|Y,M) (Behrens et al., 2003). Generally, Markov Chain Montecarlo (MCMC) is the used sampling technique.

Regardless from the sampling technique, probabilistic tractography final result always represents a probabilistic map, which defines the confidence interval of the location of the most probable single connection between seed and target regions (Jones, 2008). In fact, tracking does not progress just along the most likely principal diffusion direction. Since a high number of possible (θ,φ) is available for each voxel, every tracking step evaluates all the possible connection between voxels considering numerous different diffusion directions (Lilja et al, 2013). Therefore, streamlines become samples from the connectivity distribution and, after drawing a large number of independent samples, we are able to compute the probability of the dominant streamline. The value of each voxel of the final probabilistic map identifies the number of streamlines that passes through it (Behrens et al.,2007).

Probabilistic tracking termination criteria tend to be slightly different from deterministic algorithm ones (Jones, 2008). Since probabilistic algorithms are not dependent on a unique

principal diffusion direction, it is not necessary to include FA threshold as termination criteria (Jones, 2008). For the same reason, the bending angle threshold is less restrictive too, generally around 80° (Behrens et al.,2003).

One of the main advantages of probabilistic tractography is a high ability in detecting bending, crossing and kissing fibers, not only due to less restrictive stopping criteria but also because the partial volume model allows to detect more than one fiber in each voxels (Jones, 2008) (figure 2.12).
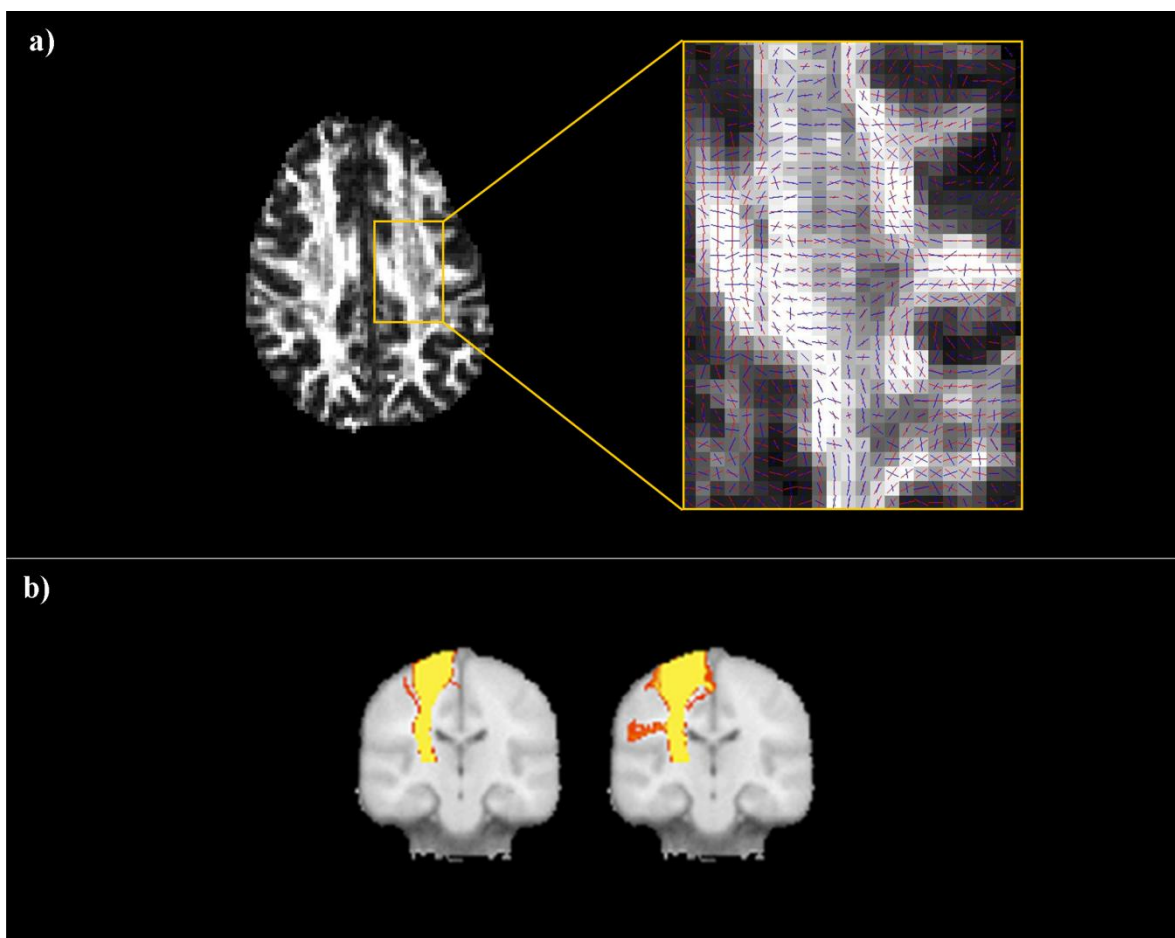
Figure 2.12 Crossing fiber modelling by multi-fiber probabilistic tractography. **a)** Axial close up of crossing fibre bundles with dominant fibre orientation in red and the second one in blue. Shown directions are the mean vectors of the posterior distribution samples. **b)** Tracking the cortico-spinal tract from the internal capsule to the primary motor cortex with single fibre (left) and multi-fibre (right) tractography (Behrens et al,. 2007).

Further, probabilistic tractography is quite robust to noise since wrong paths are classified with low probability (Behrens et al.,2003). As counterpart, it may lead to false positive streamline detection. In order to reduce them, it is necessary to select an appropriate threshold, below which connections are discarded as unlikely (Lilja et al, 2014). Other drawbacks of probabilistic tractography are the less intuitive result interpretation than DTI-based tractography and a strong dependence on the seed dimensions.

2.4. fMRI-guided and rsfMRI-guided tractography

fMRI provides a detailed information about the spatial location of the functionally active cortical areas (Kim et al.,2005). Conversely, tractography is a powerful *in vivo* and non-invasive tool for exploring WM structure and investigating the brain anatomical features. Hence, combining these techniques in a specific brain circuitry may yield to obtain a further insight into the correlation between the structural connections and the functional responses. One of these combination approaches is fMRI-guided tractography.

fMRI-guided tractography consists in using functional activation areas as regions of interest (ROIs) in tractography. Therefore, anatomical landmarks commonly used for fiber selection are replaced by functional landmarks, which are the spatial patterns of the fMRI response (Preti et al., 2012). Before defining them as seed regions in tractography, ROIs are generally dilated in order to reach WM from the GM activated areas.
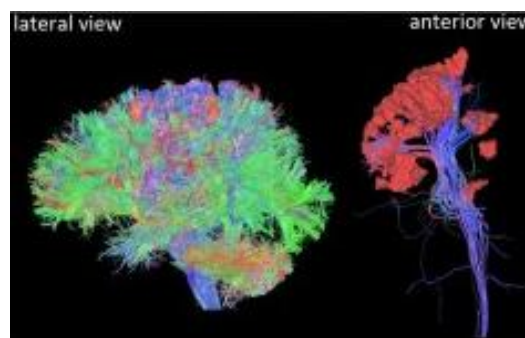

Figure 2.13 Functional tract derived from fMRI activation sites during a finger-tapping task (on the right). The whole subject tract is represented on the left (Bernier et al., 2014).

This multimodal approach allows not only to improve neurophysiologic knowledge about functional and structural connectivity relationship, but also to clinically investigate

neurodegenerative pathologies or brain lesions effects, since the activated cortical area, which are adopted as ROIs for tractography, are altered in brain disorders. Indeed, fMRI-guided tractography allows overcoming a critical aspect of tracking, namely the definition of an appropriate seed region, since anatomical landmarks are prone to large inter-subject anatomical variations (Staempfli et al., 2008). Moreover, by using fMRI activation areas as seed regions we can avoid the operator-dependence of seed ROI delineation.

Recently, due to the increasing interest in studies about the relationship between functional connectivity (FC) and structural connectivity (SC), also rsfMRI activated areas have been used to drive fiber tracking (figure 2.14) (Damoiseaux et al., 2009; Greicius et al., 2009). We refer to this technique as rsfMRI-guided tractography.
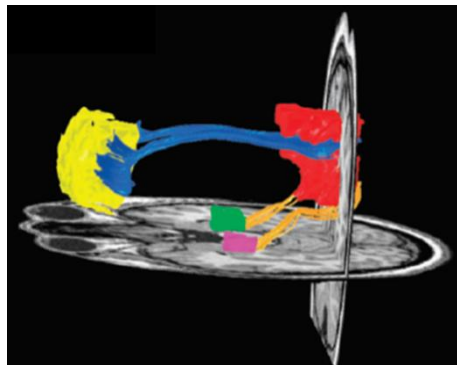
Figure 2.14 Results of rsfMRI-guided tractography run using DMN areas as regions of interest (Greicius et al., 2008).

This method allows to evaluate FC and SC between exactly the same ROIs, thus, in the same conditions. It is possible then comparing and integrating FC and SC results to address connectivity issue with a complete multimodal approach.

2.5. Conclusion

In conclusion, the present work aim at combining the above illustrated methods: the clusters of voxels identified within RSNs, previously extracted by ICA, are used as ROIs in rsfMRI-guided tractography based on the probabilistic approach. Since these clusters can be seen as nodes of both functional and anatomical networks, this method intends to compare the two basic types of connectivity both at single and group level.

Chapter 3

Materials and Methods

In this chapter the procedures adopted for the image acquisition and processing are presented in detail. Data analysis was performed in the Magnetic Resonance Lababoratory of Don Carlo Gnocchi Foundation, IRCCS "Santa Maria Nascente" in Milan.

In the first part an overview on the image acquisition protocol is presented (par. 3.1).

The second section (par. 3.2) deals with the description of resting state functional magnetic resonance imaging (rsfMRI) data preprocessing, which included cleaning, identification of resting state networks (RSNs) and their subdivision in clusters, based on anatomical information. Further, functional connectivity estimation within these sub-networks is described.

To follow (par. 3.2), diffusion weighted imaging (DWI) data processing is presented, highlighting all the performed steps (i.e., eddy current correction, B-matrix rotation, diffusion parameters estimation, probabilistic tracking). Afterwards, structural connectivity problem and tracts probabilistic maps construction are addressed.

Further on, a novel methodological approach to correlate functional and structural brain connectivity is presented (par 3.4).

3.1. Subjects and data acquisition

3.1.1. Subjects and ethic statement

Twenty healthy right-handed voluntary subjects were recruited for this study. Age between 29 and 66 years was defined as inclusion criteria, in order to focus the study on a middle-aged sample. Movement artifacts and image corruption were considered as exclusion criteria. Therefore, all subject images were visually checked before starting the preprocessing procedure. All subjects that did not meet every defined criteria were excluded from the analysis.

Written informed consent was obtained from all participants according to the ethical principles of the Helsinki Declaration. The study was approved by the Don Gnocchi Foundation Ethics Committee. Resting state fMRI, DWI and MPRAGE data were acquired on a 1.5 Tesla scanner (Siemens Magnetom Avanto, Erlangen, Germany). During the resting state recordings, the subjects were instructed to relax and keep their eyes closed without falling asleep. All subjects were scanned in a single session without changing their position.

3.1.2. Image acquisition

Resting state images were acquired during a period of 8 min using a gradient echo planar T2* sequence (TR = 2500 ms, TE = 20 ms, voxel size = $3.125 \times 3.125 \times 2.5$ mm^3, matrix size = 64×64, FOV = 200 mm x 200 mm, number of axial slices = 39, number of volumes = 190).

In the same scanning session, a set consisting of 30-weighted diffusion scans (b-value=1000 s/mm^2) and one non-weighted scan (b-value = 0 s/mm^2) were acquired with a diffusion weighted pulsed-gradient spin-echo planar sequence (TR = 6700 ms, TE = 99 ms, voxel size = 1.9 x 1.9 x 2.5 mm^3, matrix size = 128×128, FOV = 240 mm $\times$ 240 mm).

In addition, 3D T1-weighted Magnetization Prepared Rapid Acquisition Gradient Echo (MPRAGE) (TR = 1900 ms, TE = 3.37 ms, TI = 1100 ms, flip angle = 15∘, resolution= 1 mm $\times$ 1 mm$\times$ 1 mm, matrix size = 192×256, FOV = 192 mm x 256 mm, number of axial slices = 176) was acquired as anatomical reference.

3.2. rsfMRI: image processing and functional connectivity

3.2.1. rsfMRI data preprocessing

rsfMRI data preprocessing was performed with different FSL 3.0 packages. MELODIC (Multivariate Exploratory Linear Optimized Decomposition into Independent Component) (http://fsl.fmrib.ox.ac.uk/fsl/fslwiki/MELODIC) was used to decompose multiple 4D dataset into different spatial and temporal components (Beckmann and Smith, 2004). FIX (FMRIB's ICA-based Xnoiseifier) was adopted for the signal classification, namely for separating actual signal and noise component. FLIRT (FMRIB's Linear Image Registration Tool) and FNIRT (FMRIB's non-Linear Image Registration Tool) were finally used for the image registration in the Montreal Neurological Institute (MNI) standard space.

MELODIC preprocessing :

- **Motion correction**, performed with MCFLIRT (Jenkinson et al., 2002).
  In rsfMRI, motion correction is a very awkward issue because the slightest head movement during a scan may bring the same voxel of two contiguous volumes not to correspond to the same physical point. In addition, the magnitude of the signal changes caused by head movements may result greater than the blood oxygenation level dependent (BOLD) activation response. Therefore, standard processing consists in estimating motion parameters and realigning the raw data. MCFLIRT is an intra-modal motion correction tool, designed for fMRI time series and based on optimization and registration techniques realized by FLIRT (Jenkinson et al., 2001). FLIRT is a fully automated robust and accurate tool for linear (affine) intra/inter-modal brain image registration in spaces different from the native ones.
- **Brain extraction**, performed with BET (Smith, 2002).
  BET deletes non-brain tissue from an image of the whole head.
- **Spatial smoothing**, performed with a 5 mm full width at half maximum (FWHM) Gaussian kernel. Spatial smoothing was used to reduce the random noise and improve the signal-to-noise ratio. A 5 mm FWHM was chosen as compromise

between the increase of sensitivity to detect true activations and the functional image spatial resolution reduction.

- **High-pass temporal filtering**, performed with cut off frequency equal to 0.01 Hz. RSNs functional connectivity originates from signals which fluctuate not only at a frequency around 0.1 Hz but also at higher frequencies linked to underlying broadband neuronal processes (Niazy et al., 2011; Smith et al., 2012). In this study a high-pass temporal filter was used instead of a band pass filter, in order to improve the signal to noise ratio without cutting parts of the actual signals. An example of raw data and preprocessed images is shown in figure 3.1.
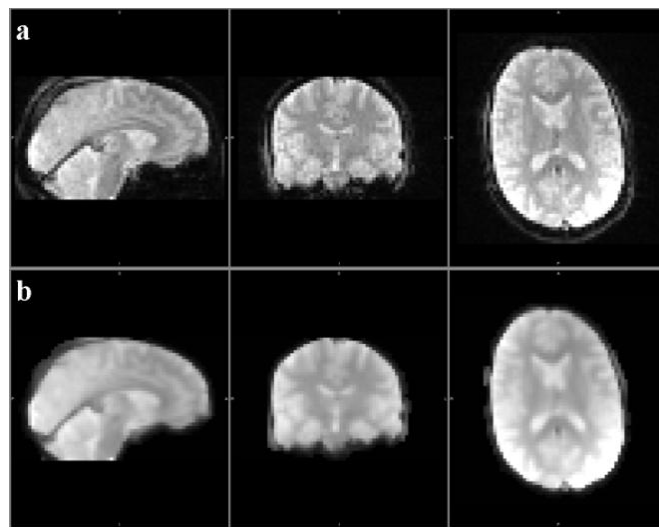
Figure 3.1 (a) Raw rsfMRI image; (b) preprocessed rsfMRI image.

- **Single-subject spatial ICA**, performed with automatic model order estimation. The input data were reshaped as a 2D time×space matrix. MELODIC decomposes this matrix into pairs of time courses and spatial maps, one for each component. Hence, the original data are assumed to be the product between the matrix of the time courses and the spatial maps associated to the estimated components (Fig. 3.2).
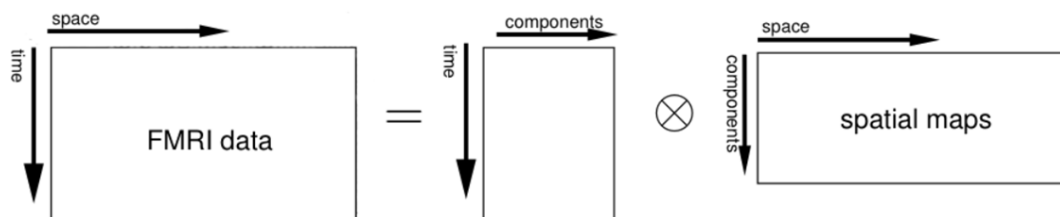
Figure 3.2 Matrix representation of single subject spatial ICA

FIX preprocessing

The components individuated by MELODIC (Beckmann and Smith, 2004) are both actual signal and noise components. Using FIX (Griffanti et al., 2014) we automatically addressed the discrimination between noisy and "good" ones on the basis of a training dataset of hand-labeled components. FIX removed the contribution of artifactual components and returned de-noised data.

FLIRT-FNIRT preprocessing

Filtered and de-noised rsfMRI images need to be registered to a standard space in order to allow single subject comparison and group analysis. Registration was performed in two steps:

- data registration to their respective high-resolution structural brain images (T1-3D) using FLIRT linear registration (Jenkinson et al., 2001). The structural brain images were generated from T1-weighted MPRAGE data by means of the fsl_anat function (http://fsl.fmrib.ox.ac.uk/fsl/fslwiki/fsl_anat). The obtained brain images were visually checked slice by slice and manually corrected if necessary;
- registration to the MNI152 standard space ($2x2x2$ mm^3 resolution) using FNIRT non linear transformation (Andersson et al., 2010). The MNI152 standard space is a T1-weighted average structural image derived from 152 subjects, created by the Montreal Neurological Institute.

An example of data before and after registration is shown in figure 3.3.
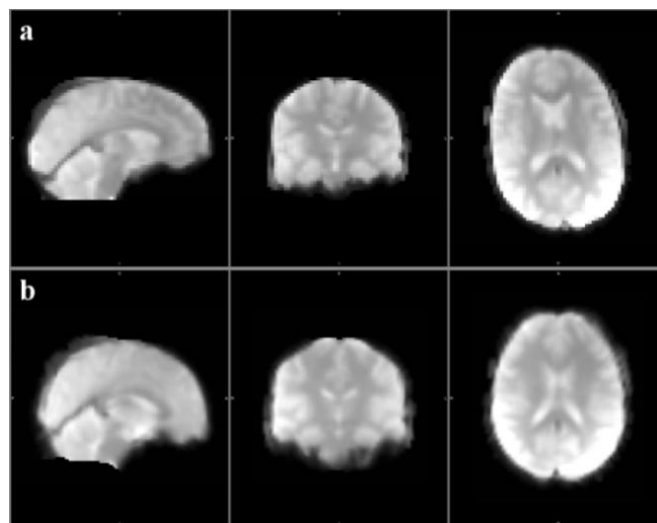

Figure 3.3 (a) Filtered rsfMRI data; (b) filtered rsfMRI data registered to MNI space.

3.2.2. rfMRI data processing

Group-ICA and cluster identification

Using MELODIC, the group-ICA was performed to look for common spatial patterns across subjects. First of all, space×time matrices are temporally concatenated across subjects obtaining a unique matrix. Concatenation approach is particularly useful when the signals of interest are not expected to have similar time courses in all subject datasets (Filippini et al., 2009; Beckmann et al., 2009). Then, the group-ICA decomposes this unique matrix into independent components (Fig. 3.4).
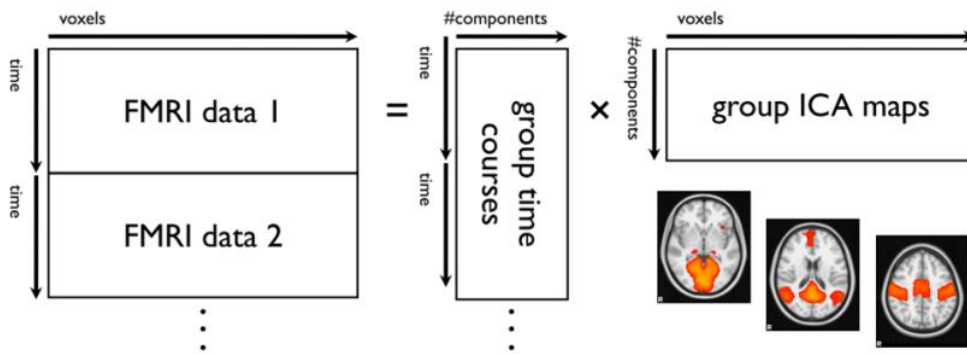
Figure 3.4 Matrix representation of temporal concatenation group-ICA (Beckmann et al., 2009).

The number of components (i.e., dimensionality) in which decomposing the signal was set to 30, since this allowed to better identify the RSNs of interest.

Each component was manually classified in order to select the default mode network (DMN), left lateral network (LLN) and right lateral network (RLN), subsequently split in sub-networks as described below:

- RSN images binarization;
- image labelling, using *cluster* function (http://fsl.fmrib.ox.ac.uk/fsl/fslwiki/Cluster) to associate different intensities to blobs anatomically separated;
- clusters thresholding, to remove spurious signal components;
- RSN original image masking with the created clusters, to split them in their sub-networks.

The identified clusters were considered to be relevant since they correspond to DMN, RLN and LLN clusters in a well-estabilished template (Smith et al., 2009). These sub-networks

were used as regions of interest (ROIs) for the next analysis concerning both, functional and structural connectivity.

Dual regression

Dual regression was performed with *dual regression* function (http://fsl.fmrib.ox.ac.uk/fsl/fslwiki/DualRegression) to generate a subject-specific spatial maps from the set of spatial maps obtained with group-ICA (Filippini et al., 2009; Beckmann et al., 2009). Specifically, group ICA spatial maps were used as spatial regressors in general linear model (GLM) (Fig. 3.5) to calculate the set of subject-specific time series by a last square criterion. These data were stored in a text file (one for each subject) where the n-th column represented the temporal dynamic associated to the n-th component in the GLM input data.

All the good ICs were used as spatial regressors in GLM. The reason why we included all the good ICs in the estimation of the time courses associated to the cluster of interest was to not introduce a bias in the estimation. In fact, if we had used only the clusters of interest as regressors, we would have forced the model to attribute to these clusters more signal than the actual one.
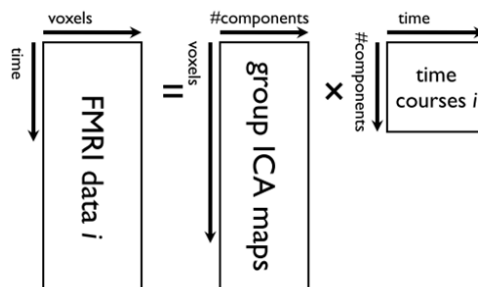
Figure 3.5 Dual regression: time courses extraction (Beckmann et al., 2009).

3.2.3. Functional connectivity

The functional connectivity (FC) among the identified clusters was calculated as correlation (i.e., Pearson full correlation coefficient 'r') by means of FSLnets tool provided in FSL package (http://fsl.fmrib.ox.ac.uk/fsl/fslwiki/FSLNets). For each subject, FSLNets estimates the correlation between the time series associated to the group ICA sub-networks of interest. Single subject correlation data were stored in matrices called FC matrices.

Averaging single subject FC matrices, a group FC matrix for each RSN was obtained (Fig. 3.6).
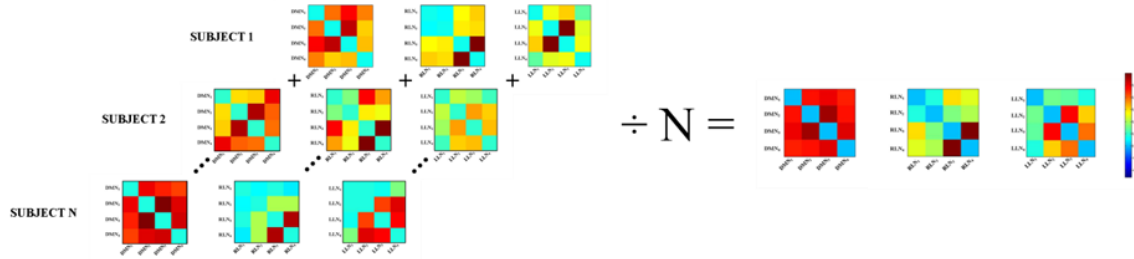
Figure 3.6 Group FC matrices calculation from single-subject FC matrices. FC is expressed as *r*. N = number of subjects.

Functional connectivity index could be expressed either as Pearson correlation coefficient ($r \in [-1,+1]$) or transformed into z-scores ($z \in [0,\infty)$). The relationship between r and z is:

$$z = \frac{1}{2} \ln\left(\frac{1+r}{1-r}\right)$$ (Eq. 3.1)

In this study z-scores was chosen as FC index in order to improve normality through the Fisher z-transform (Fisher, 1921) and to make this index suitable for statistical comparisons. Hence, z-score functional connectivity matrices were generated from the respective full correlation matrices. Functional connectivity matrices (both expressed through full correlation and z-score) were represented as images in order to visually highlight the highest values.

3.3. DWI: image processing and structural connectivity

3.3.1 DWI Data Preprocessing

Eddy current correction and B-matrix rotation

Firstly, DWI data were corrected for gradient coil eddy current distortions. This is a fundamental step to avoid stretches and shears in the diffusion weighted images by means of an affine registration to a reference volume (b = 0). The distortions are different depending on the gradient directions. Secondly, the B-matrix was reoriented by realigning

the diffusion weighted images to correctly preserve the orientation information (Leemans et al., 2009).

Bayesian estimation of diffusion parameters obtained using sampling techniques

The estimation of diffusion parameters (θ,Φ) (i.e., the principal diffusion direction in spherical polar coordinates) and the anisotropic volume fraction was performed with bayesian estimation of diffusion parameters obtained by 'bedpostx' (FMRIB's Diffusion Toolbox - FDT v2.0) tool provided in FSL package (Behrens et al, 2003).

Regarding the parameter estimate, bayesian approach is completely different from the deterministic criterion used in DTI techniques. Specifically, the deterministic approach looks for the set of parameters that best fit the data, while the bayesian method associates a probability density function (pdf) to the parameters (par 2.3.2).

In this study two fibers per voxel were modeled to allow crossing fibers detection. Each fiber was weighted by a unitary multiplicative factor so that none of the two directions was supposed to be more probable that the other one. The number of the iterations to be performed before starting sampling was set to 1000. This default value was estimated to be high enough for convergence. BedpostX returned 4D volumes representing the samples from the distribution on the principal diffusion direction in spherical polar co-ordinates (θ,Φ) and the samples from the distribution on anisotropic volume fraction. These 4D volumes are the data needed to run probabilistic tractography.

3.3.2. Probabilistic tractography

Probabilistic tractography was performed with 'probtrackX' (FMRIB's Diffusion Toolbox - FDT v2.0) tool provided in FSL package (Behrens et al, 2007). The computation of the connection probability existing between a seed A and a target B given the data Y is:

$$\mathcal{P}\,(\exists\; \text{ROI A} \rightarrow \text{ROI B} \mid Y) \qquad\qquad \text{(Eq. 3.2)}$$

First of all a 'placeholder' is defined (i.e., *z*) to take into account the tracking progression. Placing *z* in A, a random sample (θ,Φ) is selected from

$$\mathcal{P}\,(\theta,\Phi \mid Y) \qquad\qquad \text{(Eq. 3.3)}$$

and z is moved for a distance s (i.e., step length) along (θ, Φ) direction. These steps have to be repeated until a stopping criterion is met. By drawing many of such streamlines, the spatial pdf of

$$\mathcal{P}\,(\exists\,\text{ROI A} \rightarrow \text{ROI B} \mid Y) \qquad\qquad \text{(Eq. 3.4)}$$

is built for all possible targets (Behrens et al., 2003). Then, imposing a specific target B, streamlines that do not connect A to B are excluded. The final tract is obtained by performing the summation of all the non-rejected streamlines, namely by counting in each voxel the number of non-excluded streamlines that run through it. A graphical representation of this procedure is illustrated in figure 3.7.

In this study, pairs of DMN, LLN and RLN clusters individuated as previously described in 3.2.2 were used as ROIs for running probabilistic tractography.

ProbtrackX was set to model 5000 samples within each voxel. Curvature threshold was set to 0.2, corresponding to a minimum angle of approximately ±80 degrees. The iterative algorithm step length was set to 0.5 mm and 2000 steps maximum were allowed, corresponding to a distance of 1 m (Behrens et al., 2007). Obtained tracks were registered at first to high-resolution structural brain images (gained as explained in paragraph 3.2.1. in 'Image co-registration' section), then to MNI152 standard space (2x2x2 mm^3 resolution).
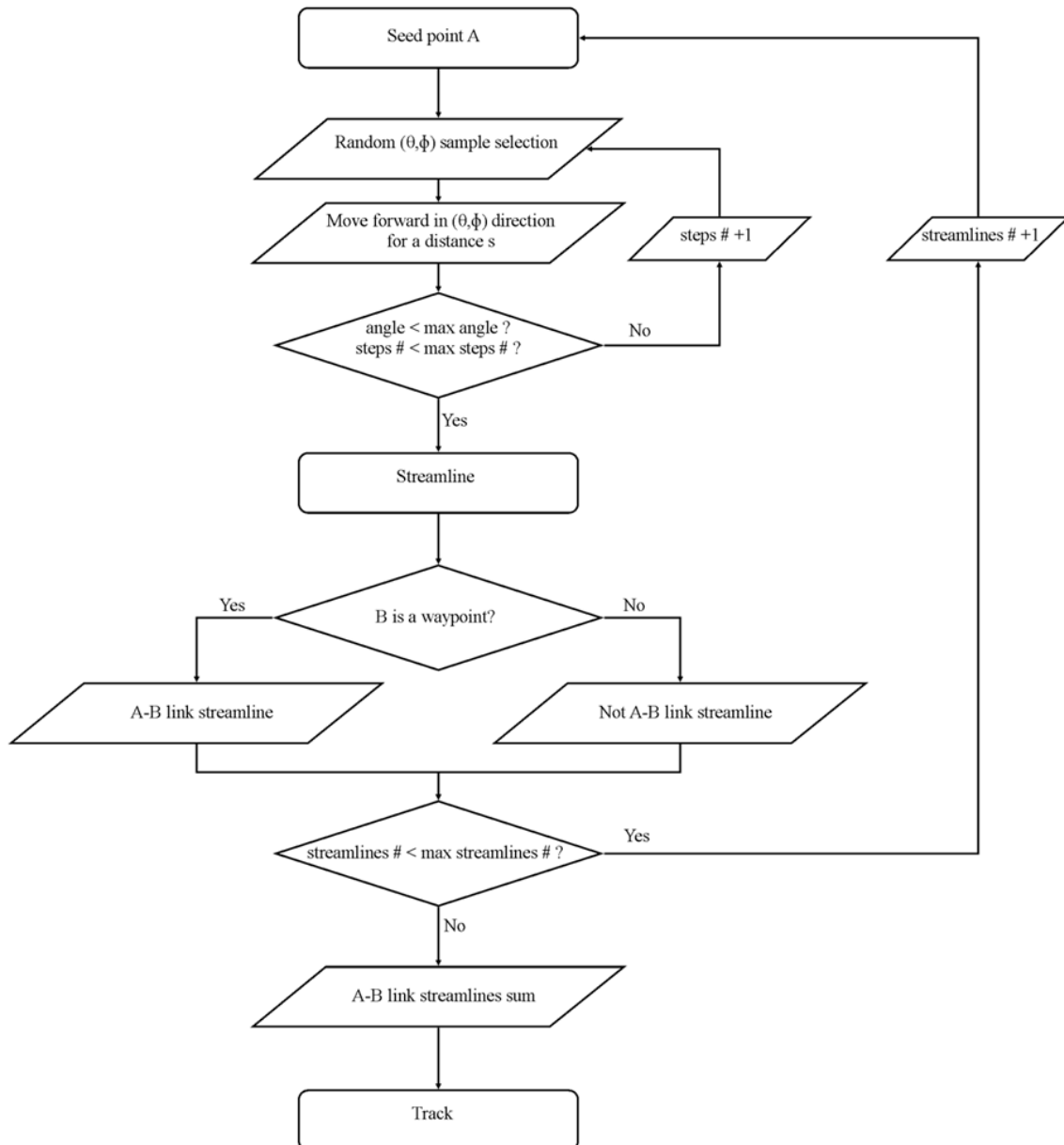
Figure 3.7 ProbtrackX processing scheme when point A is set as seed and B is set as target. All the streamlines running through A are found with a probabilistic approach. Then, among these, streamlines that do not run through B are rejected.
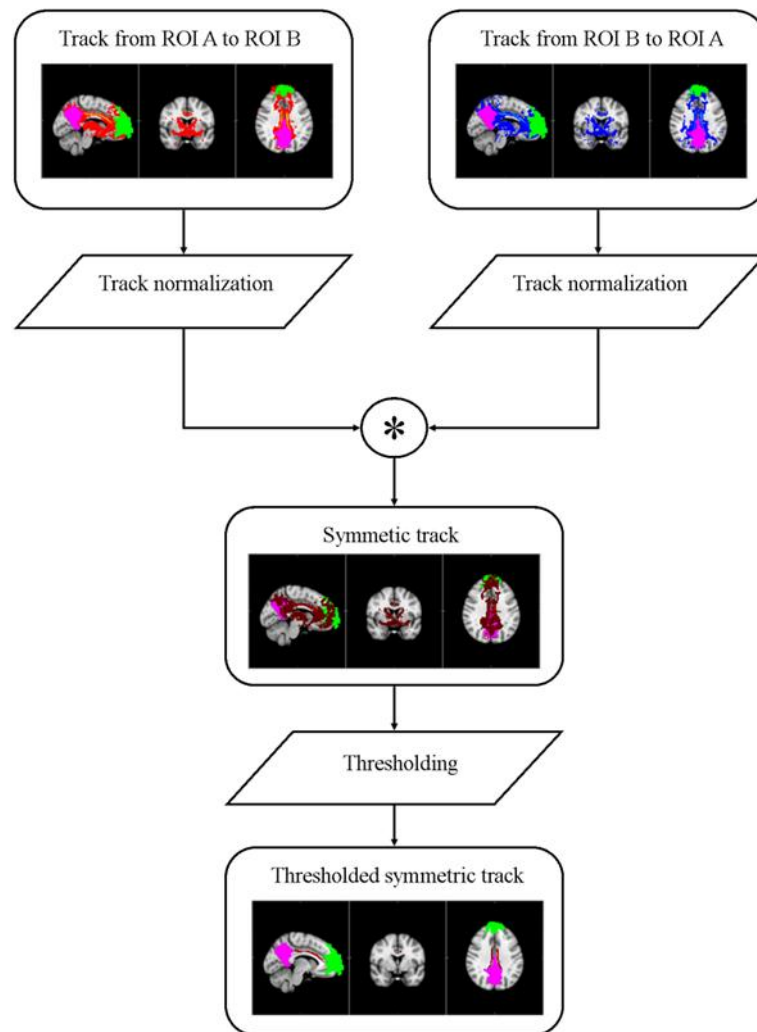
3.3.3 Tract processing

In this study, we aimed at probing the structural connections between pairs of clusters (i.e., ROIs) belonging to DMN, RLN and LLN with probabilistic tractography. Differently from the classical fMRI-guided tractography approach that uses deterministic algorithms, the

rsfMRI-guided tractography with probabilistic technique does not require a dilation of the ROIs in order to bridge the gap between GM and WM..

In probabilistic tractography, defining a cluster as seed region is not the same of setting it as target . Hence, a novel processing of the tract was implemented in order to solve this problem. Imposing A as seed and B as target, the reconstructed tract differs from the tract obtained setting B as seed and A as target, highlighting an asymmetry in defining seed and target regions. This happens due to the intrinsic nature of probabilistic tractography. As explained in figure 3.7, at first, all streamlines running through the seed are generated using a Bayesian approach, starting the tracking from the seed location. Then, the identified streamlines that do not run through the target are rejected. Hence, not surprisingly, tracts generated in the two opposite ways do not exactly correspond. For this reason, considering all the generic possible pairs of ROIs within each selected RSN, tracts were generated setting A as seed and B as target and *viceversa*. The steps accomplished to reconstruct the bundles and to overcome the tract symmetry limitation are hereunder described:

- tract from ROI A (seed) to ROI B (target) was normalized to its maximum intensity. This value represents the total number of tracked probabilistic streamlines. After normalization, voxels intensities represent the probability of being part of the tract that run from ROI A and passed through ROI B; similarly, tract from ROI B (seed) to ROI A (target) was normalized to the maximum intensity of the track;

- the normalized tract going from ROI A to ROI B was multiplied by the normalized tract running from ROI B to ROI A. The resulted tract (we will refer to it as "symmetric" track), has non-zero voxels only where both the original tracts were not null;

- the symmetric tract was thresholded to remove false positive streamlines. In this study, we adopted the 15% of the maximum intensity of the original tract according to Khalsa and collegues (2014). Since our final tract was the product of two distinct tracts we multiplied the threshold values (i.e., $0.15 \times 0.15 = 0.02$). *

A graphical representation of this procedure is shown in figure 3.8.

Figure 3.8 Tract processing scheme. Original tracks are normalized and multiplied in order to obtain a symmetric track. Then, the symmetric tract is thresholded.

Since there is no standard procedure described in the literature about thresholding, we could make two different methodological choices. The first one consisted in accomplishing the thresholding before the product of the tracts. The second one, instead, lied in multiplying the tracts and then thresholding the final result. Note that the latter approach is less restrictive than the former. Consider as example a voxel whose intensity is above threshold in the tract that runs from A to B and that is, instead, under threshold in the tract that runs from B to A. Using the first approach the voxel will be rejected since its intensity will be equal to zero. In this case the voxel will be hence classified as a false positive. On the other hand, if we adopt the second approach, the same voxel will not have necessarily an intensity value lower than the applied threshold and so, it will not necessarily be classified as false positive and then rejected.

All the obtained tracks for each subjects were visualized both in FSLview (http://fsl.fmrib.ox.ac.uk/fsl/fslview) and in Trackvis (http://trackvis.org) in order to identify the anatomical WM fibers to which the virtual tracks refer.

3.3.4. Structural connectivity

After tracts processing, we addressed the issue of defining a SC index. In this work we decided to use the number of voxels above threshold (0.02), since it is the most common SC index adopted in previous studies (Khalsa et al.,2014, Lilja et al., 2014). For each pair of ROIs, group SC was evaluated as the average on single-subject SC indexes. These values were stored in matrices called group SC matrices displayed as images in order to visually compare them with the FC matrices.

3.3.5. Group probabilistic map construction

In order to validate the SC results, we created group probabilistic maps of the "symmetric" tracts by averaging them across the subjects. The voxel values of each map state the number of subjects which presents the specific tract. The maps were thresholded at 20%, 40% and 60% to highlight the most robust results of the tract processing. Finally, we computed the mean intensities on each group probabilistic map and stored them in matrices called SC consistency matrices.

## 3.4. Functional connectivity and structural connectivity comparison

The index used to express functional connectivity was correlation (z-score) between cluster time series. On the other hand, structural connectivity was expressed by the number of voxels above a threshold fixed at 0.02.

Functional connectivity (FC) and structural connectivity (SC) comparison was performed at two different levels (figure 3.9):

- considering each couple of clusters, across subjects;
- considering each subject, across connections.

The first comparative approach consisted in averaging functional and structural connectivity indexes across subjects. Then, correlation between mean FC and mean SC was evaluated.

The second approach consisted in estimating the correlation between single subject FC and SC indexes for each subject .
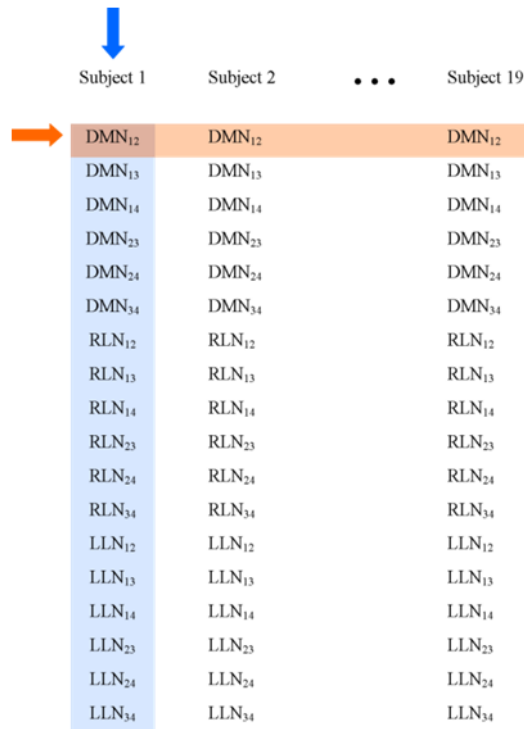
Figure 3.9 Comparative approaches scheme: across subjects (orange) and across connections (blue). The former approach implies to consider the same pair of cluster among all the subjects belonging to the sample. The latter approach implies to consider all the couple of sub-network in a single subject.

Chapter 4

Results

In this chapter we report at first the characteristics of the sample recruited for this study (par. 4.1).

Resting state fMRI (rsfMRI) analysis results are then presented, starting from the group independent component analysis (ICA) and resting state network (RSN) clustering procedure outcome (par. 4.2.1). Next, the functional connectivity (FC) issue is addressed (par. 4.2.2).

In parallel, diffusion weighted imaging (DWI) analysis results are illustrated, leading off with probabilistic tractography (par 4.3.1). Then structural connectivity (SC) investigation results are reported, followed by (par. 4.3.2) the outcomes of the consistency study accomplished through the tract group probabilistic maps (par. 4.3.3).

Afterwards, FC and SC comparison results are shown (par. 4.4).

4.1. Subjects and data acquisition

Twenty healthy right-handed voluntary subjects (mean age = 45.70 ± 11.53 years, 9 males) were recruited for this study. However, only nineteen subjects (mean age = 45.53 ± 11.82 years, 9 males) were considered in this work analysis since one subject was excluded due to the low quality of its DWI images.

# 4.2. rsfMRI: image processing and functional connectivity results

4.2.1. rsfMRI data processing results

Setting group-ICA dimensionality at 30, we identified the components (ICs) and, among them, we discriminated nineteen "good" ICs from noise. Then, for our connectivity study, we selected IC1, IC5 and IC9, corresponding respectively to Default Mode resting state Network (DMN), Right Lateral resting state Network (RLN) and Left Lateral resting state Network (LLN) (red boxes in fig. 4.1).
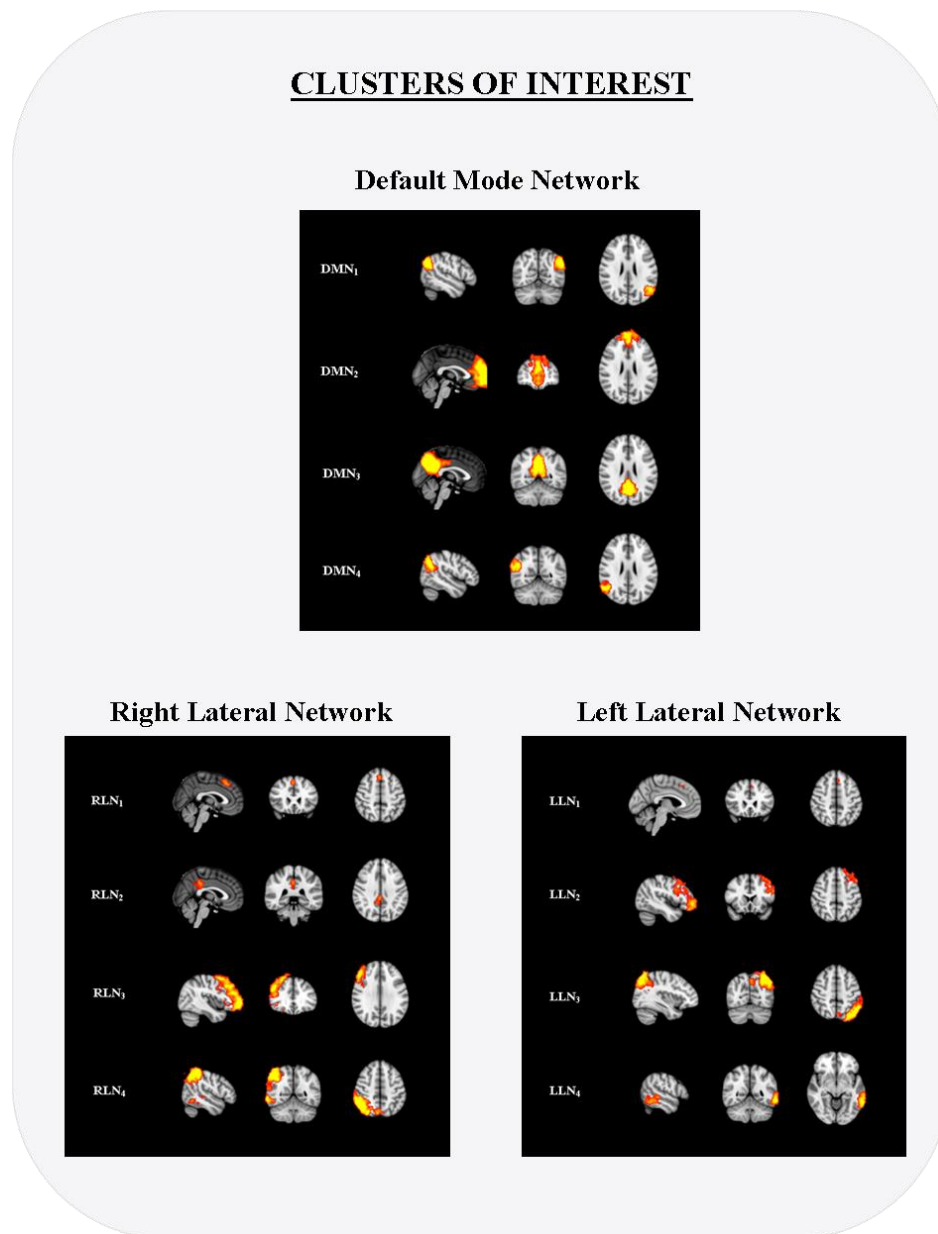
The clusters obtained from DMN, RLN and LLN splitting are displayed in figure 4.2, while their anatomical features are reported in table 4.1. Note that even if RLN and LLN are symmetric networks, the identified clusters are not the same. In RLN the right cingulated gyrus was classified as a single cluster, while in the other hemisphere the same region was classified in LLN_1 together with right parietal cortex. Furthermore, the temporal lobe, which was recognized as a single sub-network in LLN, was anatomically connected with parietal cortex activated area in RLN.

The identified sub-networks were used as ROIs for both the following FC and SC analysis. Specifically, they were considered as group template for the extraction of the single subject time courses (i.e., the first step of the dual regression process), which are the input data for the FC analysis described in the next paragraph. The same ROIs were also used as seed/target regions for probabilistic tractography and SC analysis, as described later.
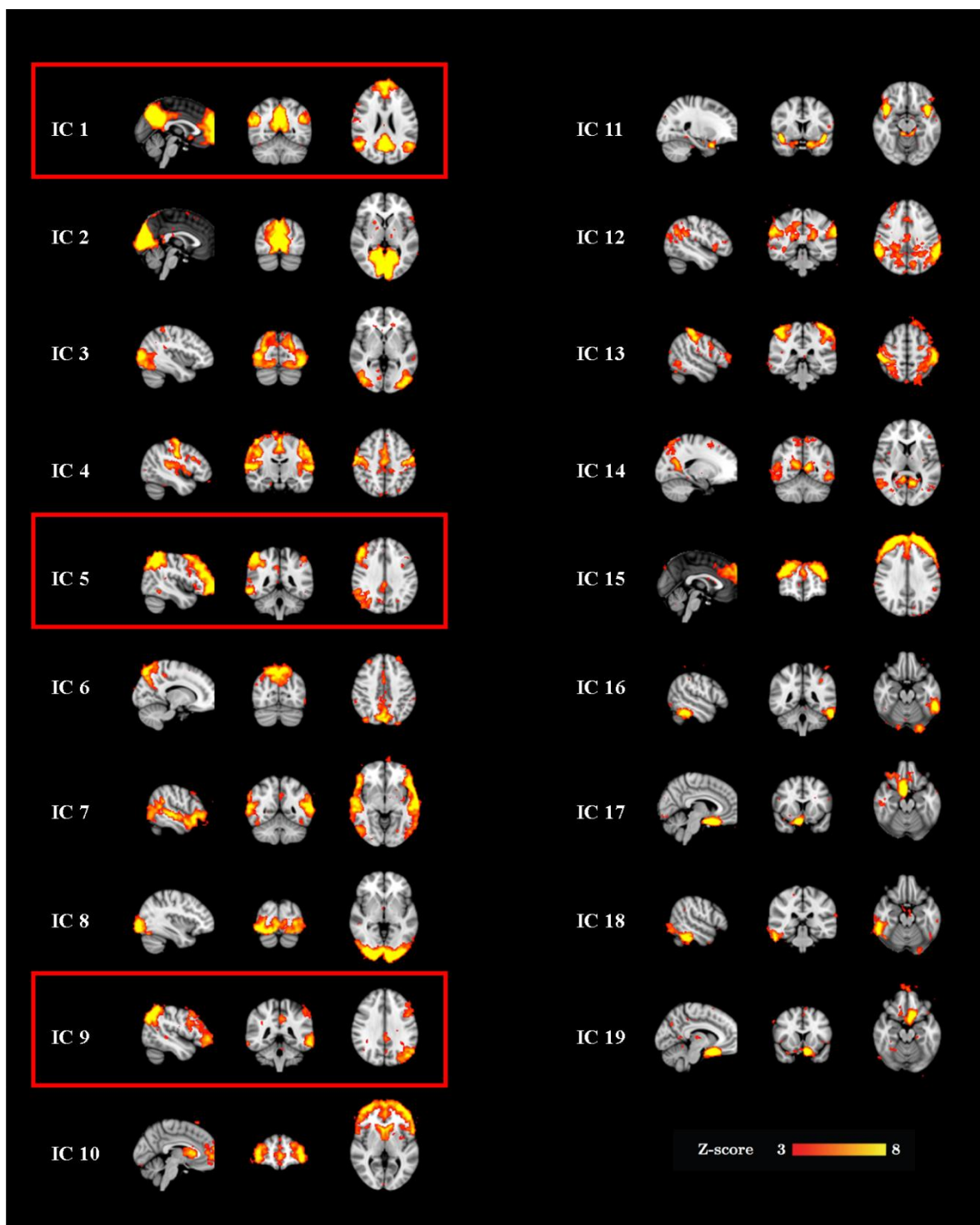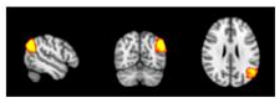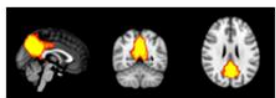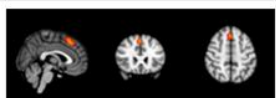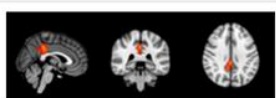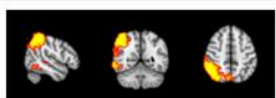
Figure 4.1 "Good" group-ICA components. The RSNs of interest are highlighted in red boxes. IC1 corresponds to Default Mode Network, IC5 to Right Lateral Network and IC9 to Left Lateral Network. IC = Independent component.

CLUSTERS OF INTEREST

Default Mode Network

Right Lateral Network   **Left Lateral Network**

Figure 4.2 Clusters obtained from DMN, RLN and LLN. DMN = Default Mode Network ; RLN = Right Lateral Network; LLN = Left Lateral Network.

Cluster		Brain region	Size [number of voxel]	Peak intensity [z-score]	Peak MNI coordinates (x, y, z) [voxel]
DMN$_1$		Left lateral parietal cortex	2423	12.8	(68, 28, 55)
DMN$_2$		Medial prefrontal cortex	10929	18.1	(45, 95, 34)
DMN$_3$		Posterior cingulate cortex	6594	21	(44, 31, 55)
DMN$_4$		Right lateral parietal cortex	2195	13.3	(21, 32, 54)
RLN$_1$		Right superior frontal gyrus	289	7.19	(43, 77, 59)
RLN$_2$		Right cingulate gyrus	473	5.63	(44, 44, 56)
RLN$_3$		Right frontal cortex	10092	11.4	(22, 89, 33)
RLN$_4$		Right parietal cortex and temporal cortex	9195	18.3	(23, 36, 66)
LLN$_1$		Left superior frontal gyrus	28	4.13	(47, 76, 60)
LLN$_2$		Left frontal cortex	4685	8.21	(67, 87, 34)
LLN$_3$		Left parietal cortex and cingulate gyrus	6236	13.2	(63, 26, 13)
LLN$_4$		Left temporal cortex	2083	9.74	(76, 37, 33)

Table 4.1 Clusters features referred to MNI standard space (resolution = 2x2x2 mm^3). DMN = Default Mode Network; RLN = Right Lateral Network; LLN = Left Lateral Network.

4.2.2. Functional connectivity analyses results

FC analyses were performed within DMN, RLN and LLN, considering each possible pairs of clusters (i.e., 18, 6 for each RSN of interest).

For each subject, functional connectivity was calculated as full correlation (Pearson correlation coefficient) between the time series associated to the considered sub-networks. Then, the correlation values were transformed in z-score and stored in matrices which were represented as images in order to visually highlight the highest correlation values. Values on the diagonal of the matrices were forced to zero. An example of these subject-specific FC matrices, expressed as Pearson correlation coefficient, is shown below (Fig. 4.3).
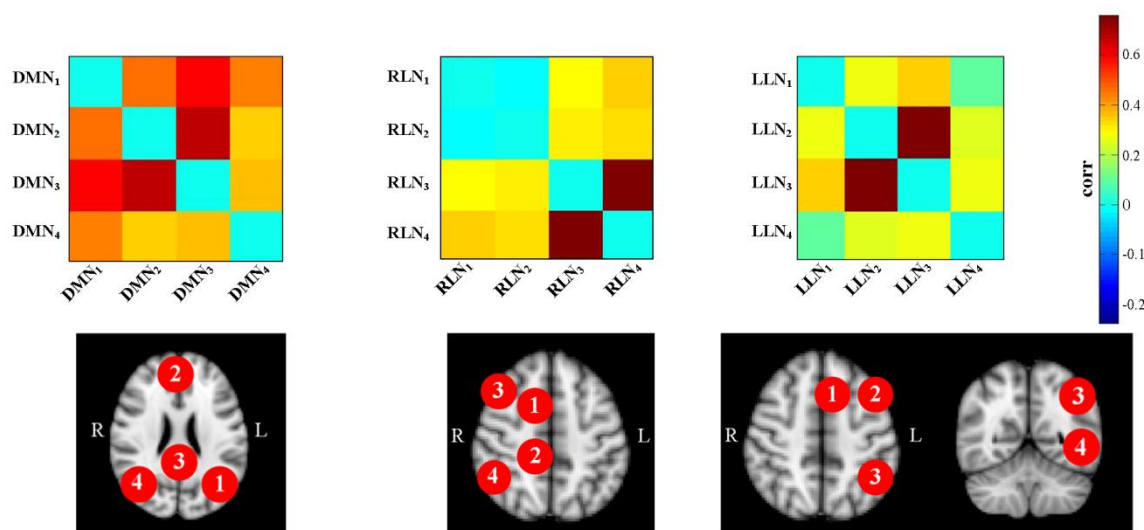
Figure 4.3 Subject-specific functional connectivity matrices expressed as Pearson correlation coefficient. In the first line, matrices referring to a single-subject data are shown. Different colors represent different Pearson correlation coefficient values. Color scale is reported on the right. In the second line, a schematic representation of the RSNs associated to the matrices is illustrated: from left to right, DMN, RLN and LLN axial views and LLN coronal view are shown. Red numbered spots represent the identified clusters considered in the matrices above. DMN = Default Mode Network; RLN = Right Lateral Network; LLN = Left Lateral Network; R = Right; L = Left.

The group FC matrices computed by the average of the single subject Pearson correlation coefficients are shown in figure 4.4. In this paragraph, functional connectivity matrices are reported with their values expressed as Pearson correlation coefficient since correlation allows a more intuitive interpretation compared to z scores, conversely addressed in our statistics.
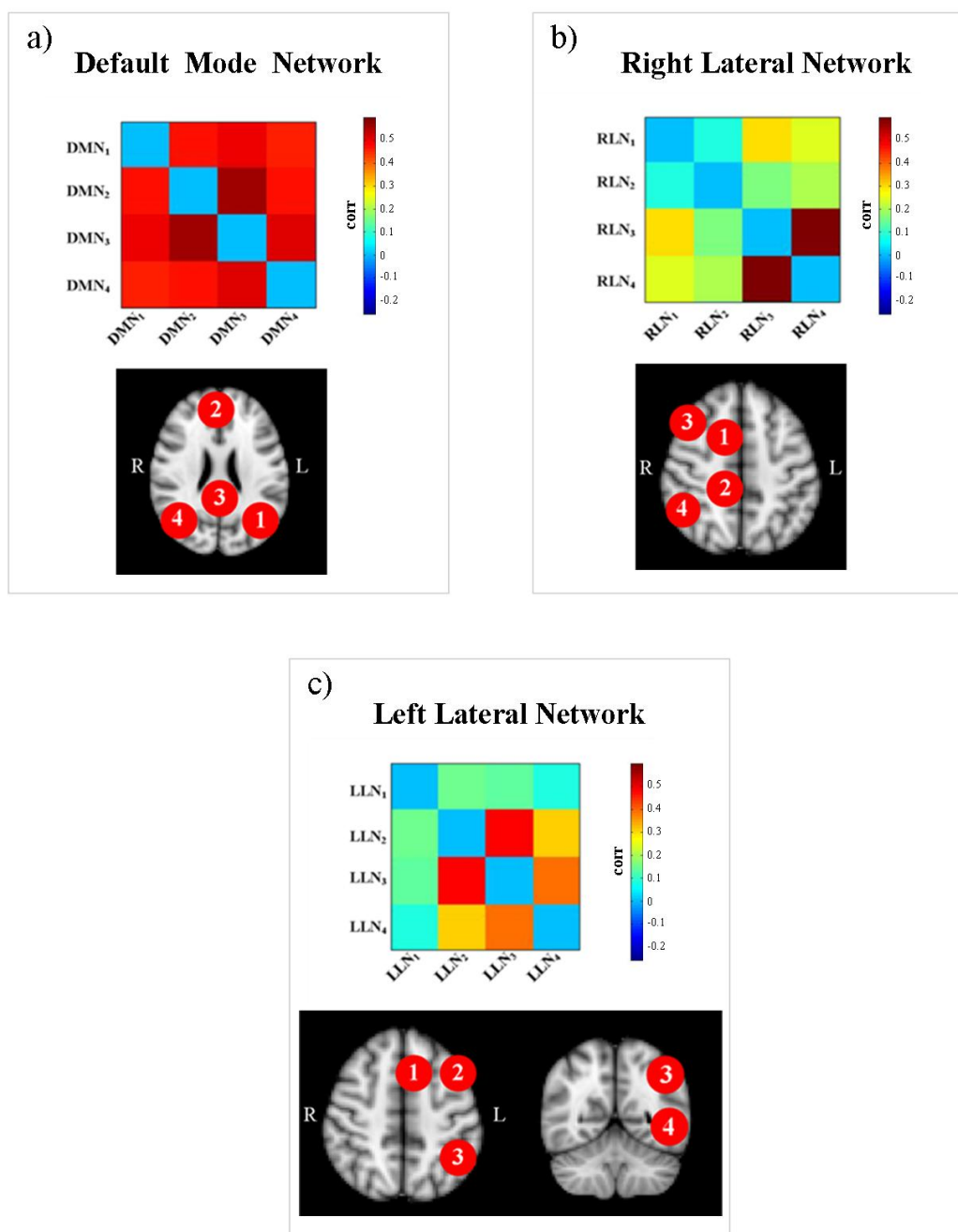
Figure 4.4 Group functional connectivity matrices expresses as full correlation (Pearson correlation coefficient). Panel (a) refers to DMN, panel (b) refers to RLN and panel (c) refers to LLN. In each panel, on top, it is shown the group FC matrix associated to the underlying RSN. Color scale is reported on the right. Red numbered spots represent the identified clusters considered in the matrices. DMN = Default Mode Network; RLN = Right Lateral Network; LLN = Left Lateral Network; R = Right; L = Left.

Each pair of clusters obtained from DMN showed high functional correlations (values between 0.460 and 0.564). In this network the FC maximum value was observed between DMN_2 (corresponding to medial prefrontal cortex) and DMN_3 (corresponding to posterior cingulate cortex).

Within the RLN the highest FC index was registered between RLN_3 (corresponding to right frontal cortex) and RLN_4 (corresponding to right parietal cortex). The other RLN pairs of clusters showed functional connectivity values significantly lower (p-value=0.009) than the maximum value registered in this network.
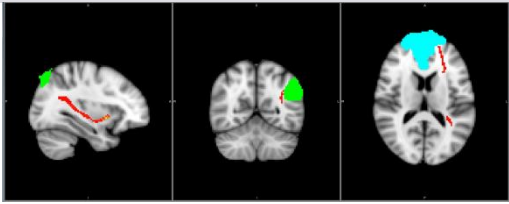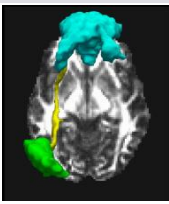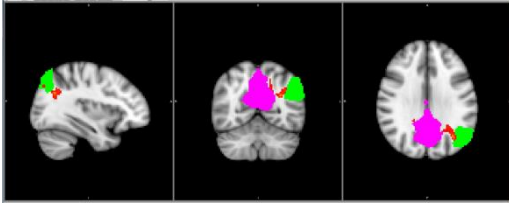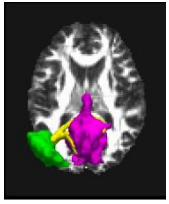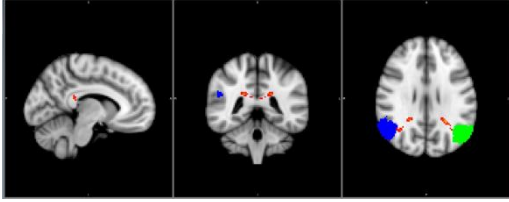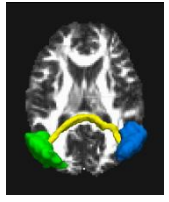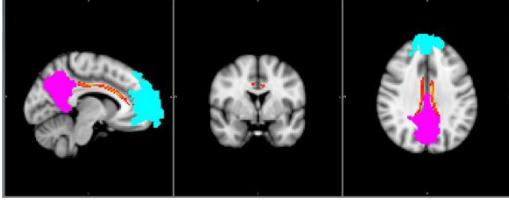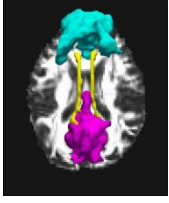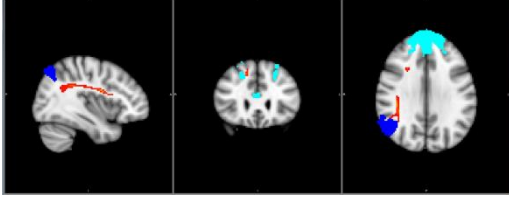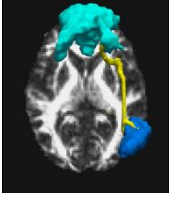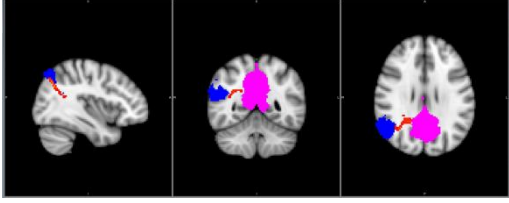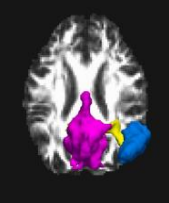
Within LLN the maximum correlation value was obtained between LLN_2 (corresponding to left frontal cortex) and LLN_3 (corresponding to left parietal cortex). Also LLN_3 and LLN_4 (corresponding to left temporal cortex) and LLN_2 and LLN_4 presented significant FC values.

4.3. DWI: image processing and structural connectivity results

4.3.1. Probabilistic tractography and tract processing results

SC analysis was performed by means of probabilistic tractography. The clusters pairs identified in DMN, RLN and LLN were used as ROIs (seed and target, symmetrically combined) to extract the WM fiber bundles which linked each pair.

Processed tracts were visualized both in FSLview (http://fsl.fmrib.ox.ac.uk/fsl/fslview) and Trackvis (http://trackvis.org) in order to be anatomically located. Since the tracts were reconstructed with a probabilistic approach, some of them could not be associated to just one well-recognizable anatomical fasciculus but, instead, to an ensemble of bundles, as shown in tables 4.2 (DMN), 4.3 (RLN), 4.4 (LLN) for a single subject case. However, the reported results are valid for all the subjects included in this study.
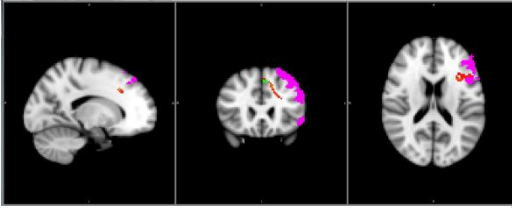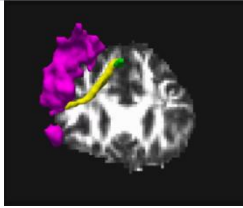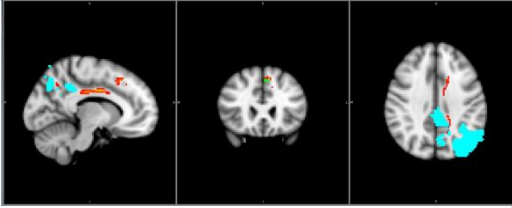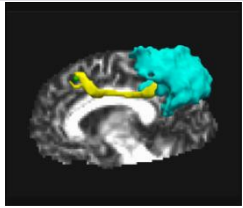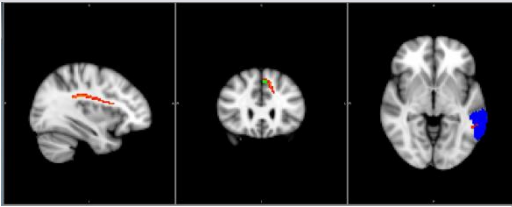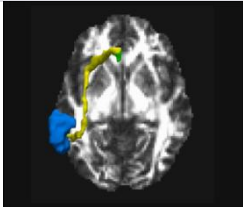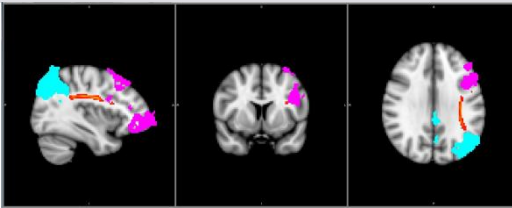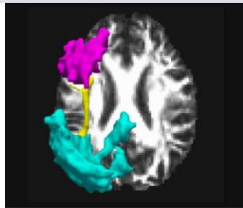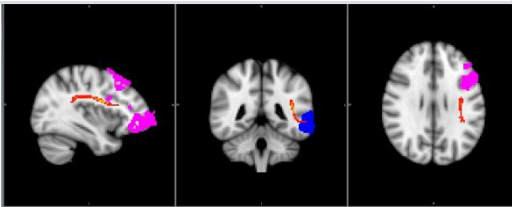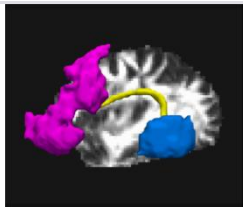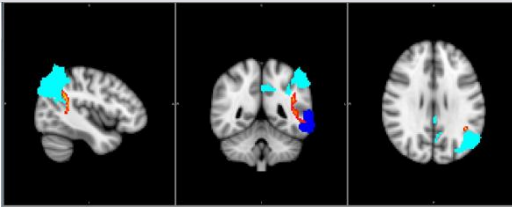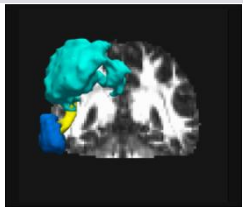
Seed ↔ Target	Track visualization in FSLview	Track visualization in Trackvis	Anatomical fasciculus
DMN$_1$ ↔ DMN$_2$			Left SLF, left IFOF left ILF
DMN$_1$ ↔ DMN$_3$			Left SLF, left ILF, splenium CC
DMN$_1$ ↔ DMN$_4$			CC splenium
DMN$_2$ ↔ DMN$_3$			Cingoli
DMN$_2$ ↔ DMN$_4$			Right SLF, right IFOF right ILF
DMN$_3$ ↔ DMN$_4$			Right SLF, right ILF, splenium CC

Table 4.2 Processed tracts (i.e., "symmetric" tracts thresholded at 0.02) obtained between DMN clusters in a single subject. DMN = Default Mode Network; SLF = superior longitudinal fasciculus; ILF = inferior longitudinal fasciculus; IFOF = inferior frontal-occipital fasciculus; ILF = inferior longitudinal fasciculus; CC = corpus callosum.

71

Seed ↔ Target	Track visualization in FSLview	Track visualization in Trackvis	Anatomical fasciculus
RLN₁ ↔ RLN₂			Right cingolum
RLN₁ ↔ RLN₃			CC genu, right ATR
RLN₁ ↔ RLN₄			Right cingolum, CC
RLN₂ ↔ RLN₃			Right IFOF, right ATR, right uncinate, right cingolum
RLN₂ ↔ RLN₄			CC splemnium
RLN₃ ↔ RLN₄			Right SLF

Table 4.3 Processed tracts (i.e., "symmetric" tracts thresholded at 0.02) obtained between RLN clusters in a single subject. RLN = Right Lateral Network; CC = corpus callosum; ATR = anterior thalamic radiation; IFOF = Inferior frontal occipital fasciculus; SLF = superior longitudinal fasciculus.

Seed ↔ Target	Track visualization in FSLview	Track visualization in Trackvis	Anatomical fasciculus
LLN₁ ↔ LLN₂			CC genu, left ATR, left ACR
LLN₁ ↔ LLN₃			Left cingolum, CC
LLN₁ ↔ LLN₄			Left SLF, CC genu, left ACR, left ATR
LLN₂ ↔ LLN₃			Left SLF
LLN₂ ↔ LLN₄			Left SLF, left ILF, left IFOF
LLN₃ ↔ LLN₄			Left SLF

Table 4.4 Processed tracts (i.e., "symmetric" tracts thresholded at 0.02) obtained between LLN clusters in a single subject. LLN = Left Lateral Network; CC = corpus callosum; ATR = anterior thalamic radiation; ACR = Anterior Corona Radiata; IFOF = Inferior frontal occipital fasciculus; ILF = Inferior lateral fasciculus; SLF = superior longitudinal fasciculus.

4.3.2. Structural connectivity analysis results

For each subject, SC was evaluated using as index the number of voxel above threshold (0.02) belonging to each reconstructed tract within the same RSN. Averaging the SC indexes across subjects, conversely to FC analysis, group SC was obtained and group SC matrices where created in order to visually highlight the most relevant results (Fig. 4.5).

Within all the considered RSNs, structural connections were found and the connection degree was variable across the couples of clusters.

In DMN, the strongest link was found between DMN_1 (corresponding to left lateral parietal cortex) and DMN_2 (corresponding to medial prefrontal cortex).

In RLN, high structural indexes were observed between RLN_3 (corresponding to right frontal cortex) and RLN_4 (corresponding to right parietal cortex) and between RLN_2 (corresponding to right cingulated gyrus) and RLN_3. The link found between RLN_3 and RLN_4 was the strongest observed among the three considered RSNs.

In LLN, the highest structural connectivity index was observed between LLN_2 (corresponding to left frontal cortex) and LLN_3 (corresponding to left parietal cortex).
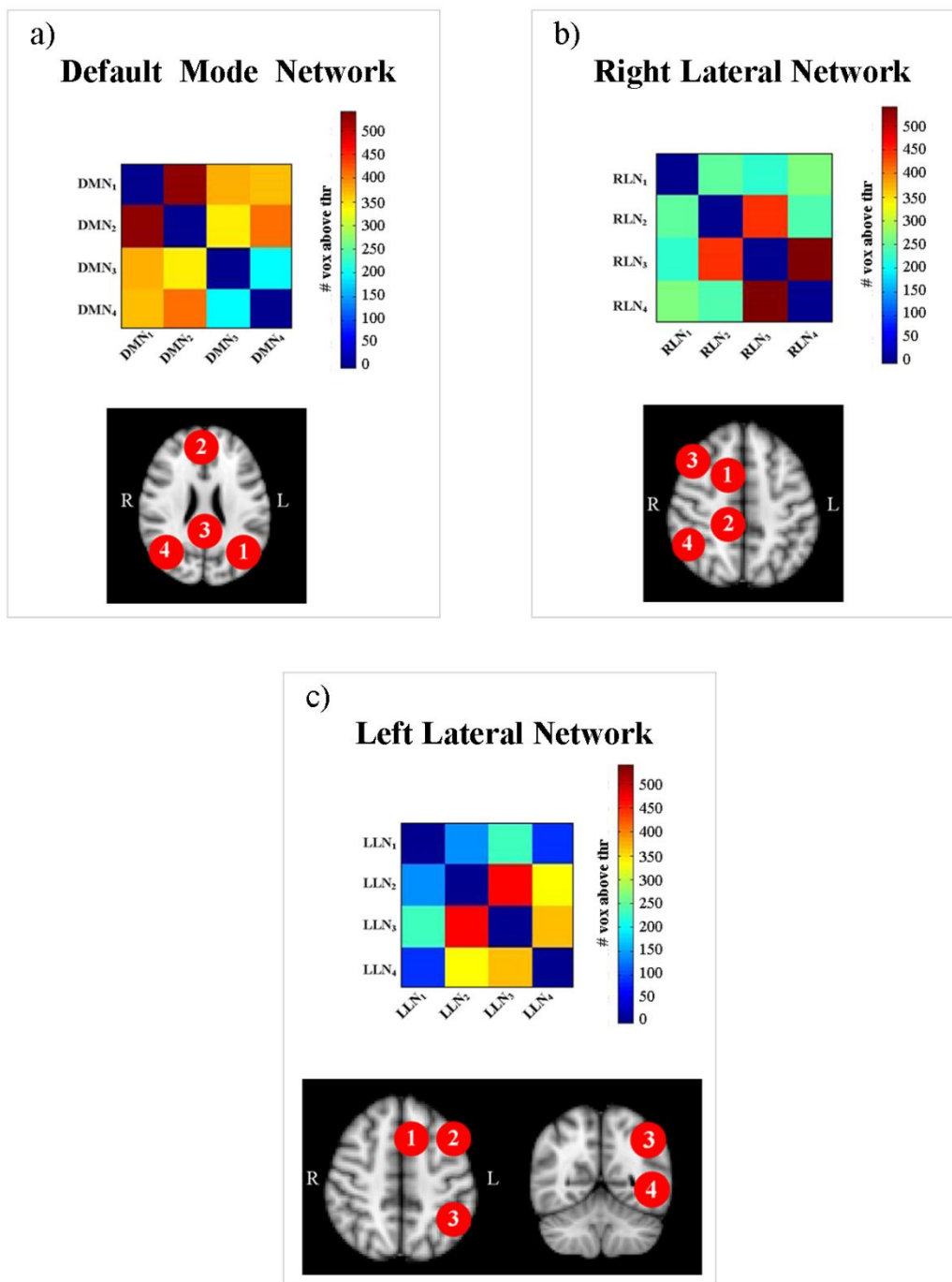
Figure 4.5 Group SC matrices expresses as number of voxel above threshold (0.02). Panel (a) refers to DMN, panel (b) refers to RLN and panel (c) refers to LLN. In each panel, on top, it is shown the group SC matrix associated to the underlying RSN. Color scale is reported on the right. Red numbered spots represent the identified clusters considered in the matrices. DMN = Default Mode Network; RLN = Right Lateral Network; LLN = Left Lateral Network; R = Right; L = Left.

4.3.3. Group probabilistic map results

Group probabilistic maps were thresholded at 20%, 40% and 60%. Those obtained thresholding at 20% were the less restrictive. Tracts belonging to these maps were easily detectable. The higher thresholds, 60% in particular, made tracts thinner, sometimes even null. An example of differences existing between different maps of the same tract is shown in figure 4.6.
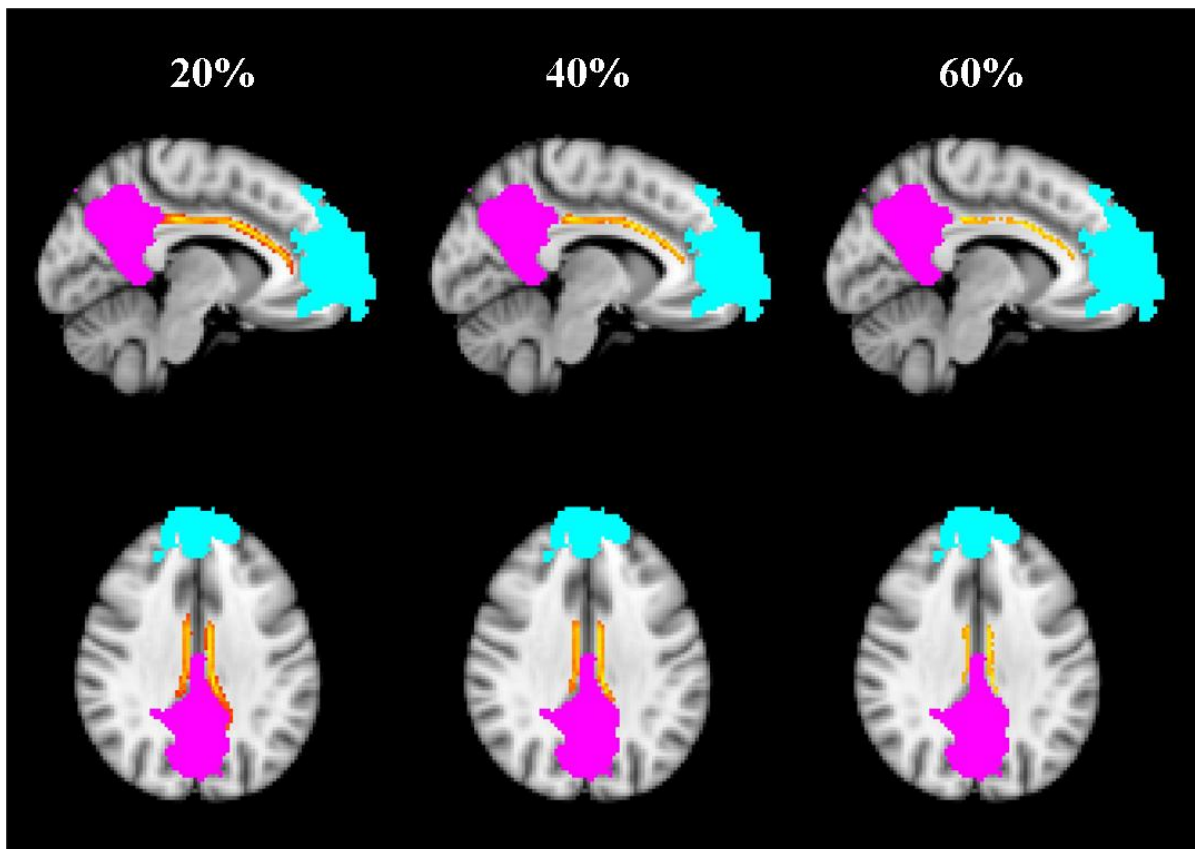
Figure 4.6 Sagittal and axial view (respectively first and second line) of the tract connecting DMN_2 and DMN_3 thresholded at 20%, 40% and 60%.

The mean intensity of the group probabilistic maps was used as cluster to cluster SC consistency index and stored in group SC matrices (Fig. 4.7). For every pairs of ROIs, this index represents how many subjects present the tract in each specific voxel. Therefore, it is an index of tract robustness across subjects.
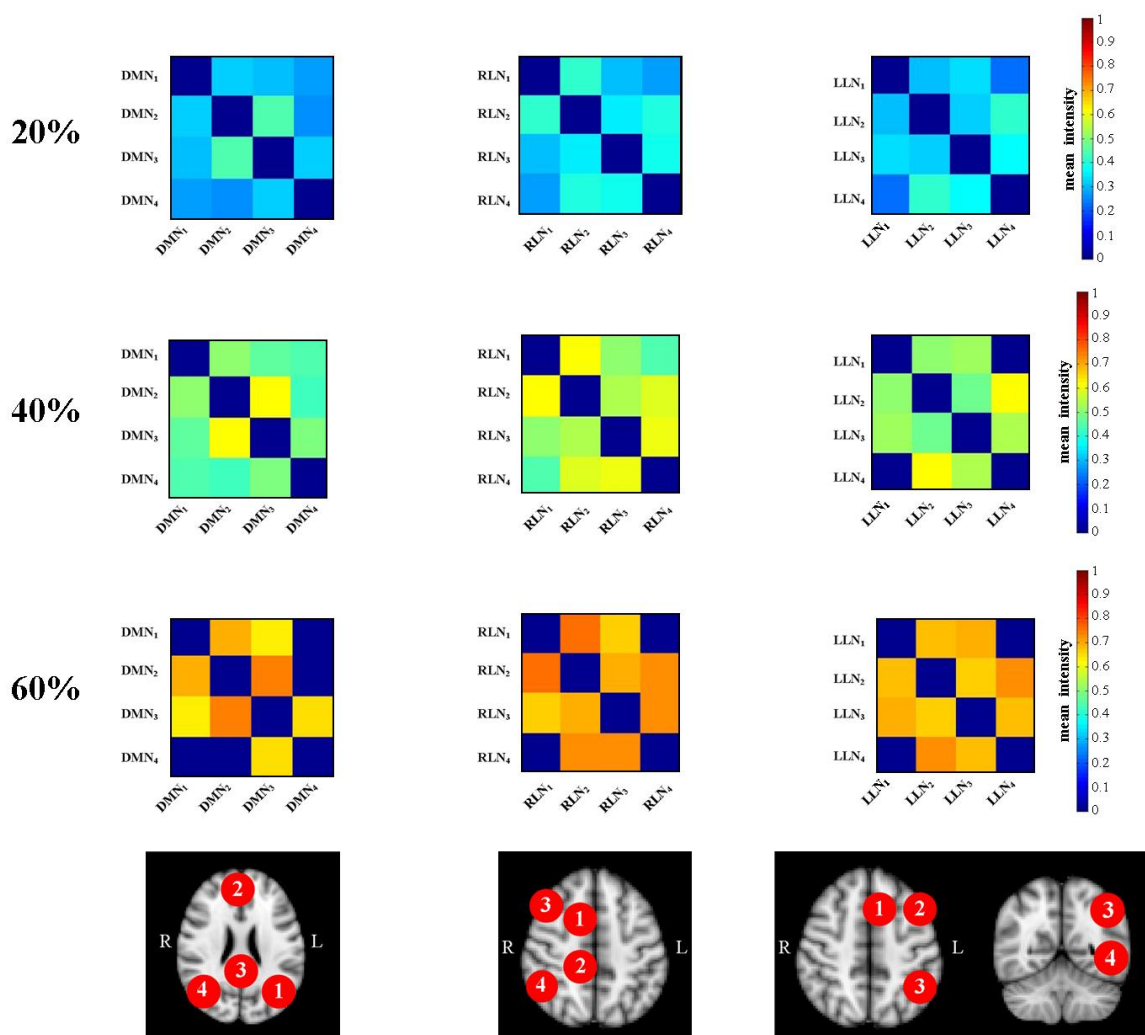
Figure 4.7 SC consistency group matrices calculated from group probabilistic maps thresholded at 20%, 40% and 60% and their respective clusters (from top to bottom). Color scale is reported on the right. Red numbered spots represent the identified clusters considered in the matrices. DMN = Default Mode Network; RLN = Right Lateral Network; LLN = Left Lateral Network; R = Right; L = Left.

Matrices associated to group probabilistic maps thresholded to 20% show not null structural connectivity indexes between all the couples of sub-networks. However, with higher threshold, some links between ROIs are lost. In group probabilistic maps thresholded at 40%, SC between LLN$_1$ (corresponding to left superior frontal gyrus) and LLN$_4$ (corresponding to left temporal cortex) is not detected. In group probabilistic maps thresholded at 60%, also DMN1 (corresponding to left lateral parietal cortex) and DMN4 (corresponding to right lateral parietal cortex), DMN2 (corresponding to medial prefrontal cortex) and DMN4, RLN1 (corresponding to right superior frontal gyrus) and RLN4

(corresponding to right parietal and temporal cortex) are not indicated as linked, highlighting a great inter-subject variability. The sub-networks that did not lost their connections in the maps thresholded at 60% are very robust and characterized by a low inter-subject variability.
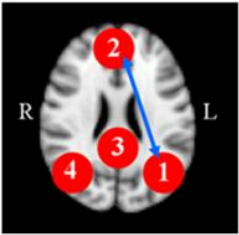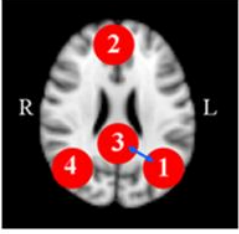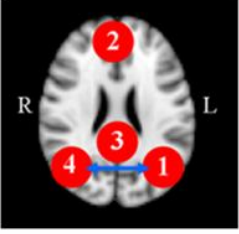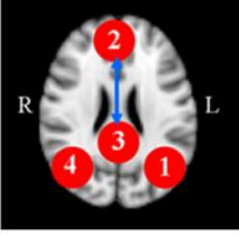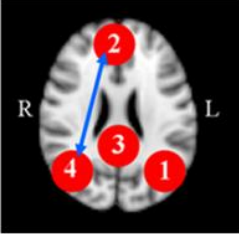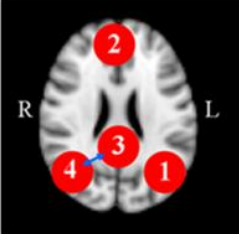
4.4. Functional connectivity and structural connectivity comparison results

Functional and structural connectivity comparison was performed by computing the correlation between the z-score as FC index and the number of voxels above threshold (0.02) as SC one. The comparison was performed both across subjects and across the pairs of clusters (Figure 3.9).
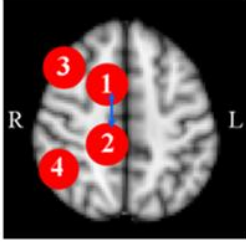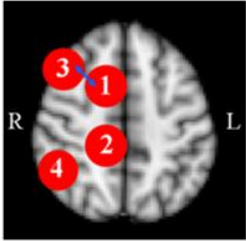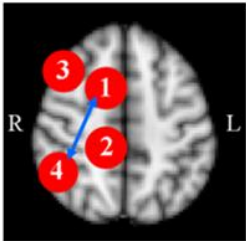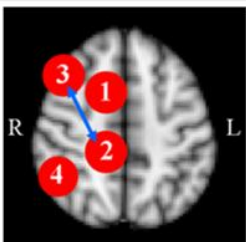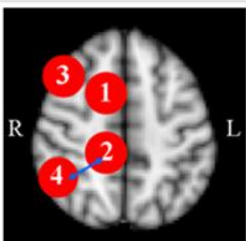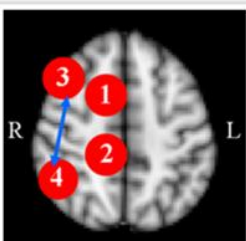
4.4.1 Across subject comparison

The first approach consisted in analyzing the relationship between FC and SC across subjects. Functional and structural indexes values (mean ± standard deviation) are reported in tables 4.5 (DMN), 4.6 (RLN), 4.7 (LLN) and illustrated in figure 4.8 (matrices represented as images) and 4.9 (box and whiskers plots).

The strongest across subject correlations between FC and SC can be observed within LLN: high values of SC correspond to high values of FC. Moreover, within this network a similar trend is observed in FC and SC index values across the pairs of clusters (see the red line in figure 4.9, third line). Also RLN shows a good correlation level between FC and SC, even if less strong than the one in LLN. Within RLN, both the highest value of FC and SC index are found between RLN_3 (corresponding to right frontal cortex) and RLN_4 (corresponding to right parietal and temporal cortex). DMN, instead, does not show an evident correlation between FC and SC. Correlation (Pearson correlation coefficient) between FC and SC index series within each RSN of interest are reported in figure 4.10.
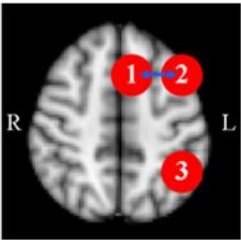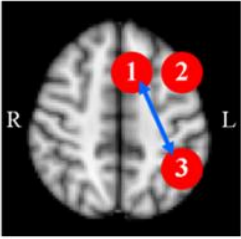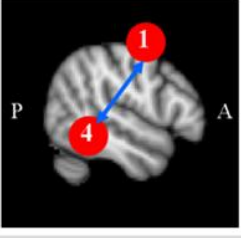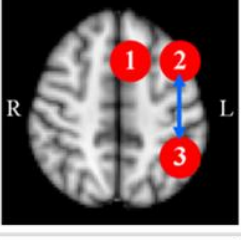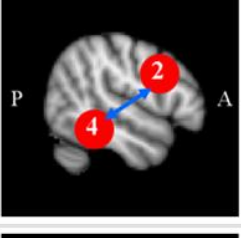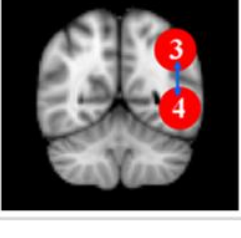
Seed - Target		FC [z-score]	SC [# voxels above thr]
	$DMN_1 \leftrightarrow DMN_2$	6.593 ± 3.123	530 ± 175
	$DMN_1 \leftrightarrow DMN_3$	7.171 ± 2.999	374 ± 148
	$DMN_1 \leftrightarrow DMN_4$	6.275 ± 2.049	370 ± 205
	$DMN_2 \leftrightarrow DMN_3$	8.262 ± 2.970	340 ± 66
	$DMN_2 \leftrightarrow DMN_4$	6.558 ± 2.498	412 ± 153
	$DMN_3 \leftrightarrow DMN_4$	7.268 ± 2.369	200 ± 89

Table 4.5 FC and SC across subjects comparison within DMN. FC is expressed as z-score (mean ± standard deviation), while SC is expressed as number of voxel above threshold (0.02) (mean ± standard deviation)

Seed - Target		FC [z-score]	SC [# voxels above thr]
	$RLN_1 \leftrightarrow RLN_2$	1.053 ± 1.057	246 ± 48
	$RLN_1 \leftrightarrow RLN_3$	3.799 ± 1.959	227 ± 107
	$RLN_1 \leftrightarrow RLN_4$	3.054 ± 1.591	265 ± 129
	$RLN_2 \leftrightarrow RLN_3$	2.111 ± 1.325	444 ± 170
	$RLN_2 \leftrightarrow RLN_4$	2.502 ± 1.577	541 ± 224
	$RLN_3 \leftrightarrow RLN_4$	8.818 ± 2.631	241 ± 99

Table 4.6 FC and SC across subjects comparison within RLN. FC is expressed as z-score (mean ± standard deviation), while SC is expressed as number of voxel above threshold (0.02) (mean ± standard deviation).

Seed - Target	FC [z-score]	SC [# voxels above thr]
$LLN_1 \leftrightarrow LLN_2$	1.928 ± 1.886	139 ± 55
$LLN_1 \leftrightarrow LLN_3$	1.799 ± 1.538	231 ± 58
$LLN_1 \leftrightarrow LLN_4$	1.098 ± 1.258	91 ± 102
$LLN_2 \leftrightarrow LLN_3$	6.846 ± 2.729	470 ± 258
$LLN_2 \leftrightarrow LLN_4$	4.182 ± 2.573	338 ± 89
$LLN_3 \leftrightarrow LLN_4$	5.286 ± 2.204	366 ± 114

Table 4.7 FC and SC across subjects comparison within LLN. FC is expressed as z-score (mean ± standard deviation), while SC is expressed as number of voxel above threshold (0.02) (mean ± standard deviation).
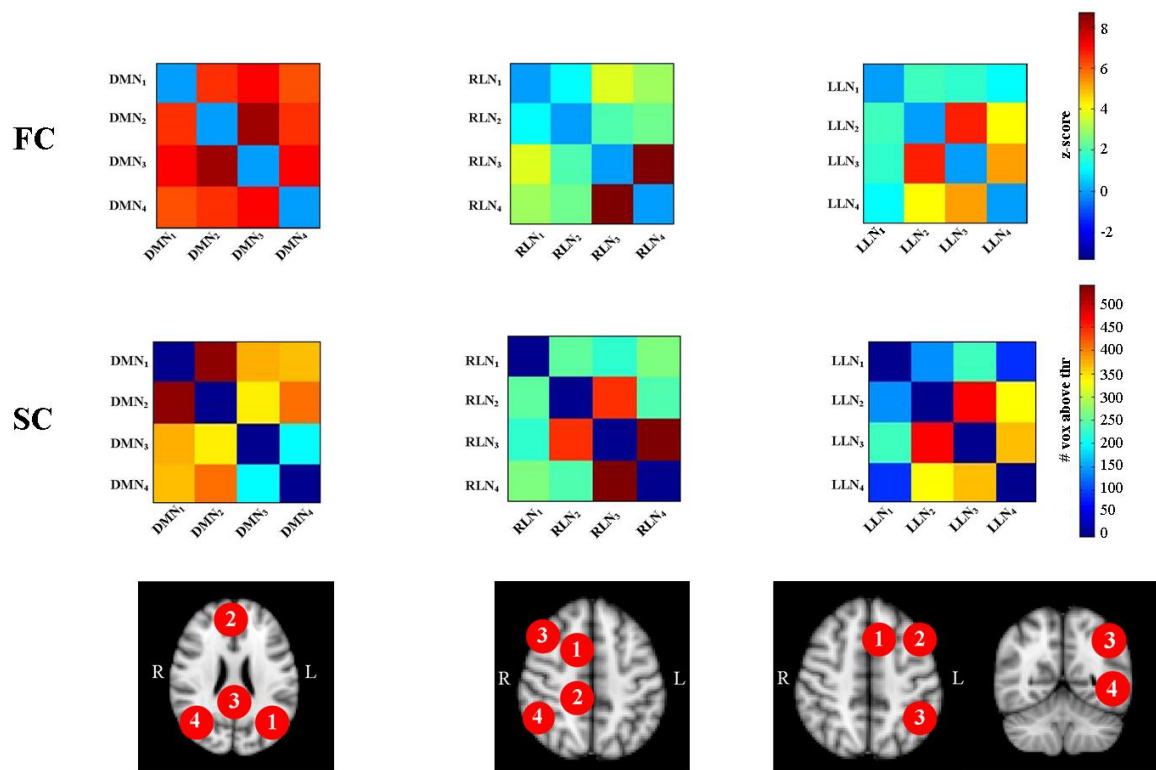
Figure 4.8 DMN, RLN, LLN functional and structural connectivity group matrices comparison. FC is expresses as z-score while SC is expressed as number of voxels above threshold (0.02). Color scale is reported on the right. Red numbered spots represent the identified clusters considered in the matrices. DMN = Default Mode Network; RLN = Right Lateral Network; LLN = Left Lateral Network; R = Right; L = Left.
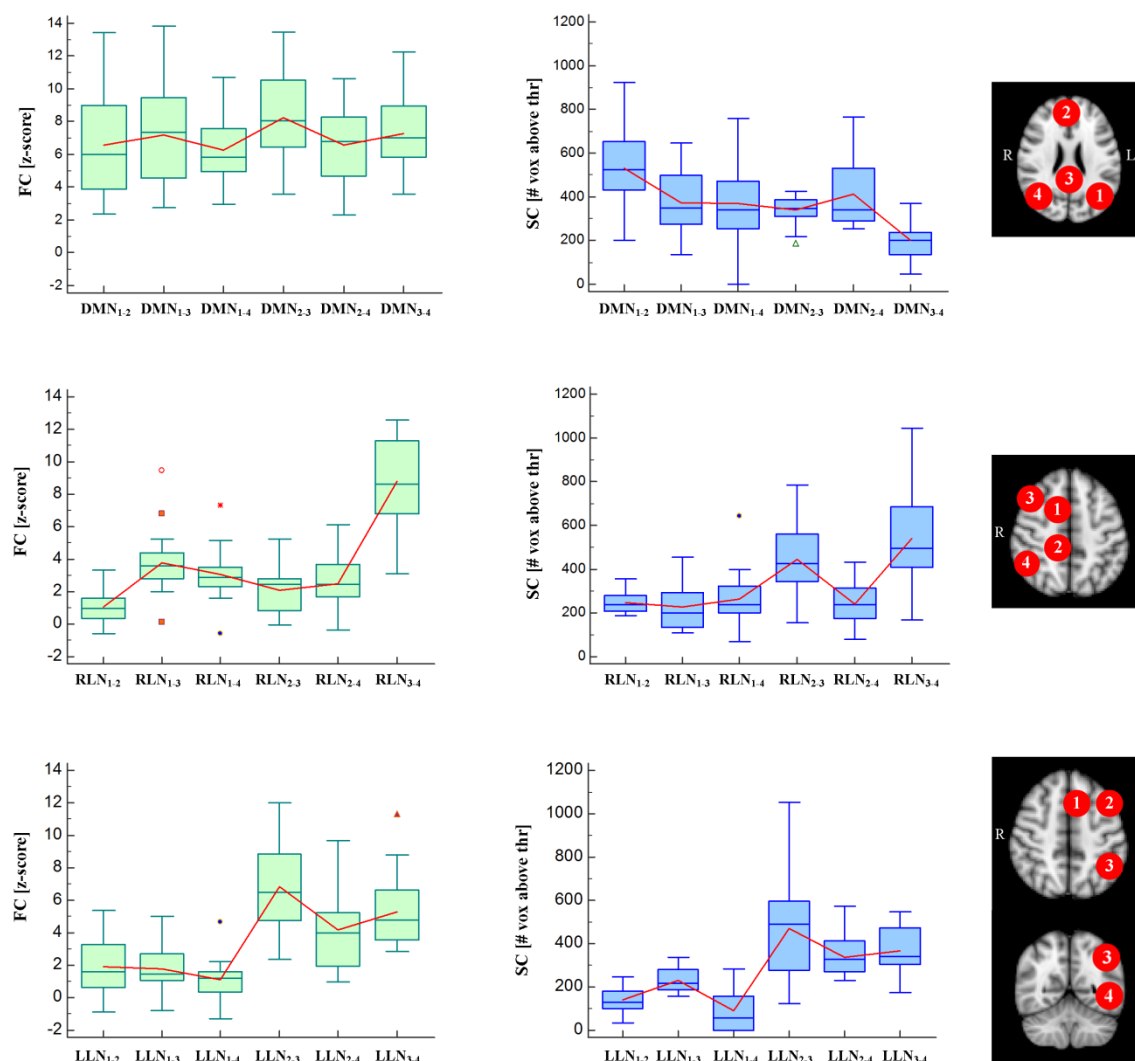
Figure 4.9 DMN, RLN, LLN group FC (on the left, in green) and SC (on the right, in blue) comparison represented in box and whiskers plots. The first line refer to DMN, the second line to RLN and the third line to LLN. On the right, a schematic representation of the RSNs to which the box and whiskers are associated is illustrated: from top to bottom, DMN, RLN, LLN axial views and LLN coronal view are shown.. Red numbered spots represent the identified clusters considered in the plots. Boxes represent median, first quartile (q_1) and third quartile (q_3) values. Whiskers are defined by q_1-1.5*IQR (interquartile range) and q_3+1.5*IQR. Spots beyond the region defined by the whickers represent outliers. The red line superimposed in each box-plot links the mean values evaluated for every pair of ROIs. FC = Functional Connectivity; SC = Structural Connectivity; DMN = Default Mode Network; RLN = Right Lateral Network; LLN = Left Lateral Network.
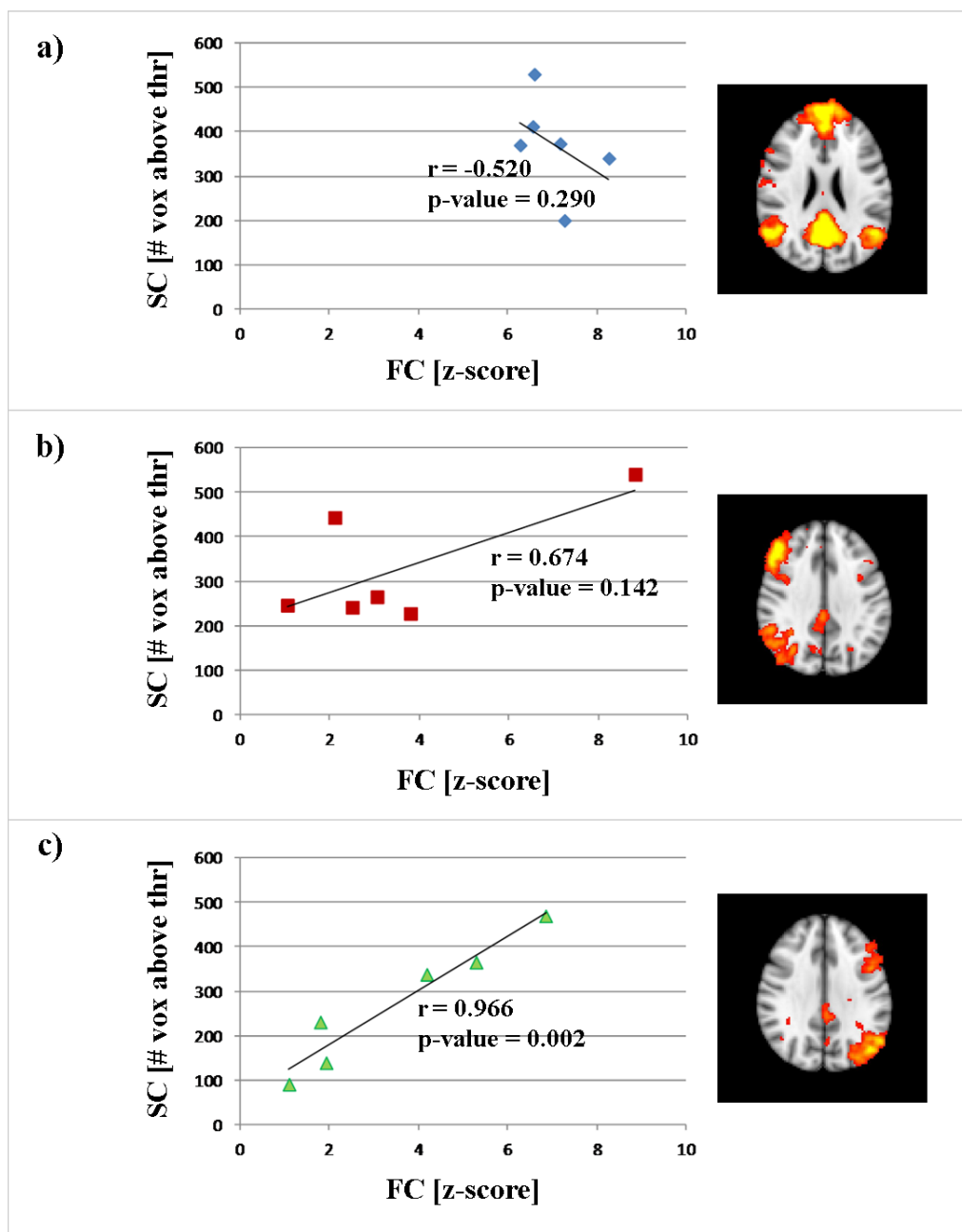
Figure 4.10 Relationship between structural and functional group connectivity within DMN (panel a, in blue), RLN (panel b, in red) and LLN (panel c, in green). FC is expressed as z-score while SC is expressed as the number of voxel above threshold (0.02). Mean FC and SC values calculated across subjects are considered. Pearson correlation coefficient and associated p-values are reported. The respective linear trend line is superimposed. On the right, a representation of the considered RSN is shown. FC = Fuctional Connectivity; SC = Structural Connectivity; DMN = Default Mode Network; RLN = Right Lateral Network; LLN = Left Lateral Network.

4.4.2 Across connections comparison

For each subject, the correlation between FC (expressed as z-score) and SC was analyzed considering all the pairs of clusters. Seventeen out of nineteen subjects showed a positive correlation. In particular, eleven subjects presented a significant correlation (p-value < 0.05) between FC and SC (panel 'a', Fig. 4.11) while the remaining six subjects showed a positive but not significant correlation. However, this six subjects showed an evident positive correlation within two of the three components, namely LLN and RLN (panel 'b', Fig 4.11, on the left) . Only two subjects, instead, did not showed neither a global nor a component-specific correlation between FC and SC (panel 'c', Fig. 4.11).
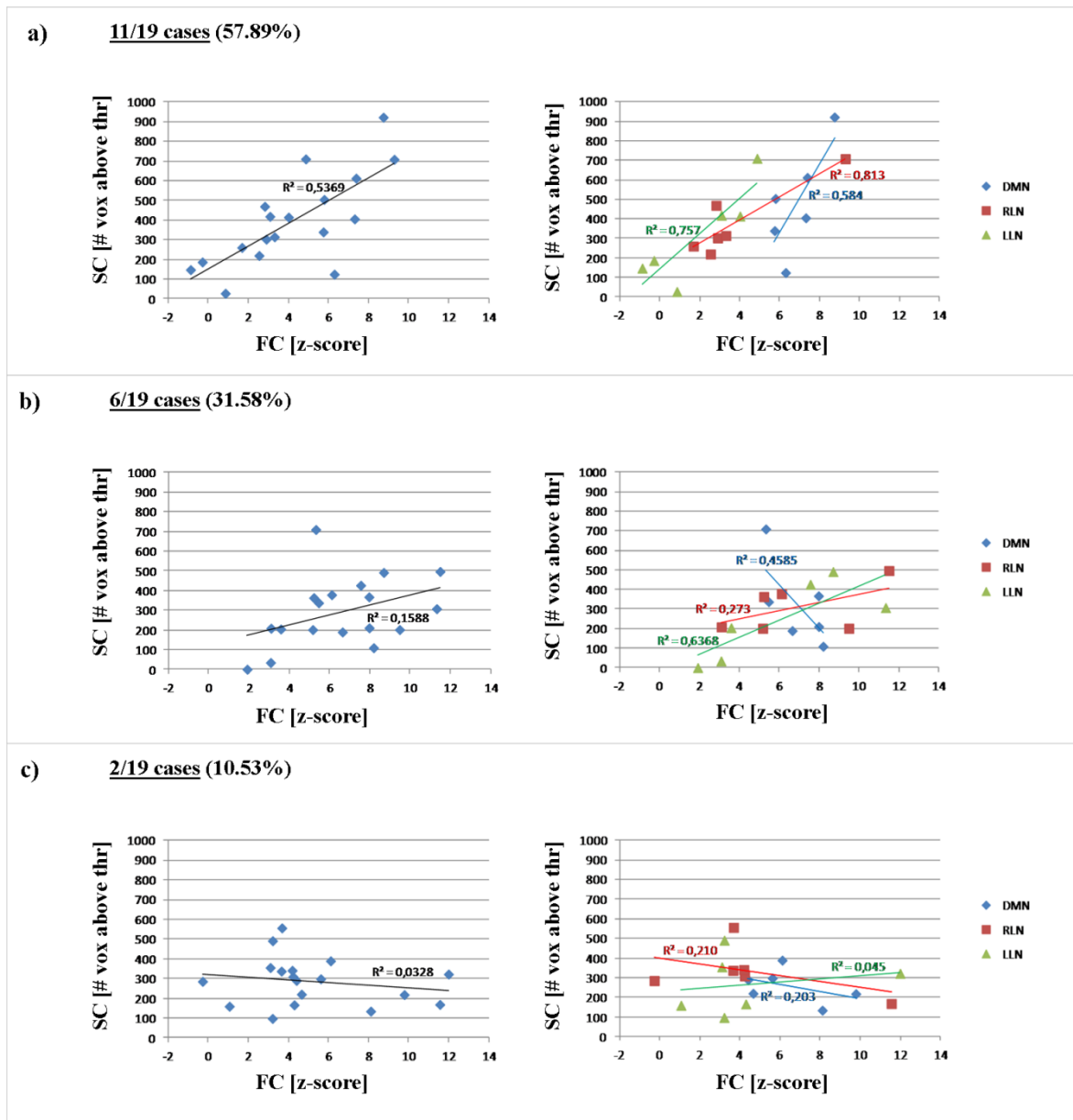
Figure 4.11 SC and FC correlation at single-subject level. Panel a) refers to a representative subject of the group that showed a significant positive correlation. Panel b) refers to a representative subject of the group that showed a positive but not-significant correlation. Panel c) refers to a representative subject of the group that didn't show a positive correlation. The number of subjects belonging to the associated group is reported. In each panel, on the left, scatterplots related to all RSNs of interest are reported with the respective linear trend superimposed; on the right, the same scatterplots are illustrated by highlighting data belonging to DMN (blue points), RLN (red points) and LLN (green points). Their specific linear trend is superimposed (blue line for DMN, red line for RLN, green line for LLN). DMN = Default Mode Network; RLN = Right Lateral Network; LLN = Left Lateral Network.

Chapter 5

Discussion and Conclusion

Main results

Our study aimed at analyzing functional connectivity (FC) and structural connectivity (SC) relationships within specific resting state networks (RSNs).To reach this goal, three RSNs were identified: the default mode network (DMN), the right lateral network (RLN) and the left lateral network (LLN). RLN and LLN enclose the same anatomical regions, respectively in the right and in the left hemisphere, and together they are known as fronto-parietal network.

The DMN was considered since it was the first to be discovered and its clinical relevance is well-established in neurological and psychiatric disorders (e.g. autism, Alzheimer's disease, schizophrenia) (Buckner, 2008). The DMN is involved in human cognition core processes such as the integration of cognitive and emotional processing (Greicius et al., 2003), the monitoring of the world around us (Gusnard at al., 2001) and the mind-wandering (Mason et al., 2007). The fronto-parietal network, instead, is involved in working memory (Rottschy et al., 2012; Smith and Jonides, 1998), episodic retrieval (e.g., Buckner and Wheeler, 2001; Guerin and Miller, 2011; Vilberg and Rugg, 2008), mental

imagery (Daselaar et al., 2010; Kosslyn and Thompson, 2003; Zvyagintsev et al., 2013) attentional control (Mesulam et al., 1990) and language comprehension (Zhu et al.,2014). Specifically, RLN and LLN are involved in different functions, even though they correspond to the same anatomical areas in the two hemisphere, which are known to play different roles in cognitive processes. Hence, we expected to find slight differences between RLN and LLN functional and structural connectivity results.

The selected RSNs were easily and satisfactorily extracted by group independent component analysis (ICA), showing spatial patterns comparable to the literature templates (Smith et al., 2009; van den Heuvel et al., 2010). Moreover, examining FC within each considered RSN, high values of connectivity were observed, especially at group level. In this work, FC within the RSNs was investigated adopting a novel approach in the sub-network definition, namely a clustering procedure based on the anatomical separation of the clusters of which the network consist. This approach differs from the widespread sub-network identification technique through high dimensionality ICA (model order > 30) whose outcome highly depends on the sample size (Dipasquale et al., 2015). Identifying the RSN clusters, taking advantage of their anatomical segregation, allows their easy identification even when a dataset of small dimension is considered. The obtained FC high values are not surprising since ICA, adopted to identify RSNs, extracts spatially independent components from the rsfMRI signal and, thus, it allows to map brain areas that are consistently activated together (Beckmann, 2012). Hence, if some cortical regions are not strongly functionally connected, ICA classifies them into different networks. Nevertheless, obtained FC values were not uniform within each considered RSNs, highlighting the interest in investigating the connectivity between their sub-networks. Regarding this exploration, our results showed that DMN presented remarkable FC index values between all the clusters of which it consists (Fig.4.4, panel *a*). This outcome suggests that DMN is a highly integrative network, in agreement with Greicius and colleagues (2003). Furthermore, in both RLN and LLN, the FC highest values were detected between frontal cortex and parietal cortex (Fig.4.4, panels *b* and *c*). As we expected, RLN and LLN FC patterns were not exactly symmetric. This asymmetry may be justified by the differences between the two hemispheres in the data-driven sub-network identification, probably due to the well-known asymmetry between left and right hemisphere functional roles. Indeed, right fronto-parietal regions underlie visuospatial

orienting attention (Rushworth et al., 2007; Shulman et al., 2010; Rossi et al., 2014), while left fronto-parietal areas are dominant in language comprehension and involuntary orienting, namely attention in relation to limb movements (Rushworth et al., 2007; Rossi et al., 2014; Zhu et al.,2014).

The obtained high FC results made SC study particularly challenging. In fact, evident simultaneous activation of anatomically separated regions doesn't necessarily imply a direct structural connection between them. To test SC within the considered RSNs, the identified sub-networks were adopted as regions of interest (ROIs) in probabilistic tractography. To the best of our knowledge, this approach was adopted only in one previous work (Khalsa et al., 2013). Khalsa and colleagues investigated SC with probabilistic tractography exclusively within DMN, imposing posterior cingulate cortex as seed region and adopting medial prefrontal cortex, right inferior parietal cortex and left inferior parietal cortex as target regions. In our study we adopted a similar approach, even though some methodological modifications were performed. Instead of setting one cluster as seed and all the other ones as targets, we implemented a novel tract processing in order to make the SC symmetric, namely independent from the definition of a cortical area as seed or target region. We decided to process the original tracts as described in paragraph 3.3.3, even if this implied to alter tract intensity values, which represent the probability of the voxels to be part of the bundle that links the seed and the target areas. This methodological choice is in agreement with the literature, which does not use the track intensity in SC evaluation. Furthermore, we investigated connectivity not only within DMN but also within RLN and LLN.

The first remarkable result dealing with SC was that a direct structural connection was found between all the considered sub-networks (Fig. 4.5). In particular, high SC values were found either when a unique robust tract connected the considered ROIs (e.g. DMN_2-DMN_3 connected by cingoli, LLN_2-LLN_3 and RLN_3-RLN_4 connected respectively by left and right SLF) or when an ensemble of tracts was involved (e.g. RLN_2-RLN_3 connection). Low SC values, instead, have to be ascribed to ROI tiny dimensions. It is intuitive inferring that, since fiber tracking imposes the seed and target regions as waypoints, if a ROI is small, the reconstructed virtual tract will be thin, even if the associated bundle is anatomically thick. This would explain why RLN_1 and LLN_1 seemed to be not strongly linked to the other sub-networks belonging to the same RSN, even if remarkable tracts

were involved. Interestingly, high level of SC were strongly consistent across subjects. Indeed, considering the SC consistency matrices created from group probabilistic maps (Fig. 4.7), we could state that the majority of the identified virtual tracts were robust since in probabilistic maps thresholded at 60%,the connections were lost only in 4 out of 18 cluster pairs. These few inconsistent tracts were either thin tracts (such RLN_1 - RLN_4 and LLN_1-LLN_4 connections) or ensemble of tracts (DMN_2-DMN_4 connection), hence, their inconsistency can be justified. The tract linking DMN_1 and DMN_4 was classified as inconsistent too, even if the splenium was involved. This result can be supported by the high inter-subject variability in bundles that connect the two hemisphere, which is especially evident in fascicle terminal parts (Veenith et al., 2013).

The most interesting results were obtained combining FC and SC, adopting, thus, a multimodal approach. This integration was performed by correlating the two connectivity indexes. DMN did not exhibit a correlation between FC and SC, even though it presented high FC and SC values separately, while RLN and, mainly, LLN showed a correspondence between FC and SC trends. This results were obtained both at single and at group level. Particularly, at single level, seventeen out of nineteen subjects globally showed a positive correlation between FC and SC while two subjects only did not presented a correlation between them (Fig. 4.11). The FC and SC correlation was statistically significant ($p<0.05$) for eleven subjects, while it was marginally significant for six subjects. In details, this group of six subjects presented no correlation between the two index value only within DMN. The absence of a positive correlation in this RSN contrasted the positive correlation trend observed in the fronto-parietal network affecting, thus, global FC-SC correlation significance. These results suggest that LLN and RLN are highly function-specific networks and, hence, direct structural links between their clusters reflect the functional communication existing between them. DMN, instead, is a more associative and integrative network. Since it underlies to many different basic functions, DMN sub-networks are highly connected through many different pathways, both direct and indirect. Therefore, FC is not completely explained by structural links detected by tractography, since other fascicles connecting DMN clusters exist (Krienen and Buckner, 2009; O'Reilly et al., 2010; Buckner et al., 2011; Lu et al., 2011). Indeed, graph studies proved that DMN consists of prominent brain hubs that are not only interconnected, but also linked to specific sub-cortical regions, passing through the cortical midline and, thus, defining dense

lower degree networks (van den Heuvel et al., 2011). One possible explanation for the existence of both, direct and indirect communication between these anatomical segregated regions and thus, for connectivity at different levels, might be a possible tendency of the brain to provide a certain level of resilience to its core (van den Heuvel et al., 2011).

In conclusion, our study results proved that SC is a good predictor of FC but, high FC does not necessarily imply high SC. Therefore, in addition to direct connections (that can be identified by tractography), different pathways (e.g. polysynaptic circuits) probably exist and sub-networks communication maybe supported by some other cortical regions which act like mediators.

Applications

The study of brain connectivity as proposed in this work is extremely interesting both in neuroscience field and clinical practice. Several studies have suggested a link between an efficient organization of the brain network and cerebral higher level functions (e.g. cognition, movement coordination, perception, stimulus integration, consciousness, working memory) (Sporns et al., 2004; Edelman et al., 1978). Furthermore, many neurological disorders such as neurodegenerative diseases (e.g. Alzheimer's disease, Parkinson's disease, Huntington's disease, multiple sclerosis), psychiatric (e.g. schizophrenia, depression) and neurodevelopment disorders (e.g. autism) show altered functional and/or structural networks (Guye et al., 2010; Pievani et al., 2014).

Focusing on the neurodegenerative diseases, it is interesting to point out that their symptoms occur long after the actual onset of the brain damages, namely the loss of neurons and synapses. In the phase known as prodromal, although the symptoms are not evident yet, the features of neural networks are altered (Chase, 2014; Unschuld et al., 2012). One of the possible explanations of this phenomenon could be the brain plasticity (Cramer et al., 2011). Indeed, the brain has the extraordinary ability to reorganize its structure in order to compensate as much as possible for damaged areas and interrupted paths. Several studies proved that specific stimuli can lead to a positive plasticity feedback. For instance, Maguire and colleagues (2006) have reported that, in London, taxi drivers show a greater hippocampal volume with respect to bus drivers, due to the fact that the former have to choose among many alternative routes while the latter always drive the same itinerary. Also Diamond (2001), conducting a study on rats, demonstrated that brain

microarchitecture is powerfully shaped by experiences: rats living in enriched environmental conditions showed an increase cortical thickness, leading to a memory improvement and augmented learning ability. In this clinical context, FC and SC analysis may be useful to assess the efficacy of a rehabilitation treatment as neurological rehabilitation perform a brain training and takes advantage of the brain plasticity to prevent the worsening of symptoms, allowing to preserve, at least partially, the patient cognitive abilities (Cramer et al., 2011).

Interestingly, FC and SC combined study may be particularly useful also in pathologies which apparently do not alter the brain architecture but that show evident differences from normality when the connectivity is explored, such as autism spectrum disorders (ASD), attention-deficit/hyperactivity disorder (ADHD) and schizophrenia. Focusing on autism, the literature reports contradictory findings, highlighting that still little is known about this pathology common among children. Even if an altered connectivity is ascertained in children affected by autism, both overconnectivity and underconnectivity was observed (Kitzbichler et al., 2015). Moreover, in autistic children RSN sub-networks that included the frontal cortex were found more likely to be abnormal and to develop abnormally (Kitzbichler et al., 2015). A recent study proved also that in these children relevant parts of the corpus callosum, through which many of the bilaterally activated cortical areas communicate, are smaller than normality (Travers, 2015). The methodological approach used in our study may allow to better investigate this pathology characteristics and origins. Wang and colleagues (2009) have reported a shift of brain topology toward regular networks in children with ADHD, which derives from an increased local efficiency combined with a decreasing tendency in global efficiency. Regarding schizophrenia, recent studies performed with graph analysis showed a deterioration of the hierachical network organizationin in addition to functional and structural "dysconnectivity" (Guye et al., 2010).

In conclusion, considering this broad framework, the importance of adopting a multimodal approach in exploring neurological and psychiatric disorders should appear evident. The high complexity of human brain requires, indeed, an approach as wide as possible in its disorder investigations, since considering only an aspect of the pathology would be restrictive.

Methodological limitations and possible future developments

In this study some technical and methodological limitations were encountered.

As regard with rsfMRI analysis, the principal limitation is that the RSN identification is highly determined by the dataset quality, consistency and dimension. However, ICA outcome dependence on the dataset has the advantage of introducing no *a priori* constraint in the analysis.

Regarding probabilistic tractography, instead, the main limitation is the SC dependency on seed and target definition, as two different tract, and consequently two different SC values, can be obtained between two ROIs. Since we aimed at correlating SC with FC, which it is independent from seed and target definition, we introduced a novel tract processing procedure to obtain a single SC index, as described in paragraph 3.3.3. Another probabilistic tractography weak point is the threshold selection since a gold standard has not been identified yet. By now, when probabilistic tractography is performed, threshold can be defined in two different ways: either attempting different threshold values and then choosing the one considered the best for the current application (Lilja et al., 2014), or choosing it on the basis of previous works. However, both these approaches actually do not guarantee the correct threshold selection. In this work, threshold was set on the basis of previous literature studies (Khalsa et al., 2014). A further limitation is represented by the adopted SC index. Indeed, the number of voxel above threshold is not statistically robust because of two reasons: firstly, SC values depends on the adopted threshold which, as explained above, is defined in an arbitrary way and secondly, this index represents the tract volume expressed in voxels. Therefore, if we consider two bundles of equal thickness, one connecting two distant ROIs and the other one linking two near ROIs, it stands to reason that the former will present higher SC index than the other one, even though, the connection is equally strong. The implemented tract processing lead to another limitation. Indeed, multiplying the two tracts obtained adopting A as seed region and B as target region and *viceversa*, the intensity values in each voxel of the resulted tract do not represent exactly a probability value anymore. Therefore, "symmetric" tract intensities are not comparable between each other. As positive counterpart, this tract processing made the tract more robust to false positive detection.

In future works, some improvements concerning the adopted method and the data quality could be performed. First of all, more robust MR acquisitions could be made using a

3-Tesla scanner, thus providing higher quality data. Moreover, enlarging the sample should be recommended in order to obtain more statistically robust results, especially in RSNs identification. These improvements are very important, especially if we aim at using a healthy subject group as a control sample to compare normality with pathological conditions.

Another useful future development may be the construction of a probabilistic atlas of the tracts involved in DMN, RLN and LLN internal connections ,starting from the constructed group probabilistic maps. When an atlas is constructed, its validation is extremely crucial. Hence, a healthy right-handed subject group, different from the one used to construct the atlas, should be considered. This atlas would be useful especially to explore pathology effects on structural connectivity.

The study could be also deepened by integrating the adopted techniques (ICA for FC analysis and probabilistic tractography for SC analysis) with different methodological approaches. By way of example, FC could be also analyzed with graph theory and SC could be explored using spherical deconvolution, based on a deterministic tractography algorithm. It would be interesting to compare the FC and SC results obtained with different methodological approaches.

Finally, further insight into connectivity could be gained through the integration of MRI data with EEG and MEG studies, in order to draw a broader framework in this wide problem.

Conclusions

The aim of this work was exploring the relationship between FC and SC in three important RSNs: DMN, LLN and RLN within a healthy subject sample. This goal was reached adopting a multimodal approach which combined rsfMRI and probabilistic tractography. Interesting results were obtained, since FC and SC were found to be highly correlated in LLN and RLN while in DMN no correlation was observed between them, proving that high FC does not necessarily implies high SC. These results suggest the existence of many pathways which connect different cortical areas. Furthermore they highlight that LLN and RLN are highly function specific networks while DMN is a more associative one.

The proposed method investigates the brain connectivity issue with a novel approach, which may be promising in typical and atypical condition understanding.

Bibliography

Abou-Elseoud, A., Starck, T., Remes, J., Nikkinen, J., Tervonen, O., & Kiviniemi, V. (2010). The effect of model order selection in group PICA. *Human Brain Mapping, 31*(8), 1207-1216.

Andersson JLR., Jenkinson M., Smith S. (2010). Non-linear registration, aka spatial normalisation. *FMRIB technical report*, TR07JA2.

Basser, P. J., Pajevic, S., Pierpaoli, C., Duda, J., & Aldroubi, A. (2000). In vivo fiber tractography using DT-MRI data. *Magnetic Resonance in Medicine, 44*(4), 625-632.

Beaulieu, C. (2002). The basis of anisotropic water diffusion in the nervous system–a technical review. *NMR in Biomedicine, 15*(7-8), 435-455.

Beckmann, C. F. (2012). Modelling with independent components. *Neuroimage, 62*(2), 891-901.

Beckmann, C. F., Mackay, C. E., Filippini, N., & Smith, S. M. (2009). Group comparison of resting-state FMRI data using multi-subject ICA and dual regression. *Neuroimage, 47*(Suppl 1), S148.

Beckmann, C. F., & Smith, S. M. (2004). Probabilistic independent component analysis for functional magnetic resonance imaging. *Medical Imaging, IEEE Transactions on, 23*(2), 137-152.

Beckmann, C. F., DeLuca, M., Devlin, J. T., & Smith, S. M. (2005). Investigations into resting-state connectivity using independent component analysis. *Philosophical Transactions of the Royal Society of London.Series B, Biological Sciences, 360*(1457), 1001-1013.

Behrens, T., Berg, H. J., Jbabdi, S., Rushworth, M., & Woolrich, M. (2007). Probabilistic diffusion tractography with multiple fibre orientations: What can we gain? *Neuroimage, 34*(1), 144-155.

Behrens, T., Woolrich, M., Jenkinson, M., Johansen-Berg, H., Nunes, R., Clare, S., et al. (2003). Characterization and propagation of uncertainty in diffusion-weighted MR imaging. *Magnetic Resonance in Medicine, 50*(5), 1077-1088.

Bernier, M., Chamberland, M., Houde, J., Descoteaux, M., & Whittingstall, K. (2014). Using fMRI non-local means denoising to uncover activation in sub-cortical structures at 1.5 T for guided HARDI tractography. *Frontiers in Human Neuroscience, 8*

Binnewijzend, M. A., Schoonheim, M. M., Sanz-Arigita, E., Wink, A. M., van der Flier, Wiesje M, Tolboom, N., et al. (2012). Resting-state fMRI changes in alzheimer's disease and mild cognitive impairment. *Neurobiology of Aging, 33*(9), 2018-2028.

Biswal, B., Zerrin Yetkin, F., Haughton, V. M., & Hyde, J. S. (1995). Functional connectivity in the motor cortex of resting human brain using echo-planar mri. *Magnetic Resonance in Medicine, 34*(4), 537-541.

Bluhm, R. L., Miller, J., Lanius, R. A., Osuch, E. A., Boksman, K., Neufeld, R. W., et al. (2007). Spontaneous low-frequency fluctuations in the BOLD signal in schizophrenic patients: Anomalies in the default network. *Schizophrenia Bulletin, 33*(4), 1004-1012.

Boahen, K. A. (2000). Point-to-point connectivity between neuromorphic chips using address events. *Circuits and Systems II: Analog and Digital Signal Processing, IEEE Transactions on, 47*(5), 416-434.

Bonavita, S., Gallo, A., Sacco, R., Corte, M. D., Bisecco, A., Docimo, R., et al. (2011). Distributed changes in default-mode resting-state connectivity in multiple sclerosis. *Multiple Sclerosis (Houndmills, Basingstoke, England), 17*(4), 411-422.

Brookes, M. J., Woolrich, M., Luckhoo, H., Price, D., Hale, J. R., Stephenson, M. C., et al. (2011). Investigating the electrophysiological basis of resting state networks using magnetoencephalography. *Proceedings of the National Academy of Sciences of the United States of America, 108*(40), 16783-16788.

Buckner, R. L., Andrews-Hanna, J. R., & Schacter, D. L. (2008). The brain's default network. *Annals of the New York Academy of Sciences, 1124*(1), 1-38.

Buckner, R. L., Wheeler, M. E., & Sheridan, M. A. (2001). Encoding processes during retrieval tasks. *Journal of Cognitive Neuroscience, 13*(3), 406-415.

Buckner, R. L., Krienen, F. M., Castellanos, A., Diaz, J. C., & Yeo, B. T. (2011). The organization of the human cerebellum estimated by intrinsic functional connectivity. *Journal of Neurophysiology, 106*(5), 2322-2345.

Bush, G., Frazier, J. A., Rauch, S. L., Seidman, L. J., Whalen, P. J., Jenike, M. A., et al. (1999). Anterior cingulate cortex dysfunction in attention-deficit/hyperactivity disorder revealed by fMRI and the counting stroop. *Biological Psychiatry, 45*(12), 1542-1552.

Buxton, R. B., Uludağ, K., Dubowitz, D. J., & Liu, T. T. (2004). Modeling the hemodynamic response to brain activation. *Neuroimage, 23*, S220-S233.

Cabral, J., Kringelbach, M. L., & Deco, G. (2014). Exploring the network dynamics underlying brain activity during rest. *Progress in Neurobiology, 114*, 102-131.

Caffini, M., Bergsland, N., Laganà, M., Tavazzi, E., Tortorella, P., Rovaris, M., et al. (2014). Surface-based reconstruction and diffusion MRI in the assessment of gray and white matter damage in multiple sclerosis. *SPIE Medical Imaging,* pp. 90343V-90343V-6.

Catani, M., & De Schotten, M. T. (2008). A diffusion tensor imaging tractography atlas for virtual in vivo dissections. *Cortex, 44*(8), 1105-1132.

Chase A. (2014). Altered functional connectivity in preclinical dementia. *Nature Reviews Neurology*, 10, 609.

Cherkassky, V. L., Kana, R. K., Keller, T. A., & Just, M. A. (2006). Functional connectivity in a baseline resting-state network in autism. *Neuroreport, 17*(16), 1687-1690.

Comon, P. (1994). Independent component analysis, a new concept? *Signal Processing, 36*(3), 287-314.

Cordes, D., Haughton, V. M., Arfanakis, K., Wendt, G. J., Turski, P. A., Moritz, C. H., et al. (2000). Mapping functionally related regions of brain with functional connectivity MR imaging. *AJNR.American Journal of Neuroradiology, 21*(9), 1636-1644.

Cornew, L., Roberts, T. P., Blaskey, L., & Edgar, J. C. (2012). Resting-state oscillatory activity in autism spectrum disorders. *Journal of Autism and Developmental Disorders, 42*(9), 1884-1894.

Correa, N., Adalı, T., & Calhoun, V. D. (2007). Performance of blind source separation algorithms for fMRI analysis using a group ICA method. *Magnetic Resonance Imaging, 25*(5), 684-694.

Cramer, S. C., Sur, M., Dobkin, B. H., O'Brien, C., Sanger, T. D., Trojanowski, J. Q., et al. (2011). Harnessing neuroplasticity for clinical applications. *Brain : A Journal of Neurology, 134*(Pt 6), 1591-1609.

Damoiseaux, J. S., & Greicius, M. D. (2009). Greater than the sum of its parts: A review of studies combining structural connectivity and resting-state functional connectivity. *Brain Structure and Function, 213*(6), 525-533.

Damoiseaux, J. S., Prater, K. E., Miller, B. L., & Greicius, M. D. (2012). Functional connectivity tracks clinical deterioration in alzheimer's disease. *Neurobiology of Aging, 33*(4), 828. e19-828. e30.

Damoiseaux, J. S., Rombouts, S. A., Barkhof, F., Scheltens, P., Stam, C. J., Smith, S. M., et al. (2006). Consistent resting-state networks across healthy subjects. *Proceedings of the National Academy of Sciences of the United States of America, 103*(37), 13848-13853.

Daselaar, S. M., Porat, Y., Huijbers, W., & Pennartz, C. M. (2010). Modality-specific and modality-independent components of the human imagery system. *Neuroimage, 52*(2), 677-685.

De Luca, M., Beckmann, C., De Stefano, N., Matthews, P., & Smith, S. M. (2006). fMRI resting state networks define distinct modes of long-distance interactions in the human brain. *Neuroimage, 29*(4), 1359-1367.

de Pasquale, F., Della Penna, S., Snyder, A. Z., Lewis, C., Mantini, D., Marzetti, L., et al. (2010). Temporal dynamics of spontaneous MEG activity in brain networks. *Proceedings of the National Academy of Sciences of the United States of America, 107*(13), 6040-6045.

Deco, G., Ponce-Alvarez, A., Mantini, D., Romani, G. L., Hagmann, P., & Corbetta, M. (2013). Resting-state functional connectivity emerges from structurally and dynamically shaped slow linear fluctuations. *The Journal of Neuroscience : The Official Journal of the Society for Neuroscience, 33*(27), 11239-11252.

Desmond, J. E., Gabrieli, J. D., Wagner, A. D., Ginier, B. L., & Glover, G. H. (1997). Lobular patterns of cerebellar activation in verbal working-memory and finger-tapping tasks as revealed by functional MRI. *The Journal of Neuroscience : The Official Journal of the Society for Neuroscience, 17*(24), 9675-9685.

Diamond, M. C. (2001). Response of the brain to enrichment. *Anais Da Academia Brasileira De Ciências, 73*(2), 211-220.

Dickson, J. W., & Gerstein, G. L. (1974). Interactions between neurons in auditory cortex of the cat. *Journal of Neurophysiology, 37*(6), 1239-1261.

Difrancesco, M. W., Holland, S. K., & Szaflarski, J. P. (2008). Simultaneous EEG/functional magnetic resonance imaging at 4 tesla: Correlates of brain activity to spontaneous alpha rhythm during relaxation. *Journal of Clinical Neurophysiology :*

Official Publication of the American Electroencephalographic Society, 25(5), 255-264.

Dipasquale, O., ONLUS, Fondazione Don Carlo Gnocchi, & Nascente, I. S. M. (2015). High dimensional ICA analysis detects within-network functional connectivity damage of default mode and sensory motor networks in 2 alzheimer's disease 3. *Frontiers in Human Neuroscience, 9*, 43.

Edelman, G. M., & Mountcastle, V. B. (1978). *The mindful brain: Cortical organization and the group-selective theory of higher brain function.* Massachusetts Inst of Technology Pr.

Elam, J. S., & Van Essen, D. (2014). Human connectome project. *Encyclopedia of computational neuroscience* (pp. 1-4) Springer.

Faivre, A., Rico, A., Zaaraoui, W., Crespy, L., Reuter, F., Wybrecht, D., et al. (2012). Assessing brain connectivity at rest is clinically relevant in early multiple sclerosis. *Multiple Sclerosis (Houndmills, Basingstoke, England), 18*(9), 1251-1258.

Feige, B., Scheffler, K., Esposito, F., Di Salle, F., Hennig, J., & Seifritz, E. (2005). Cortical and subcortical correlates of electroencephalographic alpha rhythm modulation. *Journal of Neurophysiology, 93*(5), 2864-2872.

Filippini, N., MacIntosh, B. J., Hough, M. G., Goodwin, G. M., Frisoni, G. B., Smith, S. M., et al. (2009). Distinct patterns of brain activity in young carriers of the APOE-epsilon4 allele. *Proceedings of the National Academy of Sciences of the United States of America, 106*(17), 7209-7214.

Fox, M. D., Snyder, A. Z., Vincent, J. L., Corbetta, M., Van Essen, D. C., & Raichle, M. E. (2005). The human brain is intrinsically organized into dynamic, anticorrelated functional networks. *Proceedings of the National Academy of Sciences of the United States of America, 102*(27), 9673-9678.

Garrity, A. G., Pearlson, G. D., McKiernan, K., Lloyd, D., Kiehl, K. A., & Calhoun, V. D. (2007). Aberrant "default mode" functional connectivity in schizophrenia.

Glover, G. H. (1999). Deconvolution of impulse response in event-related BOLD fMRI 1. *Neuroimage, 9*(4), 416-429.

Goncalves, S., De Munck, J., Pouwels, P., Schoonhoven, R., Kuijer, J., Maurits, N., et al. (2006). Correlating the alpha rhythm to BOLD using simultaneous EEG/fMRI: Inter-subject variability. *Neuroimage, 30*(1), 203-213.

Greicius, M. D., Flores, B. H., Menon, V., Glover, G. H., Solvason, H. B., Kenna, H., et al. (2007). Resting-state functional connectivity in major depression: Abnormally increased contributions from subgenual cingulate cortex and thalamus. *Biological Psychiatry, 62*(5), 429-437.

Greicius, M. D., Krasnow, B., Reiss, A. L., & Menon, V. (2003). Functional connectivity in the resting brain: A network analysis of the default mode hypothesis. *Proceedings of the National Academy of Sciences of the United States of America, 100*(1), 253-258.

Greicius, M. D., Srivastava, G., Reiss, A. L., & Menon, V. (2004). Default-mode network activity distinguishes alzheimer's disease from healthy aging: Evidence from functional MRI. *Proceedings of the National Academy of Sciences of the United States of America, 101*(13), 4637-4642.

Greicius, M. D., Supekar, K., Menon, V., & Dougherty, R. F. (2009). Resting-state functional connectivity reflects structural connectivity in the default mode network. *Cerebral Cortex (New York, N.Y.: 1991), 19*(1), 72-78.

Griffanti, L., Salimi-Khorshidi, G., Beckmann, C. F., Auerbach, E. J., Douaud, G., Sexton, C. E., et al. (2014). ICA-based artefact removal and accelerated fMRI acquisition for improved resting state network imaging. *Neuroimage, 95*, 232-247.

Guerin, S. A., & Miller, M. B. (2011). Parietal cortex tracks the amount of information retrieved even when it is not the basis of a memory decision. *Neuroimage, 55*(2), 801-807.

Guye M., Bettus G , Bartolomei F., Cozzone P. (2010). Graph theoretical analysis of structural and functional connectivity MRI in normal and pathological brain networks. *Magnetic Resonance Materials in Physics,* Biology and Medicine, 23, 409–421.

Gusnard, D. A., Akbudak, E., Shulman, G. L., & Raichle, M. E. (2001). Medial prefrontal cortex and self-referential mental activity: Relation to a default mode of brain function. *Proceedings of the National Academy of Sciences of the United States of America, 98*(7), 4259-4264.

Guye, M., Bettus, G., Bartolomei, F., & Cozzone, P. J. (2010). Graph theoretical analysis of structural and functional connectivity MRI in normal and pathological brain networks. *Magnetic Resonance Materials in Physics, Biology and Medicine, 23*(5-6), 409-421.

Hagmann, P., Cammoun, L., Gigandet, X., Meuli, R., Honey, C. J., Wedeen, V. J., et al. (2008). Mapping the structural core of human cerebral cortex. *PLoS Biology, 6*(7), e159.

Hellwig, B. (2000). A quantitative analysis of the local connectivity between pyramidal neurons in layers 2/3 of the rat visual cortex. *Biological Cybernetics, 82*(2), 111-121.

Hipp, J. F., Hawellek, D. J., Corbetta, M., Siegel, M., & Engel, A. K. (2012). Large-scale cortical correlation structure of spontaneous oscillatory activity. *Nature Neuroscience, 15*(6), 884-890.

Honey, C. J., Kotter, R., Breakspear, M., & Sporns, O. (2007). Network structure of cerebral cortex shapes functional connectivity on multiple time scales. *Proceedings of the National Academy of Sciences of the United States of America, 104*(24), 10240-10245.

Honey, C. J., Sporns, O., Cammoun, L., Gigandet, X., Thiran, J. P., Meuli, R., et al. (2009). Predicting human resting-state functional connectivity from structural connectivity. *Proceedings of the National Academy of Sciences of the United States of America, 106*(6), 2035-2040.

Huerta, M. F., Koslow, S. H., & Leshner, A. I. (1993). The human brain project: An international resource. *Trends in Neurosciences, 16*(11), 436-438.

Jenkinson, M., Bannister, P., Brady, M., & Smith, S. (2002). Improved optimization for the robust and accurate linear registration and motion correction of brain images. *Neuroimage, 17*(2), 825-841.

Jenkinson, M., & Smith, S. (2001). A global optimisation method for robust affine registration of brain images. *Medical Image Analysis, 5*(2), 143-156.

Jones, D. K. (2003). Determining and visualizing uncertainty in estimates of fiber orientation from diffusion tensor MRI. *Magnetic Resonance in Medicine, 49*(1), 7-12.

Jones, D. K. (2003). Determining and visualizing uncertainty in estimates of fiber orientation from diffusion tensor MRI. *Magnetic Resonance in Medicine, 49*(1), 7-12.

Jones, D. K. (2008). Studying connections in the living human brain with diffusion MRI. *Cortex, 44*(8), 936-952.

Jones, D. K., & Pierpaoli, C. (2005). Confidence mapping in diffusion tensor magnetic resonance imaging tractography using a bootstrap approach. *Magnetic Resonance in Medicine, 53*(5), 1143-1149.

Jones, D. K., & Pierpaoli, C. (2005). Confidence mapping in diffusion tensor magnetic resonance imaging tractography using a bootstrap approach. *Magnetic Resonance in Medicine, 53*(5), 1143-1149.

Kennedy, D. P., Redcay, E., & Courchesne, E. (2006). Failing to deactivate: Resting functional abnormalities in autism. *Proceedings of the National Academy of Sciences of the United States of America, 103*(21), 8275-8280.

Khalsa, S., Mayhew, S. D., Chechlacz, M., Bagary, M., & Bagshaw, A. P. (2014). The structural and functional connectivity of the posterior cingulate cortex: Comparison between deterministic and probabilistic tractography for the investigation of structure–function relationships. *Neuroimage, 102*, 118-127.

KIM, D., & KIM, M. (2005). Combining functional and diffusion tensor MRI. *Annals of the New York Academy of Sciences, 1064*(1), 1-15.

Kitzbichler, M. G., Khan, S., Ganesan, S., Vangel, M. G., Herbert, M. R., Hämäläinen, M. S., et al. (2014). Altered development and multifaceted band-specific abnormalities of resting state networks in autism. *Biological Psychiatry,*

Koch, M. A., Norris, D. G., & Hund-Georgiadis, M. (2002). An investigation of functional and anatomical connectivity using magnetic resonance imaging. *Neuroimage, 16*(1), 241-250.

Koslow, S. H., & Huerta, M. F. (1997). *Neuroinformatics: An overview of the human brain project* Psychology Press.

Kosslyn, S. M., & Thompson, W. L. (2003). When is early visual cortex activated during visual mental imagery? *Psychological Bulletin, 129*(5), 723.

Krienen, F. M., & Buckner, R. L. (2009). Segregated fronto-cerebellar circuits revealed by intrinsic functional connectivity. *Cerebral Cortex (New York, N.Y.: 1991), 19*(10), 2485-2497.

Kwak, Y., Peltier, S., Bohnen, N., Müller, M., Dayalu, P., & Seidler, R. D. (2010). Altered resting state cortico-striatal connectivity in mild to moderate stage parkinson's disease. *Frontiers in Systems Neuroscience, 4*, 143.

Lai, M., Lombardo, M. V., Chakrabarti, B., Sadek, S. A., Pasco, G., Wheelwright, S. J., et al. (2010). A shift to randomness of brain oscillations in people with autism. *Biological Psychiatry, 68*(12), 1092-1099.

Laufs, H., Krakow, K., Sterzer, P., Eger, E., Beyerle, A., Salek-Haddadi, A., et al. (2003). Electroencephalographic signatures of attentional and cognitive default modes in spontaneous brain activity fluctuations at rest. *Proceedings of the National Academy of Sciences of the United States of America, 100*(19), 11053-11058.

Lazar, M., & Alexander, A. L. (2005). Bootstrap white matter tractography (BOOT-TRAC). *Neuroimage, 24*(2), 524-532.

Lazar, M., & Alexander, A. L. (2005). Bootstrap white matter tractography (BOOT-TRAC). *Neuroimage, 24*(2), 524-532.

Le Bihan, D., Mangin, J., Poupon, C., Clark, C. A., Pappata, S., Molko, N., et al. (2001). Diffusion tensor imaging: Concepts and applications. *Journal of Magnetic Resonance Imaging, 13*(4), 534-546.

Leemans, A., & Jones, D. K. (2009). The B-matrix must be rotated when correcting for subject motion in DTI data. *Magnetic Resonance in Medicine, 61*(6), 1336-1349.

Lilja, Y., Ljungberg, M., Starck, G., Malmgren, K., Rydenhag, B., & Nilsson, D. T. (2014). Visualizing meyer's loop: A comparison of deterministic and probabilistic tractography. *Epilepsy Research, 108*(3), 481-490.

Liu, Z., Fukunaga, M., de Zwart, J. A., & Duyn, J. H. (2010). Large-scale spontaneous fluctuations and correlations in brain electrical activity observed with magnetoencephalography. *Neuroimage, 51*(1), 102-111.

Liu, Y., Liang, M., Zhou, Y., He, Y., Hao, Y., Song, M., et al. (2008). Disrupted small-world networks in schizophrenia. *Brain : A Journal of Neurology, 131*(Pt 4), 945-961.

Logothetis, N. K., & Pfeuffer, J. (2004). On the nature of the BOLD fMRI contrast mechanism. *Magnetic Resonance Imaging, 22*(10), 1517-1531.

Lu, J., Liu, H., Zhang, M., Wang, D., Cao, Y., Ma, Q., et al. (2011). Focal pontine lesions provide evidence that intrinsic functional connectivity reflects polysynaptic anatomical pathways. *The Journal of Neuroscience : The Official Journal of the Society for Neuroscience, 31*(42), 15065-15071.

Maguire, E. A., Woollett, K., & Spiers, H. J. (2006). London taxi drivers and bus drivers: A structural MRI and neuropsychological analysis. *Hippocampus, 16*(12), 1091-1101.

Makris, N., Worth, A., Papadimitriou, G., Stakes, J., Caviness, V., Kennedy, D., et al. (1997). Morphometry of in vivo human white matter association pathways with

diffusion-weighted magnetic resonance imaging. *Annals of Neurology, 42*(6), 951-962.

Marcella Laganà, M., Ceccarelli, A., Giulia Preti, M., Venturelli, C., Pia Sormani, M., Cavarretta, R., et al. (2012). Atlas-Based versus Individual-Based fiber tracking of the corpus callosum in patients with multiple sclerosis: Reliability and clinical correlations. *Journal of Neuroimaging, 22*(4), 355-364.

Mason, M. F., Norton, M. I., Van Horn, J. D., Wegner, D. M., Grafton, S. T., & Macrae, C. N. (2007). Wandering minds: The default network and stimulus-independent thought. *Science (New York, N.Y.), 315*(5810), 393-395.

Matthews, P. M., & Jezzard, P. (2004). Functional magnetic resonance imaging. *Journal of Neurology, Neurosurgery, and Psychiatry, 75*(1), 6-12.

Melhem, E. R., Mori, S., Mukundan, G., Kraut, M. A., Pomper, M. G., & van Zijl, P. C. (2002). Diffusion tensor MR imaging of the brain and white matter tractography. *American Journal of Roentgenology, 178*(1), 3-16.

Mesulam, M. M. (1990). Large-scale neurocognitive networks and distributed processing for attention, language, and memory. *Annals of Neurology, 28*(5), 597-613.

Michalski, A., Gerstein, G., Czarkowska, J., & Tarnecki, R. (1983). Interactions between cat striate cortex neurons. *Experimental Brain Research, 51*(1), 97-107.

Mohammadi, B., Kollewe, K., Samii, A., Krampfl, K., Dengler, R., & Münte, T. F. (2009). Changes of resting state brain networks in amyotrophic lateral sclerosis. *Experimental Neurology, 217*(1), 147-153.

Moosmann, M., Ritter, P., Krastel, I., Brink, A., Thees, S., Blankenburg, F., et al. (2003). Correlates of alpha rhythm in functional magnetic resonance imaging and near infrared spectroscopy. *Neuroimage, 20*(1), 145-158.

Mori S., Tournier JD. (2014). Introduction to Diffusion Tensor Imaging: And Higher Order Models. Academic Press. 35.

Niazy RK., Xie J, Miller K., Beckmann CF., Smith SM. (2011). Spectral characteristics of resting state networks. *Progress in Brain Research*, 193, 259-76.

Nikouline, V. V., Linkenkaer-Hansen, K., Huttunen, J., & Ilmoniemi, R. J. (2001). Interhemispheric phase synchrony and amplitude correlation of spontaneous beta oscillations in human subjects: A magnetoencephalographic study. *Neuroreport, 12*(11), 2487-2491.

O'Reilly, J. X., Beckmann, C. F., Tomassini, V., Ramnani, N., & Johansen-Berg, H. (2010). Distinct and overlapping functional zones in the cerebellum defined by resting state functional connectivity. *Cerebral Cortex (New York, N.Y.: 1991), 20*(4), 953-965.

Petersen, K., Hansen, L. K., Kolenda, T., Rostrup, E., & Strother, S. (2000). On the independent components of functional neuroimages. *Proc. Int. Conf. on Independent Component Analysis and Blind Signal Separation,* pp. 615-620.

Phelps, E. A., Hyder, F., Blamire, A. M., & Shulman, R. G. (1997). FMRI of the prefrontal cortex during overt verbal fluency. *Neuroreport, 8*(2), 561-565.

Pievani, M., Filippini, N., van den Heuvel, Martijn P, Cappa, S. F., & Frisoni, G. B. (2014). Brain connectivity in neurodegenerative diseases [mdash] from phenotype to proteinopathy. *Nature Reviews Neurology, 10*(11), 620-633.

Preti, M. G., Makris, N., Papadimitriou, G., Laganà, M. M., Griffanti, L., Clerici, M., et al. (2014). A novel approach of groupwise fMRI-guided tractography allowing to characterize the clinical evolution of alzheimer's disease. *PloS One, 9*(3), e92026.

Rombouts, S. A., Barkhof, F., Goekoop, R., Stam, C. J., & Scheltens, P. (2005). Altered resting state networks in mild cognitive impairment and mild alzheimer's disease: An fMRI study. *Human Brain Mapping, 26*(4), 231-239.

Rossi, S., Huang, S., Furtak, S. C., Belliveau, J. W., & Ahveninen, J. (2014). Functional connectivity of dorsal and ventral frontoparietal seed regions during auditory orienting. *Brain Research, 1583*, 159-168.

Rottschy, C., Langner, R., Dogan, I., Reetz, K., Laird, A. R., Schulz, J. B., et al. (2012). Modelling neural correlates of working memory: A coordinate-based meta-analysis. *Neuroimage, 60*(1), 830-846.

Rubinov, M., & Sporns, O. (2010). Complex network measures of brain connectivity: Uses and interpretations. *Neuroimage, 52*(3), 1059-1069.

Rushworth, M. F., Krams, M., & Passingham, R. E. (2001). The attentional role of the left parietal cortex: The distinct lateralization and localization of motor attention in the human brain. *Journal of Cognitive Neuroscience, 13*(5), 698-710.

Salvador, R., Suckling, J., Coleman, M. R., Pickard, J. D., Menon, D., & Bullmore, E. (2005). Neurophysiological architecture of functional magnetic resonance images of human brain. *Cerebral Cortex (New York, N.Y.: 1991), 15*(9), 1332-1342.

Sameshima, K., & Baccalá, L. A. (1999). Using partial directed coherence to describe neuronal ensemble interactions. *Journal of Neuroscience Methods, 94*(1), 93-103.

Schoonheim, M. M., Geurts, J. J., Landi, D., Douw, L., van der Meer, Marieke L, Vrenken, H., et al. (2013). Functional connectivity changes in multiple sclerosis patients: A graph analytical study of MEG resting state data. *Human Brain Mapping, 34*(1), 52-61.

Seeley, W. W., Menon, V., Schatzberg, A. F., Keller, J., Glover, G. H., Kenna, H., et al. (2007). Dissociable intrinsic connectivity networks for salience processing and executive control. *The Journal of Neuroscience : The Official Journal of the Society for Neuroscience, 27*(9), 2349-2356.

Setsompop, K., Kimmlingen, R., Eberlein, E., Witzel, T., Cohen-Adad, J., McNab, J. A., et al. (2013). Pushing the limits of in vivo diffusion MRI for the human connectome project. *Neuroimage, 80*, 220-233.

Shepherd, G. M., Mirsky, J. S., Healy, M. D., Singer, M. S., Skoufos, E., Hines, M. S., et al. (1998). The human brain project: Neuroinformatics tools for integrating, searching and modeling multidisciplinary neuroscience data. *Trends in Neurosciences, 21*(11), 460-468.

Shulman, G. L., Pope, D. L., Astafiev, S. V., McAvoy, M. P., Snyder, A. Z., & Corbetta, M. (2010). Right hemisphere dominance during spatial selective attention and target detection occurs outside the dorsal frontoparietal network. *The Journal of Neuroscience : The Official Journal of the Society for Neuroscience, 30*(10), 3640-3651.

Smith, S. M. (2002). Fast robust automated brain extraction. *Human Brain Mapping, 17*(3), 143-155.

Smith, S. M. (2012). The future of FMRI connectivity. *Neuroimage, 62*(2), 1257-1266.

Smith, S. M., Beckmann, C. F., Andersson, J., Auerbach, E. J., Bijsterbosch, J., Douaud, G., et al. (2013). Resting-state fMRI in the human connectome project. *Neuroimage, 80*, 144-168.

Smith, E. E., & Jonides, J. (1998). Neuroimaging analyses of human working memory. *Proceedings of the National Academy of Sciences of the United States of America, 95*(20), 12061-12068.

Smith, S. M., Fox, P. T., Miller, K. L., Glahn, D. C., Fox, P. M., Mackay, C. E., et al. (2009). Correspondence of the brain's functional architecture during activation and rest. *Proceedings of the National Academy of Sciences of the United States of America, 106*(31), 13040-13045.

Sporns, O., Tononi, G., & Edelman, G. (2002). Theoretical neuroanatomy and the connectivity of the cerebral cortex. *Behavioural Brain Research, 135*(1), 69-74.

Sporns, O., Chialvo, D. R., Kaiser, M., & Hilgetag, C. C. (2004). Organization, development and function of complex brain networks. *Trends in Cognitive Sciences, 8*(9), 418-425.

Sporns, O., Chialvo, D. R., Kaiser, M., & Hilgetag, C. C. (2004). Organization, development and function of complex brain networks. *Trends in Cognitive Sciences, 8*(9), 418-425.

Staempfli, P., Reischauer, C., Jaermann, T., Valavanis, A., Kollias, S., & Boesiger, P. (2008). Combining fMRI and DTI: A framework for exploring the limits of fMRI-guided DTI fiber tracking and for verifying DTI-based fiber tractography results. *Neuroimage, 39*(1), 119-126.

Stejskal, E., & Tanner, J. (1965). Spin diffusion measurements: Spin echoes in the presence of a time-dependent field gradient. *The Journal of Chemical Physics, 42*(1), 288-292.

Tanaka, S., & Inui, T. (2002). Cortical involvement for action imitation of hand/arm postures versus finger configurations: An fMRI study. *Neuroreport, 13*(13), 1599-1602.

Tedeschi, G., Trojsi, F., Tessitore, A., Corbo, D., Sagnelli, A., Paccone, A., et al. (2012). Interaction between aging and neurodegeneration in amyotrophic lateral sclerosis. *Neurobiology of Aging, 33*(5), 886-898.

Thomas, J. B., & Wyman, R. J. (1984). Mutations altering synaptic connectivity between identified neurons in drosophila. *The Journal of Neuroscience : The Official Journal of the Society for Neuroscience, 4*(2), 530-538.

Tournier, J., Calamante, F., Gadian, D. G., & Connelly, A. (2004). Direct estimation of the fiber orientation density function from diffusion-weighted MRI data using spherical deconvolution. *Neuroimage, 23*(3), 1176-1185.

Travers, B. G., Tromp, D. P., Adluru, N., Lange, N., Destiche, D., Ennis, C., et al. (2015). Atypical development of white matter microstructure of the corpus callosum in males with autism: A longitudinal investigation. *Molecular Autism, 6*(1), 15.

Tuch, D. S. (2004). Q-ball imaging. *Magnetic Resonance in Medicine, 52*(6), 1358-1372.

Unschuld, P. G., Joel, S. E., Pekar, J. J., Reading, S. A., Oishi, K., McEntee, J., et al. (2012). Depressive symptoms in prodromal huntington's disease correlate with stroop-interference related functional connectivity in the ventromedial prefrontal cortex. *Psychiatry Research: Neuroimaging, 203*(2), 166-174.

van den Heuvel, Martijn P, Mandl, R. C., Kahn, R. S., Pol, H., & Hilleke, E. (2009). Functionally linked resting-state networks reflect the underlying structural connectivity architecture of the human brain. *Human Brain Mapping, 30*(10), 3127-3141.

Van Den Heuvel, Martijn P, & Pol, H. E. H. (2010). Exploring the brain network: A review on resting-state fMRI functional connectivity. *European Neuropsychopharmacology, 20*(8), 519-534.

Van Essen, D. C., Ugurbil, K., Auerbach, E., Barch, D., Behrens, T., Bucholz, R., et al. (2012). The human connectome project: A data acquisition perspective. *Neuroimage, 62*(4), 2222-2231.

Van Someren, E., Van Der Werf, Y., Roelfsema, P., Mansvelder, H., & Lopes da Silva, F. (2011). Spectral characteristics of resting state networks. *Slow Brain Oscillations of Sleep, Resting State and Vigilance, 193*, 259.

Veenith, T. V., Carter, E., Grossac, J., Newcombe, V. F., Outtrim, J. G., Lupson, V., et al. (2013). Inter subject variability and reproducibility of diffusion tensor imaging within and between different imaging sessions. *PloS One, 8*(6), e65941.

Vilberg, K. L., & Rugg, M. D. (2008). Memory retrieval and the parietal cortex: A review of evidence from a dual-process perspective. *Neuropsychologia, 46*(7), 1787-1799.

Wang, L., Zhu, C., He, Y., Zang, Y., Cao, Q., Zhang, H., et al. (2009). Altered small-world brain functional networks in children with attention-deficit/hyperactivity disorder. *Human Brain Mapping, 30*(2), 638-649.

Weng, S., Wiggins, J. L., Peltier, S. J., Carrasco, M., Risi, S., Lord, C., et al. (2010). Alterations of resting state functional connectivity in the default network in adolescents with autism spectrum disorders. *Brain Research, 1313*, 202-214.

Whitfield-Gabrieli, S., Thermenos, H. W., Milanovic, S., Tsuang, M. T., Faraone, S. V., McCarley, R. W., et al. (2009). Hyperactivity and hyperconnectivity of the default network in schizophrenia and in first-degree relatives of persons with schizophrenia. *Proceedings of the National Academy of Sciences of the United States of America, 106*(4), 1279-1284.

Xiong, J., Ma, L., Wang, B., Narayana, S., Duff, E. P., Egan, G. F., et al. (2009). Long-term motor training induced changes in regional cerebral blood flow in both task and resting states. *Neuroimage, 45*(1), 75-82.

Zeki, S. (1993). A vision of the brain.

Zhou, J., Greicius, M. D., Gennatas, E. D., Growdon, M. E., Jang, J. Y., Rabinovici, G. D., et al. (2010). Divergent network connectivity changes in behavioural variant frontotemporal dementia and Alzheimer's disease. *Brain,* , awq075.

Zhu, D., Chang, J., Freeman, S., Tan, Z., Xiao, J., Gao, Y., et al. (2014). Changes of functional connectivity in the left frontoparietal network following aphasic stroke. *Frontiers in Behavioral Neuroscience, 8*

Zvyagintsev, M., Clemens, B., Chechko, N., Mathiak, K. A., Sack, A. T., & Mathiak, K. (2013). Brain networks underlying mental imagery of auditory and visual information. *European Journal of Neuroscience, 37*(9), 1421-1434.